Technical Note: Retrievability of MIPAS cloud parameter

Prepared by: Reinhold Spang (coordinator)

Forschungszentrum Juelich, ICG, Germany [FZJ, ICG]

Version: **FINAL V7.1** Sep 30, 2008

ESA ITT: *AO/1-5255/06/I-OL* **Contract No.** 20601/07/I-OL

Contributors: ICG Forschungszentrum Juelich, Germany

IMK Forschungszentrum Karlsruhe / University Karlsruhe, Germany

OXF University of Oxford, AOPP, UK RAL Rutherford Appleton Laboratories, UK

ULE University of Oxford, UK

ICG: Reinhold Spang, Sabine Griessbach; **IMK**: Michael Höpfner; **OXF**: Anu Dudhai, Jane Hurley; **RAL**: Richard Siddans, Alison Waterfall; **ULE**: John Remedios, Harjinder Sembhi

Total Pages: 123

1. Introduction

Overview of the study

The Michelson Interferometer for Passive Atmospheric Sounding (MIPAS) is a Fourier transform spectrometer for the detection of limb emission spectra in the middle and upper atmosphere. MIPAS cloud spectra contain a variety of crucial information about atmospheric processes such as cloud formation, chemical interaction of clouds and trace gases. The exploration of the scientific extremely valuable spectra – measured by MIPAS for the first time globally with unprecedented spectral resolution – has been just started. First publications on cloud observations of MIPAS already demonstrate the great scientific impact these data can achieve together with new developed scientific algorithms (Ewen et al., 2005, Höpfner et al., 2006a/b, Spang et al., 2005a/b). However, so far no validated and consolidated MIPAS cloud product is available for the scientific community. Therefore the aim of the ESA study *Cloud Information Retrieval from MIPAS Measurements* is the development of a cloud processor with standardized and validated product parameters.

In this context the purpose of the present Technical Note is to review the progress in the study of the feasibility to retrieve following information* from the MIPAS Level 1 data:

- 1. Identification of clouds
- 2. Classification (e.g. PSC types, liquid/solid particle clouds)
- 3. Retrieval of Physical Clouds Parameters (e.g. macro and micro physical)
- 4. Identification and Specification of co-located data to be used for geophysical validation

(*: The list above is in line with the items for the Technical Note addressed in the Statement of Work (SoW))

IR limb measurements from space are extremely sensitive to the detection of optically thin cirrus clouds in the UTLS region (e.g. Spang et al., 2002). Nadir looking instruments are much less sensitive to detect these type of clouds often described with subvisible and ultra-thin cirrus in the literature. The physics behind these clouds, their impact on the radiation budget or the water entrance into the stratosphere are not well understood and quantified. On the other hand recent analyses show that the impact of cloud spectra on retrieval of p/T and trace gas profiles can be

tremendously important and proper cloud screening is necessary to avoid erroneous retrieval results (Remedios and Spang, 2002, Raspollini et al., 2002). So far only a simple and robust cloud flagging for quite optically thick spectra (based on Spang et al. 2004) is implemented in Level 2 processor. Spectra below and at this altitude level will not be retrieved. But this methods need further improvements. Unfortunately no information is transferred by the procedure into the Level 2 product and by this the scientific user has no information if the product might affected by clouds (e.g. optically thin clouds).

Therefore the development of a cloud processor with standardized and validated product parameters would be extremely valuable. The interaction between the proposed output parameter and the operational level 1b and 2 products or other scientific level2 and level3 products would allow for example the analysis of processes in the Upper Troposphere and Lower Stratosphere (UTLS) in respect to cloud formation and water vapour transport, or the formation and chemical imprint of Polar Stratospheric Clouds in the polar regions in much more detail than is currently possible.

Realization

For the design and realisation of the processor it is necessary to define various steps and algorithms in the processor chain (Figure 1). These steps are linked to the scientific analysis, where optimised cloud detection and classification schemes as well as micro/macro physical parameter retrievals have to be developed. A database of cloud spectra and Jacobian/error spectra (CSDB) is the basis for the scientific analysis together with the MIPAS spectra itself. Therefore in the next section the definition, progress and open issues of the CSDB are presented.

Various algorithms for cloud detection and classification were already in use by the partners before the start of the study but had to be improved and consolidated during the first phase of project (feasibility study). These algorithms are still not completely characterised (ongoing build-up of CSDB), but give already a very good estimate of what can be achieved with the scientific algorithms. These results will be presented in sections 3 to 5. Section 6 will summarise the statistics of potential coincidences to various ground, airborne and spaceborne sensor for the validations purpose of different parameters.

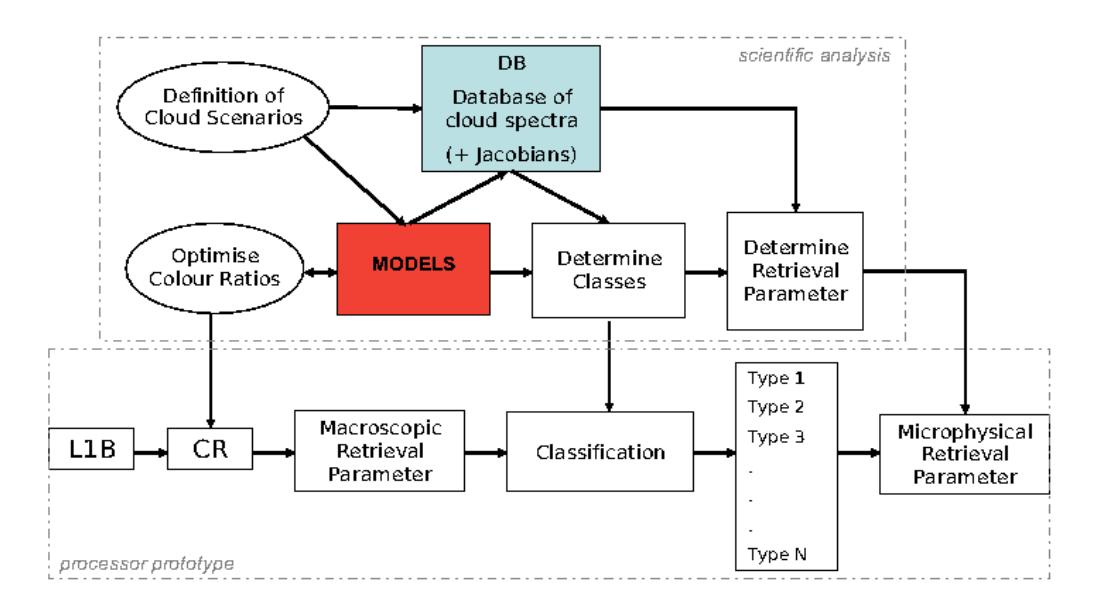


Figure 1: Flowchart of interaction of proposed scientific analysis and the processor prototype

Content

1. Introduction	1
2. Cloud Scenario Database	4
2.1 Selection of spectral intervals	4
2.2 Definition of cloud types, single scattering optical properties and particle s	ize distribution6
2.3 Definition of cloud geometry	
2.4 Definition of observation geometry	12
2.5 Definition of pressure/temperature, trace gas scenarios and the scene belo	
2.6 Definition of Jacobian parameters	13
2.7 Inter-comparison single/multiple scattering model	16
2.8 Technical definition of the database format	25
2.9 Graphical display of the database parameters	26
2.10 Overview/status CSDB	26
2.11 3D scattering model development	28
3. Cloud Identification	
3.1 Operational Cloud Detection and Problems	37
3.2 Improvements for colour ratio based cloud detection	38
3.3 Optimised MircoWindows / Cloud Effective Fraction (CEF) approach	53
3.4 Cloud detection using SVD	
3.5 Comparison of Cloud Detection Methods	64
4. Cloud Classification	67
4.1 Status of PSC classification	67
4.2 Improved PSC classification based on CSDB	69
4.3 Differentiation of Cirrus and Liquid clouds based on CSDB	73
4.4 Index for scattered tropospheric radiation	78
5. Retrieval of Physical Cloud Parameter	81
5.1 Marcophysical Parameter	81
5.2 Microphysical Parameter	88
6. Co-located Validation data	111
6.1 Introduction	111
6.2 In situ and ground based instruments	111
6.3 Satellite Instruments	
6.4 Intercomparison with Aura Instruments	115
7. Summary and Conclusions for Processor Realisation	119
8. References	122

2. Cloud Scenario Database

One major part of the study is the production of a comprehensive database containing modeled MIPAS measurements of clouds and related Jacobian spectra with respect to cloud microphysical parameters and interfering variables. To our knowledge, this is the first time that such extensive simulations have been performed for mid-IR limb-emission sounding of clouds.

The following items had to be defined before the actual production of spectra and Jacobians could be started:

- Selection of spectral intervals
- Definition of cloud types, single scattering optical properties and particle size distribution
- Definition of cloud geometry
- Definition of observation geometry
- Definition of pressure/temperature and trace gas scenarios and the scene below
- Definition of Jacobian parameters
- Selection of computational approach (single vs. multiple scattering)
- Technical definition of the database format

2.1 Selection of spectral intervals

Tests to limit the extend of spectral windows have been performed by calculating broadband Jacobians with respect aerosol extinction at tangent levels with and without gas-contribution. The quotient of these Jacobians (with/without gases) is in first order equal to the gas-transmission spectra at tangent altitude. The rational of these simulations is to exclude regions of the spectrum with strong interference of trace gases and of already opaque intervals.

Calculations have been performed for polar winter (pwi), mid-latitude (mid), and tropical (tro) conditions and for 5, 10, 15, 20, 25, and 30 km tangent altitude. Figure 2 shows the example for 15 km tangent altitude. The red lines here indicate the location of spectral windows for which a limit of 0.9 has been used in the tropical atmosphere scenario at 15 km altitude which is most interesting in case of cirrus clouds.

Additionally to the limb-transmission calculations, the following constraints have been taken into account:

MIPAS Cloud Index ranges:

Spang et al., ASR, 2004

- o CI-A 788.20-796.25 cm⁻¹ (background) 832.3-834.4 cm⁻¹ (free)
- o CI-B 1246.3-1249.1 cm⁻¹ (background) 1232.3-1234.4 cm⁻¹ (free)
- o CI-D 1929.0-1935.0 cm⁻¹ (background) 1973.0-1983.0 cm⁻¹ (free)

Microphysical property retrieval:

Höpfner et al., GRL, 2002; Mendrok et al., GRL, 2007.

- o 825-830 cm⁻¹
- o 947.5-950.5 cm⁻¹
- o 1224-1228 cm⁻¹

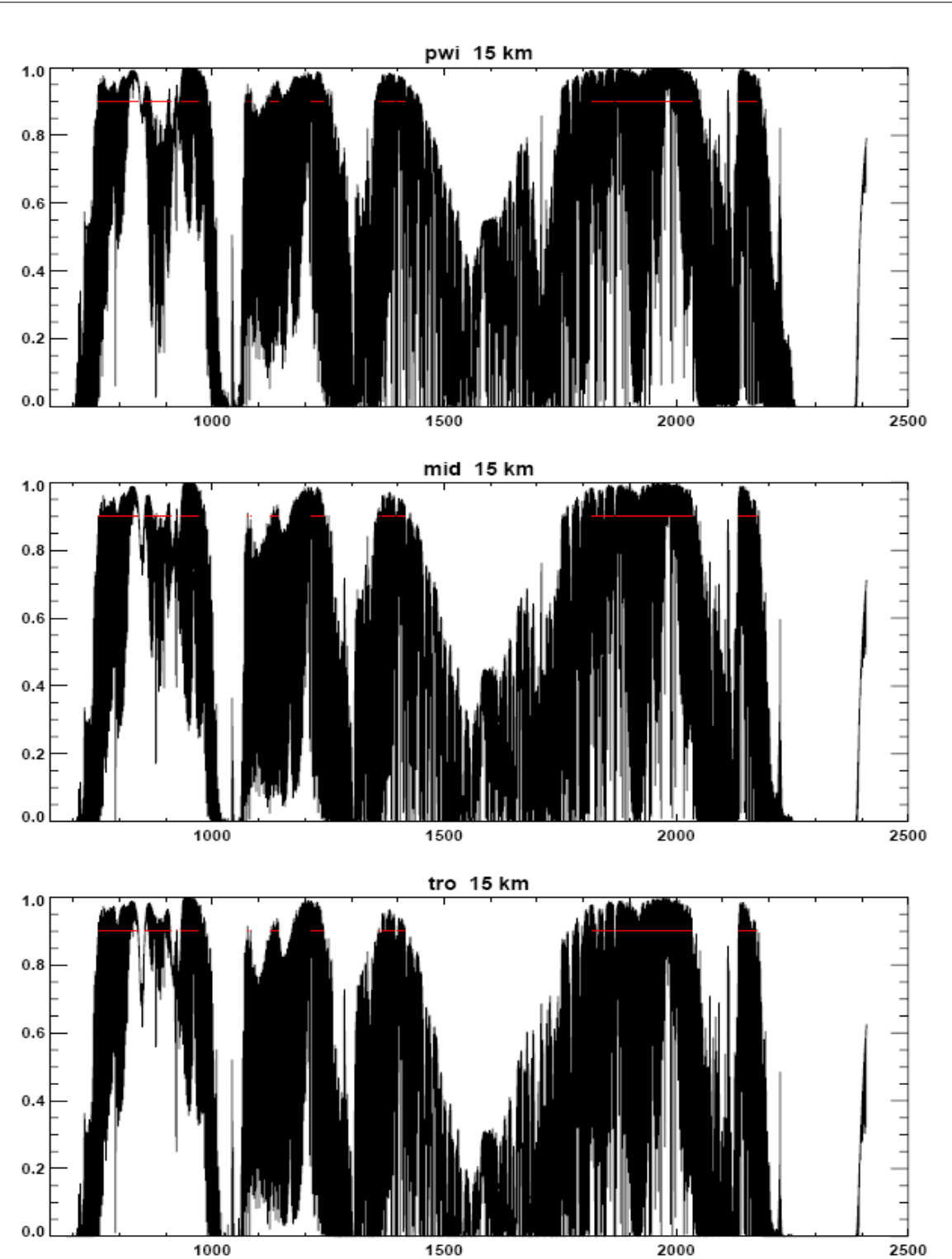


Figure 2: Limb transmission at 15 km tangent altitude for different atmospheres.

• Water vapour distinction:

Spang et al., ASR, 2007

- o 784-785 cm⁻¹ (free)
- o 787-788 cm⁻¹ (background)
- **NAT**:

Spang and Remedios, GRL, 2003, Höpfner et al., ACP, 2006.

o 820 cm⁻¹

Scattering

H2O

lines:

Höpfner et al., GRL, 2002, Höpfner, JQSRT 2004.

- o around 1225 cm⁻¹
- o around 2000 cm⁻¹

In summary, the following ranges have been selected as baseline for the database generation

(137 cm⁻¹ in total):

```
782-841 cm<sup>-1</sup>
940-965 cm<sup>-1</sup>
1224-1235 cm<sup>-1</sup>
1246-1250 cm<sup>-1</sup>
1404-1412 cm<sup>-1</sup>
1929-1935 cm<sup>-1</sup>
1972-1985 cm<sup>-1</sup>
2001-2006 cm<sup>-1</sup>
2140-2146 cm<sup>-1</sup>
```

2.2 Definition of cloud types, single scattering optical properties and particle size distribution

Databases for the following cloud types will be/have been generated:

- Polar stratospheric clouds (PSCs)
- · Cirrus clouds
- Liquid water clouds
- Tropospheric aerosols
- Stratospheric aerosols

2.2.1 Polar stratospheric clouds

Three types of PSCs are believed to be present in the wintertime Arctic/Antarctic stratosphere (e.g. Spang and Remedios, 2003, Höpfner et al., 2006b):

- NAT (Nitric acid trihydrate)
- STS (supercooled ternary H2O/HNO3/H2SO4 solution droplets)
- Ice

For each type of NAT and ice one database has been generated. In order to cover the possible compositions of STS-PSCs three -scenarios have been defined. Table 1 indicates the defined PSC scenarios including the origin of the refractive indices used.

PSC database name	Composition	Refractive index
na	NAT	Biermann 1998,
		Indicated with NAT(coa) in
		Höpfner et al., 2006b
ia	Ice	Toon et al., 1994
sa0248	STS: 2wt% H2SO4, 48wt%	Biermann et al., 2000
	HNO3	
sa2525	STS: 25wt% H2SO4, 25wt%	Biermann et al., 2000
	HNO3	
sa4802	STS: 48wt% H2SO4, 2wt%	Biermann et al., 2000
	HNO3	

Table 1: Definition of composition and refractive indices for PSC database.

On basis of the refractive indices given in Table 1 the single scattering optical properties have been calculated by use of the KOPRA-internal Mie-model using a monomodal log-normal particle size distribution

$$n(r) = \frac{N}{r S \sqrt{2\pi}} \exp\left(\frac{-\ln^2(r/R)}{2W^2}\right)$$

where N is the particle number density [cm⁻³], R the mean radius [µm] and W the width of the distribution.

The corresponding total volume density [µm³ cm⁻³] is

$$V = \frac{4\pi}{3} NR^3 \exp\left(\frac{9}{2} W^2\right) \quad ,$$

and the surface density [µm² cm⁻³] is

$$A = 4 \pi N R^2 \exp(2W^2)$$

As independently varying size distribution parameters for the database the volume density V and the mean radius R have been chosen. As width W of the distribution a value of 0.3 has been defined (Höpfner et al., 2006a, 2006b).

PSC database name	V [μm³ cm-³]	R [μm]
na	0.1, 0.5, 1.0, 5.0, 10.0	0.5, 1.0, 2.0, 3.0, 4.0, 5.0
ia	10, 50, 100	1.0, 2.0, 3.0, 4.0, 5.0, 10.0
sa0248	0.1, 0.5, 1.0, 5.0, 10.0	0.1, 0.5, 1.0
sa2525	0.1, 0.5, 1.0, 5.0, 10.0	0.1, 0.5, 1.0
sa4802	0.1, 0.5, 1.0, 5.0, 10.0	0.1, 0.5, 1.0

Table 2: Definition of size distribution parameters for the PSC database.

2.2.2 Cirrus Clouds

In case of cirrus ice clouds two different procedures have been envisaged for the definition of the single scattering properties to be applied: (a) like in the case of the PSCs database, use of Mie calculations on basis of monomodal particle distributions, or (b) use of precalculated databases of

Technical Note:

bulk single scattering optical properties. We decided to apply precalculated bulk properties (b) since these comprise more realistic particle shapes and particle distributions than pure Mie calculations. Two bulk single scattering databases covering the spectral range of MIPAS have been compared:

- 1.) compiled by B. Baum (http://www.ssec.wisc.edu/~baum/Cirrus/Spectral IR Models.html) on basis of single particle properties by P. Yang (2005).
- 2.) compiled by A. Baran (2001) which has been used within a previous ESA studies (e.g. Kerridge et al., 2004).

Figure 3 shows a comparison of the dependence on effective radius for the single (P. Yang) and both sets of bulk (Baum and Baran) optical properties normalized by the ice-water content (IWC). Prominent differences are the smaller values of the scattering coefficients between the single and the bulk optical properties at the position of the scattering peak. This is due to the effect of size distribution considered in case of bulk optical properties.

Largest differences between the bulk properties of Baum and Baran are around 20%. The dataset by Baran has been chosen as baseline for the cirrus database production due to the following reasons: (1) including smaller effective radii (3.6 μ m vs. 5 μ m for Baum), (2) already used in previous ESA studies, and thus (3) the Legendre decomposition needed by the RAL forward model has been available.

In Table 3 the variation of effective radius and ice water content for the database production is shown.

IWC [g m ⁻³]	V [μm³ cm-³]	Reff [µm]
10^{-6} , 10^{-5} , 10^{-4} , 10^{-3} , 10^{-2} , 10^{-2}	1.09039, 10.903936, 109.039,	4, 6, 8, 12, 16, 20, 25, 30, 40,
¹ , 1	1090.39, 10903.9, 109039.,	50, 70, 90
	1090393.6	

Table 3: Definition of ice water contents (IWC) and effective radii (Reff) for the Cirrus database.

2.2.3 Liquid water clouds

The spectra for liquid water clouds have been calculated on basis of the KOPRA-internal Miemodel using a monomodal log-normal particle size distribution, as has already been described for the PSC-database. For these calculations, a new compilation of complex refractive indices of supercooled liquid water by Zasetsky et al. (2005) has been applied.

As independently varying size distribution parameters for the database the volume density V and the mean radius R have been chosen. As width W of the distribution a value of 0.3 has been fixed.

Database name	V [μm³ cm-³]	R [μm]
liq	$1.09, 1.09 \times 10^{1},, 1.09 \times 10^{6}$	1.0, 2.0, 4.0, 6.0, 8.0, 12.0,
		16.0, 20.0, 25.0

Table 4: Definition of size distribution parameters for the liquid cloud database. V corresponds to liquid water contents of 1.09×10^{-6} ,..., 1.09 g/m^3 .

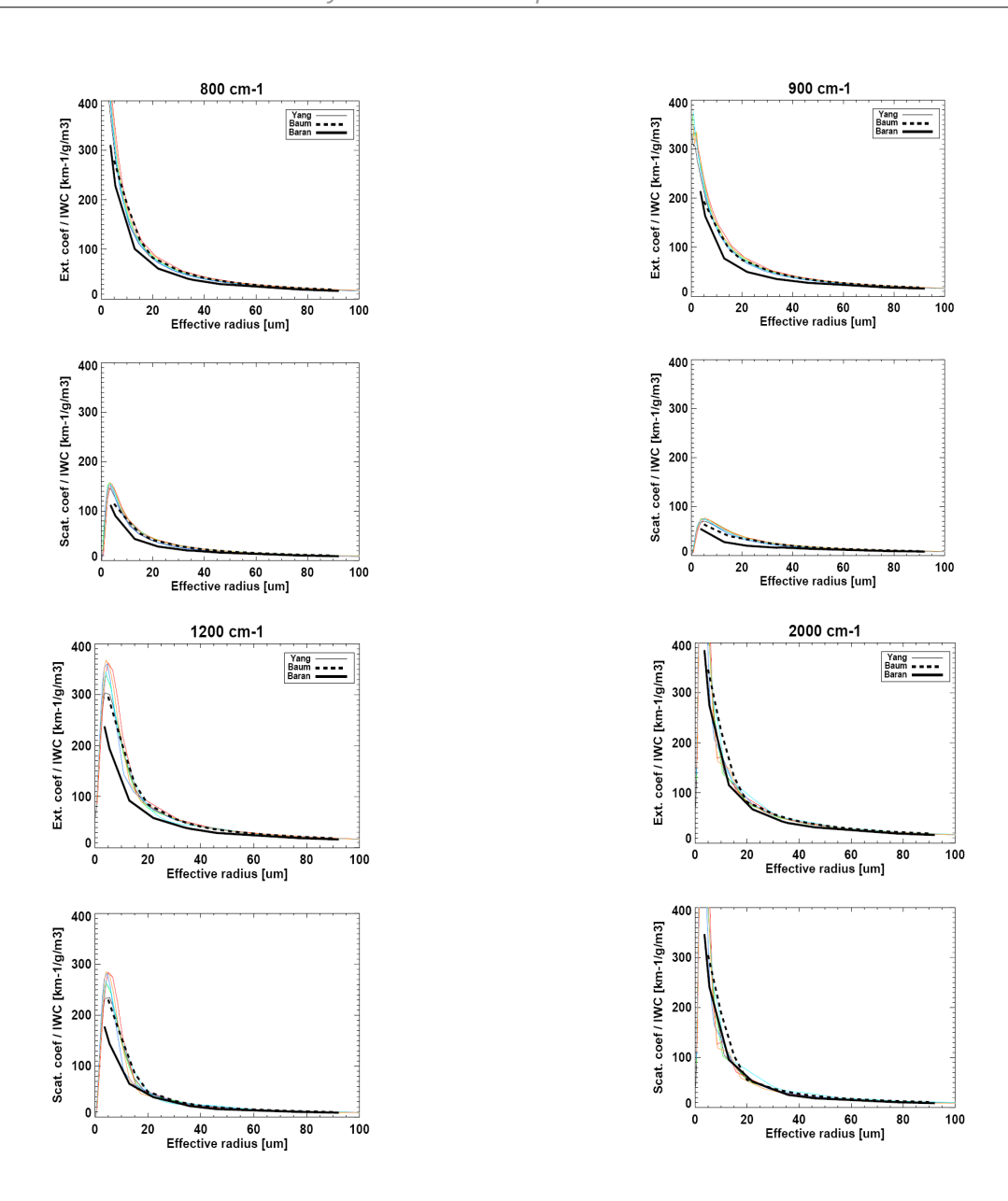


Figure 3: Single (color solid) and bulk (black solid and dashed) particle IWC-normalized optical properties. See text for further description.

2.2.4 Tropospheric Aerosols

The spectra for tropospheric aerosols have been calculated on basis of the KOPRA-internal Miemodel using a bi-modal log-normal particle size distribution:

$$n(r) = \sum_{i=1}^{2} \frac{N_i}{r S_i \sqrt{2\pi}} \exp\left(\frac{-\ln^2(r/R_i)}{2W_{i^2}}\right)$$

where N_i is the particle number density [cm⁻³], R_i the mean radius [μ m] and W_i the width of the i-th mode of the distribution.

Refractive indices of ammonium sulfate by Shettle and Fenn (1979) as supplied with the HITRAN database have been used.

The bi-modal distribution has been chosen such that one mode (mode number 2) has such small radii that it is quasi-totally absorbing which means that the only parameter to be varied is the volume density. The first mode has larger mean radii, such that scattering effects are not negligible. The actual values applied are listed in the following table.

Databa	V_1	\mathbf{R}_1	\mathbf{W}_1	V_2	\mathbb{R}_2	\mathbf{W}_2
se name	[µm³ cm-³]	[µm]		[µm³ cm-³]	[µm]	
tropaer	0.0, 0.5, 1.0, 2.0	0.2, 0.5, 1.0	0.54	0.0, 0.2, 0.4	0.1	0.37

Table 5: Definition of size distribution parameters for the tropospheric aerosol database.

2.2.5 Stratospheric aerosols

The spectra for stratospheric aerosols have been calculated on basis of the KOPRA-internal Miemodel using, like in the tropospheric case, a bi-modal log-normal particle size distribution to account for background and volcanic enhanced conditions.

Refractive indices of sulfuric acid by Tisdale et al. (1998) for a 75wt% H_2SO_4/H_2O at 215 K have been used.

The following table shows the variability of the size parameters chosen for the database.

Databas	V_1	\mathbf{R}_1	W_1	\mathbf{V}_2	\mathbb{R}_2	\mathbf{W}_2
e name	[µm³ cm-³]	[µm]		[µm³ cm-³]	[µm]	
strataer	0.0, 0.5, 1.0, 2.0, 5.0	0.2, 0.5, 1.0	0.45	0.2, 0.5, 1.0	0.1	0.3

Table 6: Definition of size distribution parameters for the stratospheric aerosol database.

2.3 Definition of cloud geometry

For database production the clouds are assumed to be horizontally and vertically homogeneous. Uncertainties caused by this assumption are planned to be quantified by application of the RAL 2d forward modeling in a later stage.

The vertical extend of the cloud is defined by two parameter: the cloud top and the vertical cloud thickness. A minimum altitude additionally confines the cloud bottom. These parameters are listed in Table 7 for the PSC and Cirrus databases.

Cloud top height [km]	Cloud vertical extend [km]	Minimum cloud bottom height [km]
	PSC	
12.5, 13.5, 14.5, 15.5, 16.5, 17.5, 18.5, 19.5, 20.5, 21.5, 22.5, 23.5, 24.5, 25.5, 26.5, 27.5, 28.5	0.5, 1, 2, 4, 8	12
	Tropical cirrus	
4.5, 5.5, 6.5, 7.5, 8.5, 9.5, 10.5, 11.5, 12.5, 13.5, 14.5, 15.5, 16.5, 17.5, 18.5, 19.5, 20.5	0.5, 1, 2, 3, 4	6
	Midlatitude cirrus	
6.5, 7.5, 8.5, 9.5, 10.5, 11.5, 12.5	0.5, 1, 2, 3, 4	6
	Arctic cirrus	
4.5, 6.5, 7.5, 8.5, 9.5, 10.5	0.5, 1, 2, 3, 4	4
	Tropical liquid	
4.5, 5.5, 6.5, 7.5, 8.5, 9.5, 10.5, 11.5, 12.5, 13.5, 14.5	0.5, 1, 2, 3, 4	4
	Midlatitude liquid	
4.5, 5.5, 6.5, 7.5, 8.5, 9.5, 10.5, 11.5, 12.5	0.5, 1, 2, 3, 4	4
	Arctic liquid	
4.5, 6.5, 7.5, 8.5, 9.5, 10.5	0.5, 1, 2, 3, 4	4
	Tropical tropaer	
4.5, 5.5, 6.5, 7.5, 8.5, 9.5, 10.5, 11.5, 12.5, 13.5, 14.5	0.5, 1, 2, 3, 4	4
	Midlatitude tropaer	
4.5, 5.5, 6.5, 7.5, 8.5, 9.5, 10.5, 11.5, 12.5	0.5, 1, 2, 3, 4	4
	Arctic tropaer	
4.5, 6.5, 7.5, 8.5, 9.5, 10.5	0.5, 1, 2, 3, 4	4
	Tropical strataer	
18.5, 19.5, 20.5, 21.5, 22.5, 23.5,	0.5, 1, 2, 3, 4	4
24.5, 25.5, 26.5, 27.5, 28.5		
	Midlatitude strataer	
12.5, 13.5, 14.5, 15.5, 16.5, 17.5,	0.5, 1, 2, 3, 4	4
18.5, 19.5, 20.5, 21.5, 22.5, 23.5, 24.5, 25.5, 26.5, 27.5, 28.5		
2, 20.0, 20.0, 27.0, 20.0	Arctic strataer	
12.5, 13.5, 14.5, 15.5, 16.5, 17.5,	0.5, 1, 2, 3, 4	4
18.5, 19.5, 20.5, 21.5, 22.5, 23.5,		
24.5, 25.5, 26.5, 27.5, 28.5		

Table 7: Definition of cloud top and vertical extend.

2.4 Definition of observation geometry

Limb emission spectra for infinitesimal field-of-views have been generated for the tangent altitudes given in Table 8.

Tangent altitudes [km]
PSC
12, 13, 14, 15, 16, 17, 18, 19, 20, 21, 22, 23, 24, 25, 26, 27, 28
Tropical cirrus
4, 5, 6, 7, 8, 9, 10, 11, 12, 13, 14, 15, 16, 17, 18, 19, 20
Midlatitude cirrus
4, 5, 6, 7, 8, 9, 10, 11, 12
Arctic cirrus
4, 5, 6, 7, 8, 9, 10
Tropical liquid
4, 5, 6, 7, 8, 9, 10, 11, 12, 13, 14
Midlatitude liquid
4, 5, 6, 7, 8, 9, 10, 11, 12
Arctic liquid
4, 5, 6, 7, 8, 9, 10
Tropical tropaer
4, 5, 6, 7, 8, 9, 10, 11, 12, 13, 14
Midlatitude tropaer
4, 5, 6, 7, 8, 9, 10, 11, 12
Arctic tropaer
4, 5, 6, 7, 8, 9, 10
Tropical strataer
12, 13, 14, 15, 16, 17, 18, 19, 20, 21, 22, 23, 24, 25, 26, 27, 28
Midlatitude strataer
12, 13, 14, 15, 16, 17, 18, 19, 20, 21, 22, 23, 24, 25, 26, 27, 28
Arctic strataer
12, 13, 14, 15, 16, 17, 18, 19, 20, 21, 22, 23, 24, 25, 26, 27, 28

Table 8: Definition of observation tangent altitudes.

2.5 Definition of pressure/temperature, trace gas scenarios and the scene below

For pressure/temperature and trace gas volume mixing ratio profiles the standard profiles by Remedios et al. (2007) have been used (see Table 9).

The scene below the tangent point can be an important factor modulating the measured radiances of a limb-sounding instrument. To simulate this effect, two sets of calculation have been performed: one with clear-sky and one with optically thick clouds below the lowest tangent point. The surface temperature has been set to the temperature of the lowest atmospheric level and in case of clouds, the effectively emitting surface is the altitude of the cloud top with the temperature there.

	G 4				_, ,
Atmosphere	Surface T I K I	Low	cloud	height	Cloud top T [K]
					o

Tec	Technical Note: Retrievability of MIPAS cloud parameter		d parameter	Contract No.:20601/07/I-OL
		•	1	
			[km]	
		PS	С	
	mipas_pwin_d2.atm	256.7	6	226.7
		Tropica	cirrus	
	mipas_eqn_d2.atm	300.9	4	277.9
	-	Midlatitu	de cirrus	
	mipas_midl_day_d2.atm	285.1	4	263.2
Arctic cirrus				
	mipas_psum_d2.atm	254.9	4	249.6

Table 9: Definition atmospheric composition and p/T profile and the scene below .

P/T and vmr profiles
PSC
mipas_pwin_d2.atm
Tropical cirrus/liquid/tropaer/strataer
mipas_eqn_d2.atm
Midlatitude cirrus/liquid/tropaer/strataer
mipas_midl_day_d2.atm
Arctic cirrus/liquid/tropaer/strataer
mipas_psum_d2.atm

Table 10: Definition atmospheric composition and p/T profile.

2.6 Definition of Jacobian parameters

The spectral database comprises not only simulated cloud measurements but also the derivatives of the spectra (Jacobians) with respect to cloud parameters envisaged to be retrieved and, for some cases also possible interfering quantities.

2.6.1 Jacobians for PSC database

In case of the PSC database where a lognormal size distribution has been used as baseline for the calculation of single scattering properties, Jacobians with respect to the distribution parameters N, R, and W have been determined, i.e.:

$$\left(\frac{ds}{dN}\right)_{R,W=const}, \left(\frac{ds}{dR}\right)_{N,W=const}, \left(\frac{ds}{dW}\right)_{N,R=const}$$

Here *s* denotes the spectral radiance.

Since volume density is often a more appropriate (smaller linear dependence) retrieval quantity, the related Jacobians can be determined from the calculated ones by transformation:

$$\left(\frac{ds}{dV}\right)_{R,W=const} = \left(\frac{ds}{dN}\right)_{R,W=const} \frac{N}{V}$$

$$\left(\frac{ds}{dR}\right)_{V,W=const} = \frac{-3N}{R} \left(\frac{ds}{dN}\right)_{R,W=const} + \left(\frac{ds}{dR}\right)_{N,W=const}$$

Jacobian	Database name
----------	---------------

Technical Note:	Retrievability of MIPAS cloud parameter		Contract No.:20601/07/I-O		
$\left(\frac{ds}{dN}\right)_{R,W=const}$		dn_			
$\left(\frac{ds}{dR}\right)_{N,W=const}$		dr_			
$\left(\frac{ds}{dW}\right)_{N,R=const}$		dw_			

Table 11: Definition of Jacobians for PSC database.

2.6.2 Jacobians for Cirrus database

In case of the Cirrus database the clouds are naturally defined by the parameters of the bulk optical properties, i.e. the effective radius Reff and the ice water content IWC. Thus, the following Jacobians are calculated:

$$\left(\frac{ds}{dIWC}\right)_{Reff=const}$$
, $\left(\frac{ds}{dReff}\right)_{IWC=const}$

In addition, the dependence on water vapour, as the main interfering species in the troposphere and on temperature has been determined:

$$\left(\frac{ds}{dH_{2}O\left(tang\right)}\right), \left(\frac{ds}{dH_{2}O\left(cloud\right)}\right), \left(\frac{ds}{dT\left(tang\right)}\right), \left(\frac{ds}{dT\left(cloud\right)}\right)$$

Here, $H_2O(tang)$ and T(tang) denote the water vapor vmr and the temperature value at the tangent level and $H_2O(cloud)$ and T(cloud) the water vapor vmr and the temperature value at the cloud position.

Jacobian	Database name
$\left(\frac{ds}{dIWC}\right)_{Reff=const}$	diwc
$\left(\frac{ds}{dReff}\right)_{IWC=const}$	dreff_
$\left(\frac{ds}{dH_2O(cloud)}\right)$	dvmr1
$\left(\frac{ds}{dH_2O(tang)}\right)$	dvmr2
$\left(\frac{ds}{dT\left(cloud\right)}\right)$	dT1
$\left(\frac{ds}{dT(tang)}\right)$	dT2

Table 12: Definition of Jacobians for Cirrus databases.

2.6.3 Jacobians for liquid cloud database

In case of the liquid cloud database where a lognormal size distribution has been used as baseline for the calculation of single scattering properties, Jacobians with respect to the distribution parameters N, R, and W have been determined, like for the PSC database (see above).

In addition, the dependence on water vapour, as the main interfering species in the troposphere and on temperature has been determined, as in case of the cirrus database (see above).

Jacobian	Database name
$\left(\frac{ds}{dN}\right)_{R,W=const}$	dn_
$\left(\frac{ds}{dR}\right)_{N,W=const}$	dr_
$\left(\frac{ds}{dW}\right)_{N,R=const}$	dw_
$\left(\frac{ds}{dH_2O\left(cloud\right)}\right)$	dvmr1
$\left(\frac{ds}{dH_2O(tang)}\right)$	dvmr2
$\left(\frac{ds}{dT\left(cloud\right)}\right)$	dT1
$\left(\frac{ds}{dT(tang)}\right)$	dT2

Table 13: Definition of Jacobians for liquid database.

2.6.4 Jacobians for the (tropospheric and stratospheric) aerosol databases

In case of the aerosol databases where a bimodal-lognormal size distribution has been used as baseline for the calculation of single scattering properties, Jacobians with respect to the distribution parameters N_1 , R_1 , W_1 , N_2 , R_2 , and W_2 have been determined (Table 14).

In addition, the dependence on water vapour, as the main interfering species in the troposphere and on temperature has been determined, as in case of the cirrus database (see above).

Jacobian	Database name
$\left(\frac{ds}{dN_1}\right)_{R_1, W_1, N_2, R_2, W_2 = const}$	dn_
$\left(\frac{ds}{dR_1}\right)_{N_1, W_1, N_2, R_2, W_2 = const}$	dr_
$\left(\frac{ds}{dW_1}\right)_{N_1, R_1, N_2, R_2, W_2 = const}$	dw_
$\left(\frac{ds}{dN_2}\right)_{N_1, R_1, W_1, R_2, W_2 = const}$	dn2_
$\left(\frac{ds}{dR_2}\right)_{N_1,R_1,W_1,N_2,W_2=const}$	dr2_
$\left(\frac{ds}{dW_2}\right)_{N_1,R_1,W_1,N_2,R_2=const}$	dw2_
$\left(\frac{ds}{dH_2O(cloud)}\right)$	dvmr1
$\left(\frac{ds}{dH_2O(tang)}\right)$	dvmr2
$\left(\frac{ds}{dT\left(cloud\right)}\right)$	dT1
$\left(\frac{ds}{dT(tang)}\right)$	dT2

Table 14: Definition of Jacobians for aerosol databases.

2.7 Inter-comparison single/multiple scattering model

The IMK KOPRA model is to be used to calculate the main body of the CSDB. The model is sufficiently fast to enable a comprehensive range of conditions to be simulated, but assumes single scattering in a horizontally symmetric (1-d) atmosphere. The RAL FM2D model is to be used to supplement the database by computing radiances from realistically structured cloud fields, including the effects of multiple scattering. In order to ensure consistency between simulations with the two models, an intercomparison exercise has been carried out.

For this purpose, two microwindows were selected: 946-951 and 2000-2007 cm⁻¹ (window regions with some absorption features of H_2O and CO_2 and O_3). Calculations were performed for an ice cloud with a profile of ice water content increasing from 0 g/m3 to x g/m3 between 9.5 and 10 km then constant until 12 km and decreasing to 0 g/m3 at 12.5 km. Values of x were chosen to correspond to cloud which is thin in nadir and limb, progressing to thin in nadir/thick in limb and finally optically thick cloud in nadir and limb (values of x = 3.7e-6,3.7e-5,3.7e-4,3.7e-3,3.7e-2 g/m3 were used). Single scattering is expected to be accurate at the two extremes of this range. Multiple scattering is likely to be most important for the intermediate cases. The following effective radii were assumed in each case: $3.6, 5.5, 13, 22.1, 33.6, 35.8, 46.1, 77.4, 92.2\mu m$. Furthermore, the Earth surface Temperature was assumed to be 285.14 K (the temperature of the lowest atmospheric layer), with emissivity equal to 1. Trace-gas absorption coefficients for a mid-

latitude atmosphere were computed by IMK and used in both models. The Baran ice cloud spectral optical properties, illustrated in Figure 4, were used (parameterised in terms of the given IWC and effective radius).

Results are shown in figures Figure 5-Figure 8 for the 5 different IWC (each row), the 7 effective radii (each line in each panel), two tangent altitudes (8 and 11km, on separate figures) and the two microwindows. In assessing the differences one should bear in mind that in real applications uncertainty due to no knowing the scene below the tangent point (e.g. lower cloud, surface properties) can cause errors in simulated radiance which can be larger than 50%. Other effects e.g. related to cloud horizontal and vertical structure also introduce uncertainty. At 950 cm-1, which is near the ice absorption band the differences in the KOPRA and FM2D radiances are always below 5% and for nearly all cases below 2%. In this case, single scattering seems to be sufficient.

Differences are larger at 2000 cm⁻¹ where the single scattering albedo is larger. Radiance differences reach up to 50% for small particles, where the single scattering albedo becomes large, in combination with intermediate IWCs, where the cloud is still thin in nadir but thick in limb. Most differences are however still below 20%.

The calculations described above neglect solar scattering which will effect MIPAS short-wave observations during day-time. Both Kopra and FM2D are capable of simulating this effect. As a further test, FM2D was also used to compute radiances for the above cloud cases, including solar scattering in the 2000 cm⁻¹microwindow (the effect is negligible at 950 cm⁻¹). Figure 9-Figure 10 illustrate the results assuming a solar zenith angle of 45 degrees and relative azimuth of 60 degrees (therefore a scattering angle of ~69 degrees at the tangent point). Solar scattering is seen to modify radiances by up to 60% for this view geometry and it is noted that the effect is strongly dependent on scattering angle and could be much larger for more forward scattering conditions (since the cloud phase function is generally strongly forward peaked).

We conclude from these simulations that (a) differences between FM2D and KOPRA are as expected, with multiple scattering being important for intermediate cloud optical thickness, but good agreement for fully optically thin and fully optically thick clouds; (b) radiance differences introduced by multiple scattering are generally within the range of other uncertainties affecting cloud radiative transfer; (c) the single scattering Kopra model should be used to compute the full range of (1-d) cloud conditions in the CSDB and these radiances / weighting functions will be used to develop the cloud retrieval schemes; (d) consideration should be given to the effect of solar scattering (for day-time retrievals) in the short-wave; (e) multiple scattering calculations with FM2D for a limited number of 1-d and 3-d cloud scenes will be used (as planned) to verify the performance of the developed schemes with more realistic simulated observations.

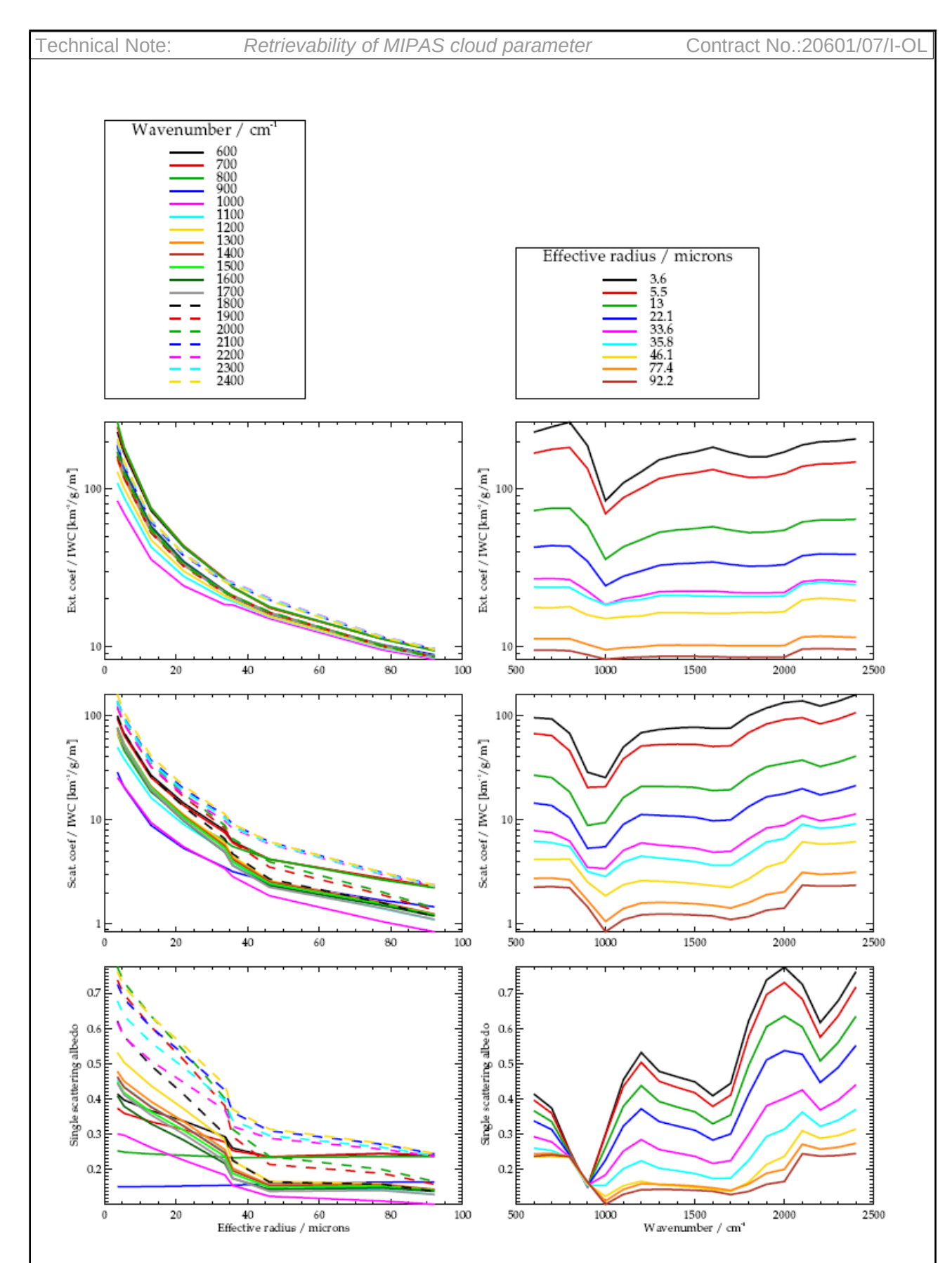


Figure 4: Ice cloud optical properties from the Baran aggregate database. Columns show the same data, but with x-axis effective radius on the left and wavenumber on the right. The top pair of panels show extinction coefficient per unit ice water content (IWC). The middle pair show scattering coefficient per unit IWC and the bottom panel shows the single scattering albedo.

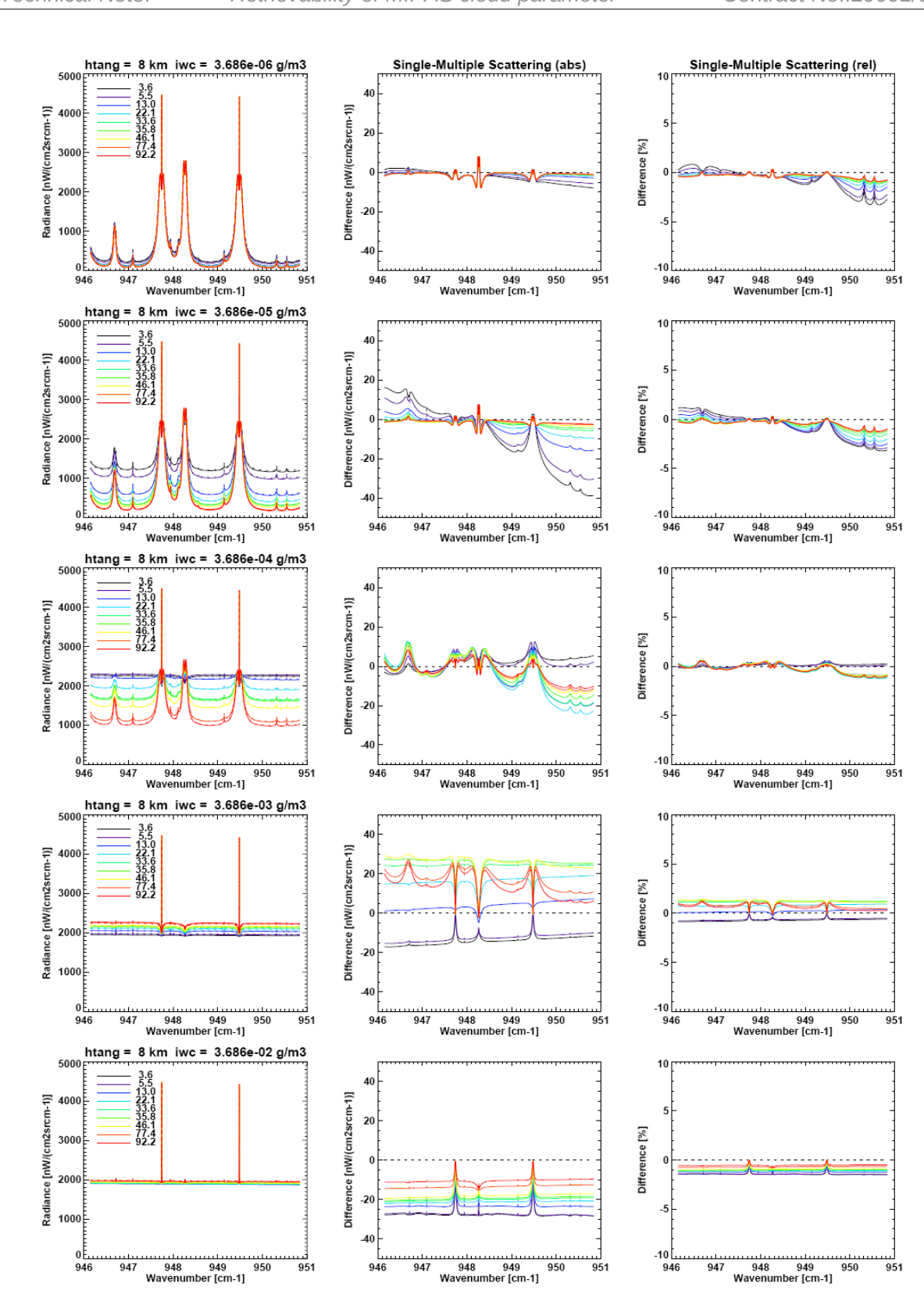


Figure 5: Comparison of single and multiple scattering models (KOPRA/FM2D) for various cloud scenarios. The 1st column show simulated spectra at 8km for a cloud centred at 11km. Solid lines show results for single scattering, whilst dashed lines show the multiple scattering results. Coloured lines are for different IWRE (as given in key), whilst each row is for different IWC. The 2nd and 3rd columns show absolute and relative differences respectively.

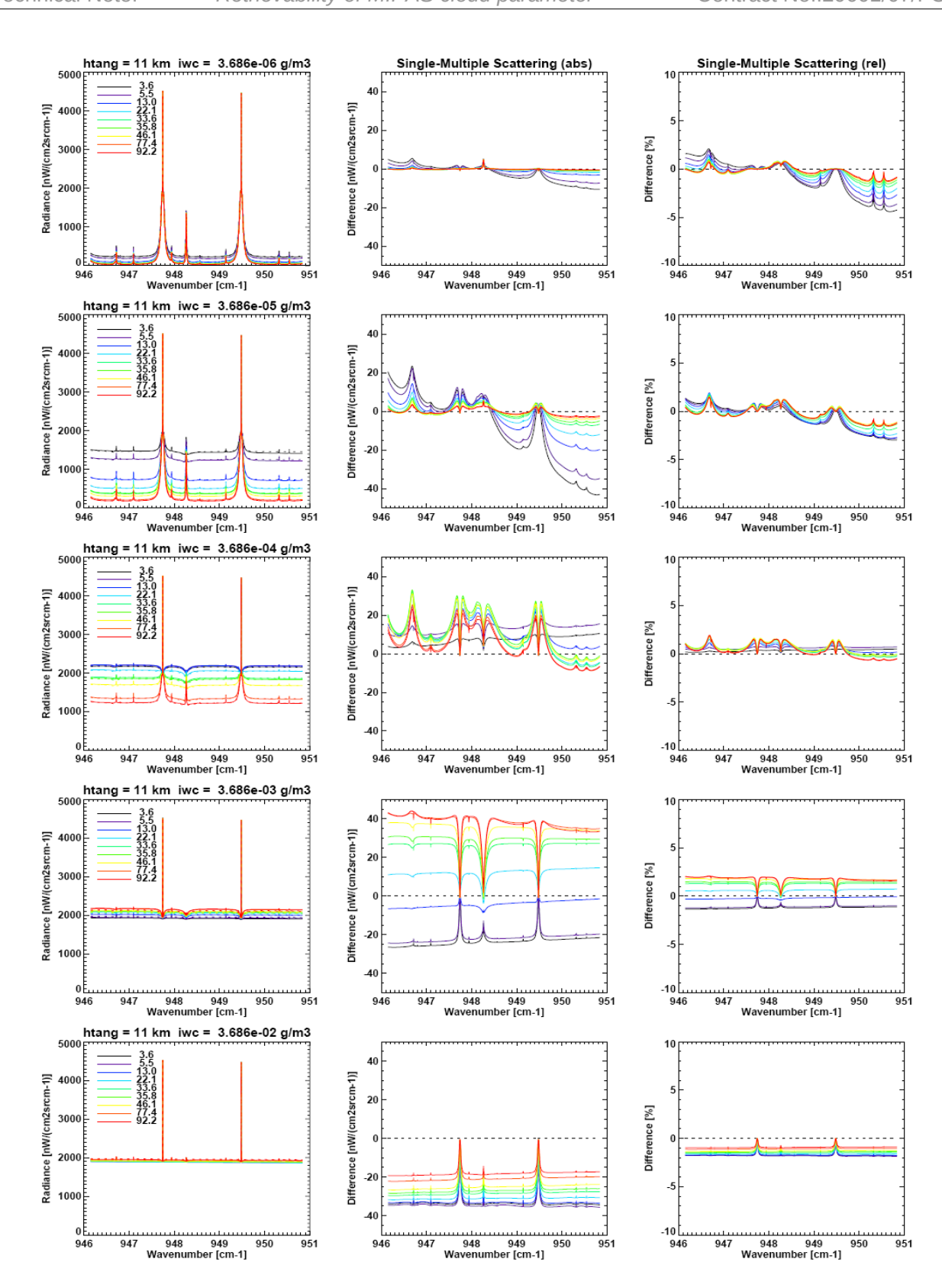


Figure 6: Comparison of single and multiple scattering models (KOPRA/FM2D) for various cloud scenarios. The 1st column show simulated spectra at 11km for a cloud centred at 11km. Solid lines show results for single scattering, whilst dashed lines show the multiple scattering results. Coloured lines are for different IWRE (as given in key), whilst each row is for different IWC. The 2nd and 3rd columns show absolute and relative differences respectively.

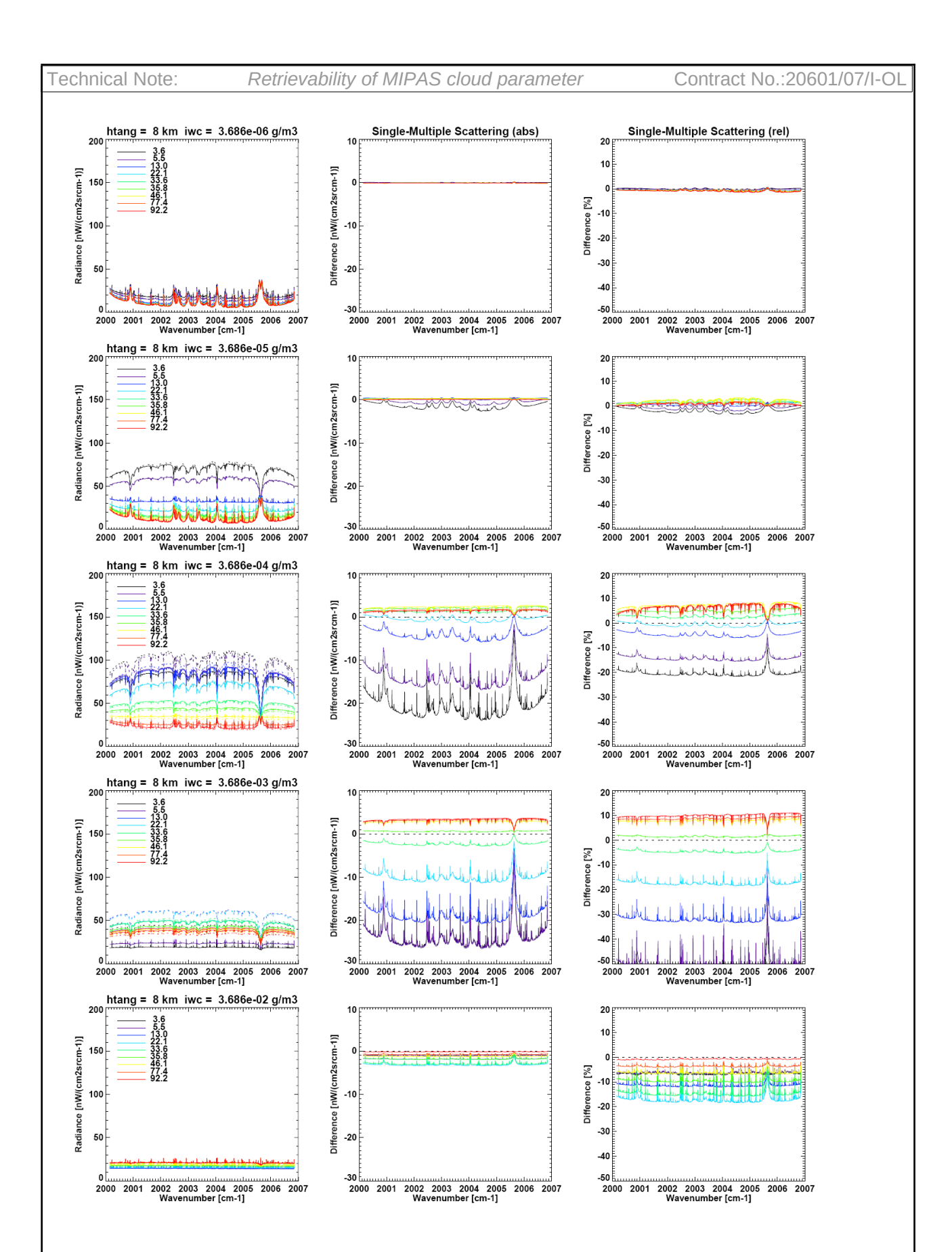


Figure 7: Comparison of single and multiple scattering models (KOPRA/FM2D) for various cloud scenarios. The 1st column show simulated spectra at 8km for a cloud centred at 11km. Solid lines show results for single scattering, whilst dashed lines show the multiple scattering results. Coloured lines are for different IWRE (as given in key), whilst each row is for different IWC. The 2nd and 3rd columns show absolute and relative differences respectively.

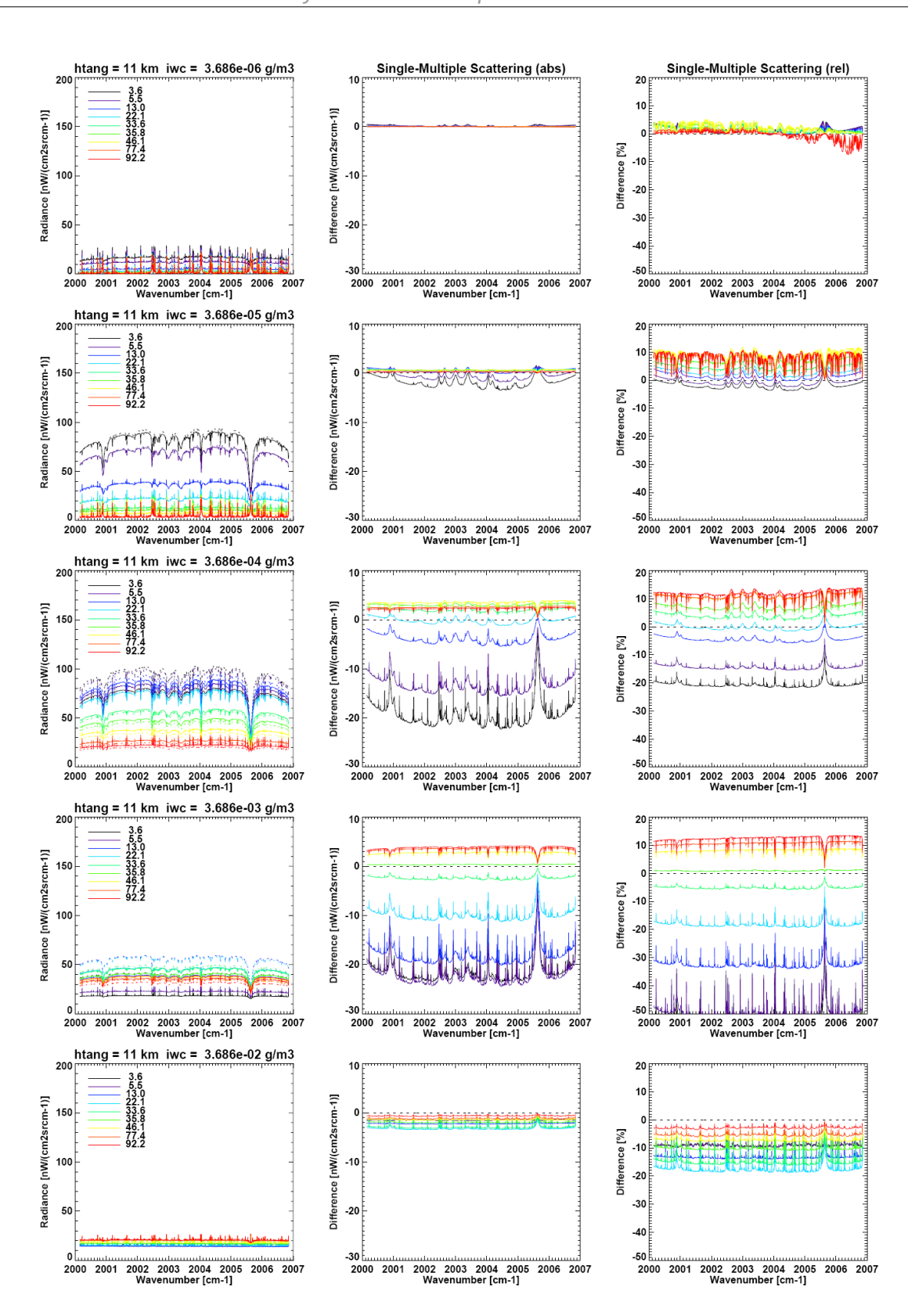


Figure 8: Comparison of single and multiple scattering models (KOPRA/FM2D) for various cloud scenarios. The 1st column show simulated spectra at 11km for a cloud centred at 11km. Solid lines show results for single scattering, whilst dashed lines show the multiple scattering results. Coloured lines are for different IWRE (as given in key), whilst each row is for different IWC. The 2nd and 3rd columns show absolute and relative differences respectively.

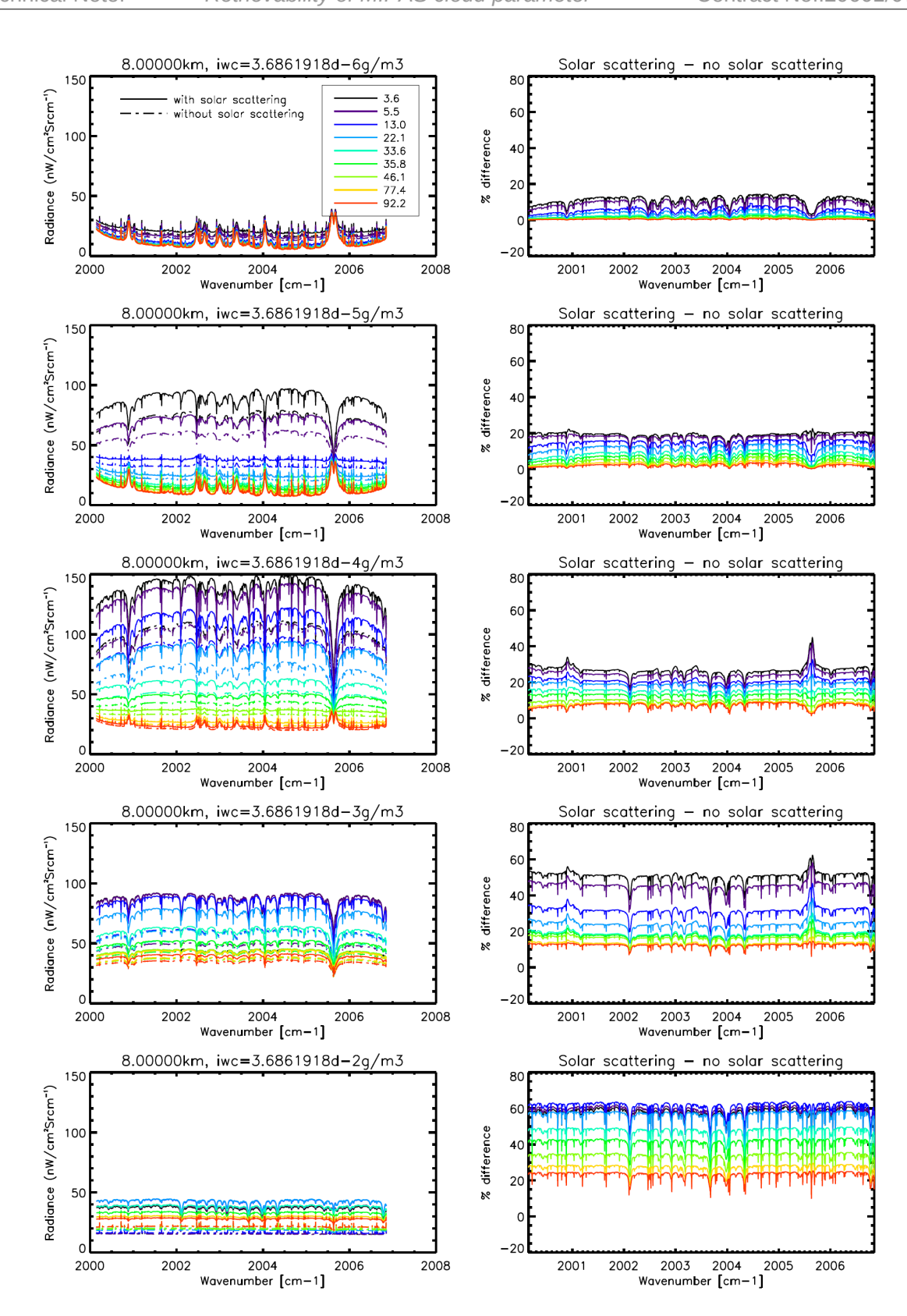


Figure 9: Comparison of multiple scattering simulations including / not including solar scattering. Solar scattering was included for a solar zenith anle of 45 and a relative azimuth of 60. The 1st column show simulated spectra at 8 km for a cloud centred at 11km. Solid lines show results for simulations including solar scattering, whilst dashed lines show the results when solar scattering is neglected. Coloured lines are for different IWRE (as given in key), whilst each row is for different IWC. The 2nd column shows the relative differences.

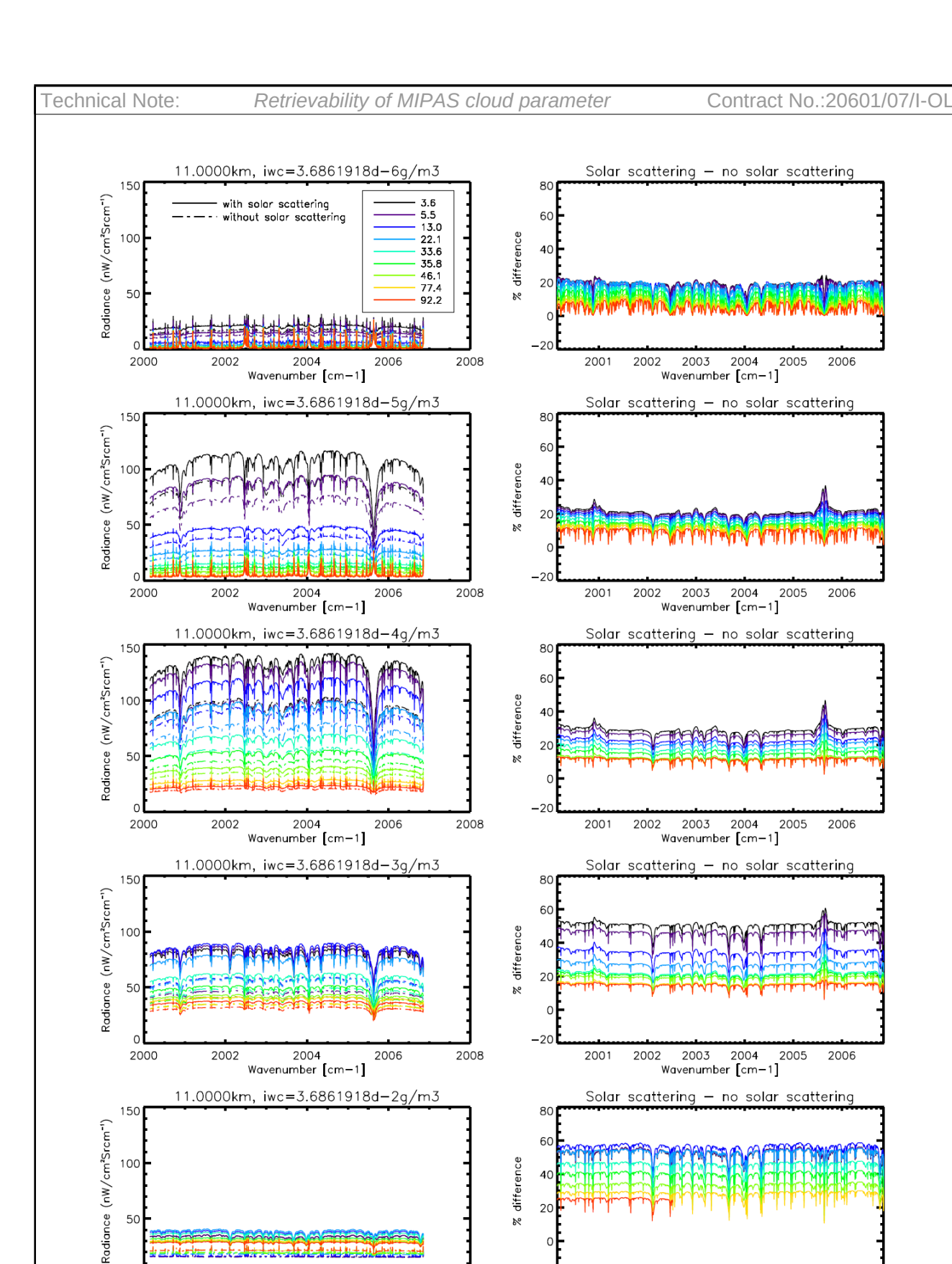


Figure 10: Comparison of multiple scattering simulations including / not including solar scattering. Solar scattering was included for a solar zenith anle of 45 and a relative azimuth of 60. The 1st column show simulated spectra at 11 km for a cloud centred at 11km. Solid lines show results for simulations including solar scattering, whilst dashed lines show the results without solar scattering. Coloured lines are for different IWRE (as given in key), whilst each row is for different IWC. The 2nd column shows the relative differences

Wavenumber [cm-1]

Wavenumber [cm-1]

2.8 Technical definition of the database format

For the moment the cloud databases are stored as structured variables in idl-save files since all members of the study group use idl. The following sheet shows the format of the structures.

Format of the PSC spectra database idl-sav-files

1) Wavenumbers

2) Reference spectra without PSCs

```
IDL> restore, 'ref a.sav'
IDL> help,ref,/str
** Structure <83691ec>, 8 tags, length=48, refs=1:
                                                                                                                                                                         ; cloud type: '0' for reference spectra without
                                                          STRING '0'
clouds
         X VERS
                                                                  STRING
                                                                                                                                                                         ; version of the calculation
         L_LOWER_CLOUD_TOP
                                                                FLOAT = 0.00000 ; altitude of tropospheric opaque clouds
(determining the upwelling radiation) [km]
          T_NAME_PT STRING 'wi001'
G_NAME_VMR STRING 'wi01'
                                                                                                                                                                         ; name of the used pressure-temperature profile
                                  SIRING 'wi01' ; name of the used pressure-t

LONG 17 ; number of tangent altitudes

POINTER <PtrHeapVar3> ; tangent altitudes [km]

POINTER <PtrHeapVar4> ; spectra for each tangent of tan
                                                                                                                                                                        ; name of the used vmr profiles
          NTANG
          HTANG
                                                                                                                                                                           ; spectra for each tangent altitude [nW/(cm2 sr cm-
1)], first index: on wavenumber grid, second index: on tangent altitude
IDL> help,(*ref[0].htang),/str
 <PtrHeapVar3>
                                                    DOUBLE
IDL> help,(*ref[0].spec),/str
<PtrHeapVar4> FLOAT
                                                                                = Array[5489, 17]
```

3) Spectra with PSCs

Format of the database continue

```
D CLDTHK
                   DOUBLE
                              0.50000000 ; cloud thickness [km]
   R RADIUS
                                                ; particle mean radius [um] (log-normal distribution)
                   FLOAT
                                    1.00000
   V VOLUME DENSITY
                   FLOAT
                                      10.0000 ; particle volume density [um^3/cm^3]
                   DOUBLE
                                9.1710000e-06; particle ice water content [g/m^3]
   N NUMBER DENSITY
                   DOUBLE
                                       1.5922898 ; partice number density [cm^-3]
                                   0.300000 ; width of lognormal distribution
   W WIDTH
                   FLOAT
                                                : version of the calculation
   L LOWER CLOUD TOP
                   FLOAT
                                      0.00000 ; altitude of tropospheric opaque clouds (determining
the upwelling radiation) [km]
   т маме рт
                   STRING
                              'wi001'
                                               ; name of the used pressure-temperature profile
                                               ; name of the used vmr profiles
   G_NAME_VMR
                   STRING
                              'wi01'
                                              ; name of the used vmr profile
; number of tangent altitudes
; tangent altitudes [km]
; spectra for each tangent all
                   LONG
                                         1
   NTANG
   HTANG
                   POINTER
                             <PtrHeapVar1>
                   POINTER
                             <PtrHeapVar2>
   SPEC
                                                ; spectra for each tangent altitude [nW/(cm2 sr cm-
1)], first index: on wavenumber grid, second index: on tangent altitude
```

2.9 Graphical display of the database parameters

Model runs with KOPRA (IMK) for the CSDB have been performed, whereby spectra for cloud-free, sulfuric ternary solutions (STS), nitric acid trihydrate (NAT) and ice has been considered. A first version of the CSDB for PSCs is now finished. Due to the large range of various parameter (in volume, radius, number density, altitude of cloud, thickness of cloud layer, tangent height altitude) the number of scenarios per PSC type is quite large. This is producing a huge amount of single spectra. An overview of the varied cloud parameter is shown in Figure 11. More than 2500 scenarios and around 25000 spectra per particle type were computed inclusive Jacobian spectra for retrieval studies. This is creating a unique dataset for testing the retrievability of cloud parameter.

2.10 Overview/status CSDB

- The PSC database as described above is finished and has been distributed in Dec. 2007
- The preparation for the Cirrus database took more time than expected for different reasons:
 - O There is more experience with modeling of PSC spectra than for cirrus. It was necessary to perform comparisons of the optical properties to be used for database creation.
 - O The IMK forward model had to be adapted to the bulk optical properties selected.
 - O Extensive comparisons between the fast single and the computationally more expensive multiple scattering model had to be performed.
- The model runs for the databases (PSC, cirrus, liquids, stratospheric and tropopsheric aerosols) are finished and distributed to all partners.

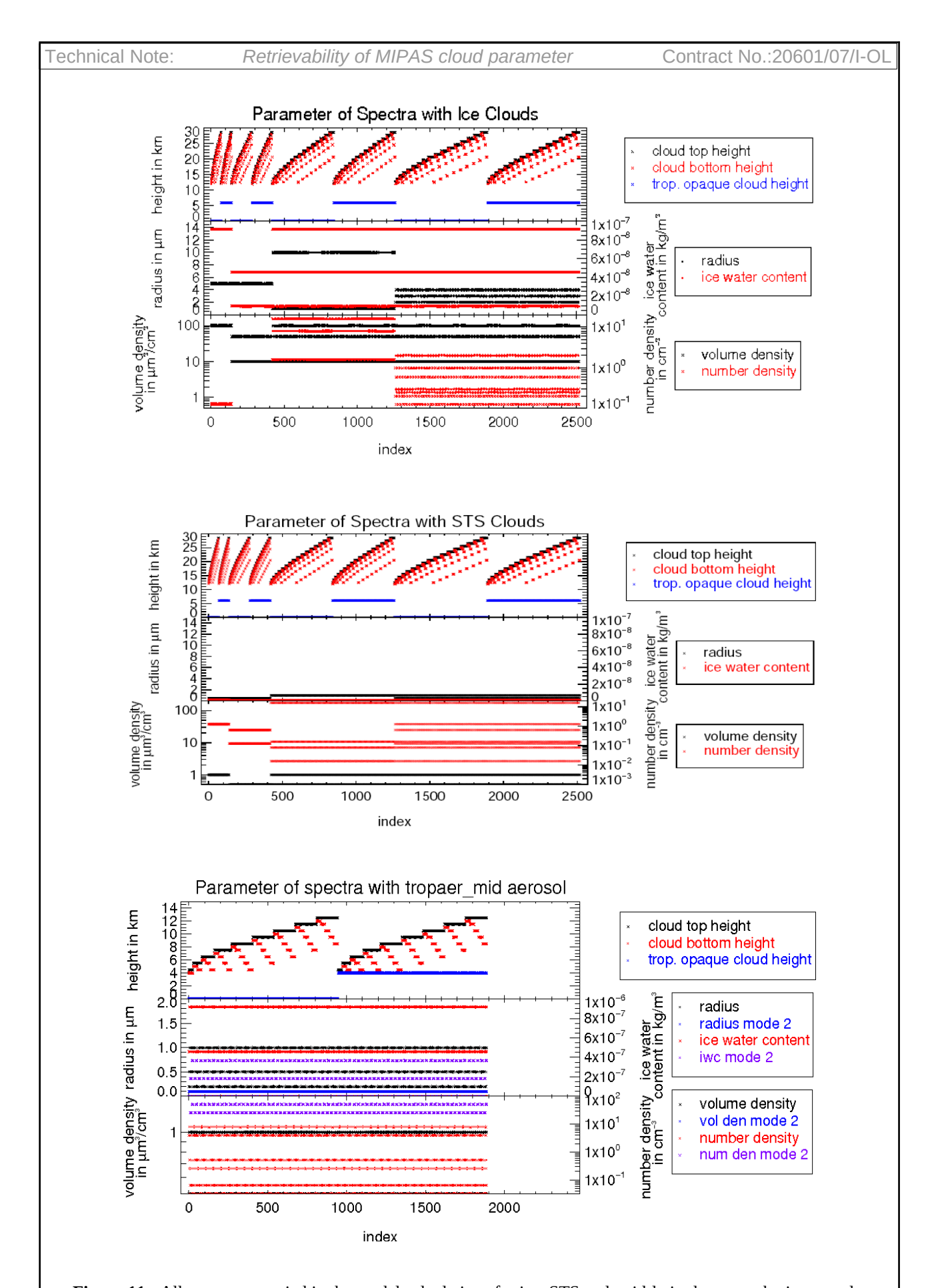


Figure 11: All parameter varied in the model calculations for ice, STS and mid-latitude tropospheric aerosols.

2.11 3D scattering model development

2.11.1 Introduction

3D simulations are required to address the specific question of how important the neglect of 3D effects are for cloud retrieval. It is intended that a 3-D RT model developed by RAL will be used to generate radiances from realistic 3-D cloud scenarios. These will be compared to radiances computed for the same field using 1D radiative transfer. Finally, the impact of 3D effects on retrievals will be assessed by applying the developed cloud schemes to the reference set of 3D radiances.

The FM2D model which was originally developed at RAL during the ESA UT/LS study (Kerridge, 2002) and provides weighting functions for all necessary optical properties and can simulate both solar and thermal radiative transfer simultaneously. The model evolved from a line-by-line thermal emission code for simulating limb geometry radiative transfer to include multiple scattering modules which are based on the GOMETRAN++ radiative transfer model (Rozanov et al., 1997), which is itself based on the finite difference method. As its name suggests the code can simulate the effects of horizontal atmospheric structure, however this is done under the assumption that the scattering source function can be solved locally along the line-of-sight using the plane parallel approximation (see Figure 12). FM2D then integrates the radiative transfer equation using the source functions local to each point along the path. This approximation enables rapid plane-parallel model to be used to accurately simulate 1-D limb scattering and approximate some of the aspects of 3-d structure.

To overcome limitations of this approximation for simulating 3-d cloud effects in 3-d, the fully 3-dimensional radiative transfer model SHDOM¹ has been interfaced to FM2D, in place of GOMETRAN++. The spherical harmonic discrete ordinate model (SHDOM) is described in (Evans et al. 1998). The method uses a spherical harmonic angular representation to reduce memory use and time computing the source function in 3-dimensions. After solving for the source function, the radiative transfer equation is integrated along discrete ordinates through a spatial grid to model the streaming of radiation. An adaptive grid approach, which places additional points where they are most needed to improve accuracy, is implemented. The solution method is a type of successive order of scattering approach or Picard iteration. The model computes accurate radiances or fluxes in either the shortwave or longwave regions, even for highly peaked phase functions. SHDOM has been recently used at RAL to model nadir uv-vis/mid-ir spectra in the context of a Eumetsat study to define requirements for a potential O₂ A-band channel for Meteosat Third Generation. A limitation of SHDOM is that it assumes a 3-d rectangular grid. I.e. it neglects the curvature of the Earth and it is therefore unsuitable as it stands to simulate limb radiances.

In the context of this study this problem has been overcome by interfacing SHDOM to FM2D: FM2D will povide trace-gas and cloud optical properties (as used elsewhere in this study to generate the main CSDB). SHDOM will then provide the 3-D scattering source function (neglecting Earth sphericity). Finally FM2D will perform the line-of-sight integration of the radiative transfer calculation in spherical geometry using the computed source function. This will yield highly accurate limb spectra incorporating full 3-D multiple scattering for use as reference spectra to test the developed cloud retrieval schemes. The model is capable of running with the same input data in various levels of approximation, including reproducing the local 1-d plane parallel approximation (as simulated by FM2D/GOMETRAN) and an intermediate approximation: 1-d plane-parallel for the diffuse radiation but 3-d for direct solar scattering.

2.11.2 Generation of 3-D cloud fields

In previous studies 2 approaches have been used by RAL to construct cloud field with realistic horizontal structure.

In the UT/LS study, ECMWF cloud data data was used. The ECMWF operational analyses provide the following cloud parameters:

- The mass mixing ratio of liquid-water and ice within the model box.
- The horizontal fraction of the (now ≈ 30 × 30 km) model box which is occupied by cloud. Where present, cloud is assumed to occupy the whole of the vertical extent of the model box.

It is important to note that the mass-mixing ratios correspond to the whole box, only a fraction of which is cloudy. I.e. the density of liquid/ice water within the cloud, where present, is given by the ratio of the liquid/ice-water content and the horizontal fraction. Furthermore, the impact of the same mass of cloud-water within a box depends strongly on horizontal distribution of cloud within the box. If the cloud fraction is high, then the distributed cloud may be optically thin and of little consequence for the limb sounder; if the the fraction is very low, then the cloud may be optically thick, but has a small horizontal extent and will not necessarily be sampled by a limb-view. Radiative transfer is non-linear so it is not adequate, e.g., to ignore the cloud fraction and always consider the cloud to be distributed evenly through the box, even for a statistical evaluation of limb optical depths.

Cloud fields at finer spatial resolution than the ECMWF model data were constructing by assuming that cloud fields follow a $1/v^2$ power law distribution, where v is the spatial wavenumber. This statistical model of cloud occurrence is based on observational data². The model represents cloud as being random at coarse spatial scales but more homogeneous over fine scales: Given a point A which is cloudy, the likelihood that point B is also cloudy increases as the separation between A and B decreases.

The application of this assumption to derive realistic cloud fields at spatial scales finer than the ECMWF model box is illustrated in Figure 13. ECMWF cloud horizontal fractions are converted to a possible high-resolution cloud field, consistent with the power law distribution, as follows:

- **1.** A cloud distribution field is constructed by generating a random image which follows a $1/v^2$ power law distribution. In the example, this field is chosen to have 16 "pixels" in the across-track dimension and 16 times the number of model-boxes along the orbit track. The image therefore over-samples the along-orbit ECMWF data by a factor of 16 in both directions and therefore has a resolution of approximately 2 km.
- **2.** The binary decision as to whether any one of the pixels within each model box is cloudy is taken by choosing a threshold value for the cloud distribution field. Where the cloud-field value is above the threshold the pixel is taken to be cloudy, where the cloud-field value is below, the pixel is assumed cloud-free. Thresholds are chosen separately for each model box (and altitude) such that the fraction of cloudy pixels agrees with the ECMWF horizontal fraction for the box (subject to the digitisation error associated with the 16×16 binary grid used to represent the model box).

In the Eumetsat oxygen A-band study, realistic 2D cloud fields of optical properties were constructed using the CloudNet data (see section under validation data below), using a fixed wind-speed assumption to translate the height vs time ground-based cloud measurements into cross-

² J.P.V Poiares Baptista and W. Leibrandt. Earthcare - earth clouds, aerosols and radiation explorer. *ESA Report for Assessment SP-1257(1)*, 2001.

J.C. van den Heuvel, M.L. Driesenaar, and R.J.L. Lerou. Fractal properties and denoising of lidar signals from cirrus. *J. Geophys. Res.*, *D105*, 3975-3982, 2000

sections of height vs distance within the limb line-of-sight plane. This method could be extended to generate 3-d fields by assuming symmetry in two horizontal directions.

In both cases, optical models based on Mie theory for liquid cloud and aggregate particles for cirrus (Baran et al., 2001) were used to determine cloud optical properties (as will be the case in this study).

The preferred approach for this study is to use model cloud data, since it is inherently 3-D and has a spatial resolution consistent with the MIPAS horizontal resolution (especially in the along-track direction). The UT/LS study already showed that the ECMWF model cloud was realistic in comparison to SAGE-II climatology and this has been confirmed by independent comparisons with e.g. MLS and CloudSat data. The ground-based data has the disadvantage of being preferentially sensitive to the cloud-base rather than cloud-top (which is most relevant to limb sounding).

Within the context of new externally funded studies in support of the PREMIER mission RAL is likely to acquire fields from a cloud-resolving model. I.e. model cloud fields at much finer scale than the ECMWF operational model. It may be possible to use these fields rather than ECMWF data in this study (TBD).

2.11.3 Example Results

Most features of the FM2D/SHDOM model are well tested by using the code to simulating visible images of structured cloud fields as seen from above the surface. (Solar scattering clearly reveals correct representation of shadowing and appropriate handling of phase functions in a manner which is less immediately clear with ir calculations which are dominated by emission and diffuse scattering.)

Figure 14 and Figure 15 show two cloud fields that have been used in initial tests of the code (one based on ECMWF data as described above, the other a simple box cloud). These images are created by running FM2D/SHDOM for 3 wavelengths which correspond to red, green and blue visible light and constructing the RGB composite image from the returned (sun-normalised) radiances. Images are for 9 am local solar time with a solar azimuth angle of 60 degrees, clockwise wrt to the vertical of the plotted images. Since the sun is relatively low, cloud shadows can be observed in these images. The surface reflectance at the 3 wavelengths is set to RGB = [0.05, 0.3, 0.1], hence the green colour of the observed surface. The cloud-free model atmosphere assumed standard mid-latitude, temperature, pressure (hence Rayleigh scattering), H_2O , and O_3 profiles. Maritime aerosol with optical depth 0.02 is assumed to be present within the bottom 2km only. These images could have been readily produced by SHDOM without code modification (other than to generate the necessary input optical properties).

Figure 16 shows images computed using FM2Ds spherical LOS integration to give radiances from with the cloud field, viewing above and below the horizon (i.e. including in the limb), from 10m and 3km altitude, at just after sunrise and at 9am. Note that directly transmitted solar radiation is not included in these plots (i.e. the sun itself is absent from the images, only scattered light is shown). A disk around the sun position is visible in the 10m altitude scenes due to the forward scattering of the background aerosol. The 3km scenes are viewed above the aerosol layer, leading to a bright apparent "reflection" of the sun for the aerosol below.

Finally, Figure 17 and Figure 18 show limb thermal emission calculations for the two cloud scenes, for the 12 micron spectral region (with clear-sky absorption computed using the RTTOV model of the SEVIRI 12 micron channel).

Figure 12:Schematic illustration of 3-D radiative transfer (RT) in spherical geometry. Each panel shows a cloud (white) and water vapour (blue) field (both derived from ECMWF data) over a surface, as a function of horizontal distance and altitude. The black line shows a limb line-of-sight (LOS) which is a parabola within this coordinate system. The radiance observed in the limb is computed by dividing the LOS into sections and at each point (one of which is illustrated), evaluating the scattering source function (blue). As illustrated in the top panel, this involves determining the incoming atmospheric/surface (purple) and solar (yellow) radiation in all directions, then integrating these over the scattering phase function. RT is complicated by the fact that scattering must be also be accounted for in modelling each of the rays arriving at each point along the LOS. Approximate methods are required to solve the otherwise potentially circular problems. The middle panel illustrates the solution now implemented using SHDOM to compute the source function. SHDOM adopts an iterative approach to compute the complete scattered radiance field at all locations and directions. However sphericity of the Earth is neglected (NB purple lines in the middle panel are straight not parabolic). FM2D however traces the limb path in spherical geometry, extracting the source function at the required angles along the LOS. The bottom panel illustrates the previous approximation employed by FM2D prior to this study, whereby the 1-D plane-parallel model GOMETRAN++ was used in a similar way to compute the source function. In this case, at each point along the LOS the scattering field is assumed to be horizontally invariant in order to compute the source function (although the scattering profile local to each point along the LOS was used to compute the local source function and extinction / emission along the path was fully modelled in 3d).

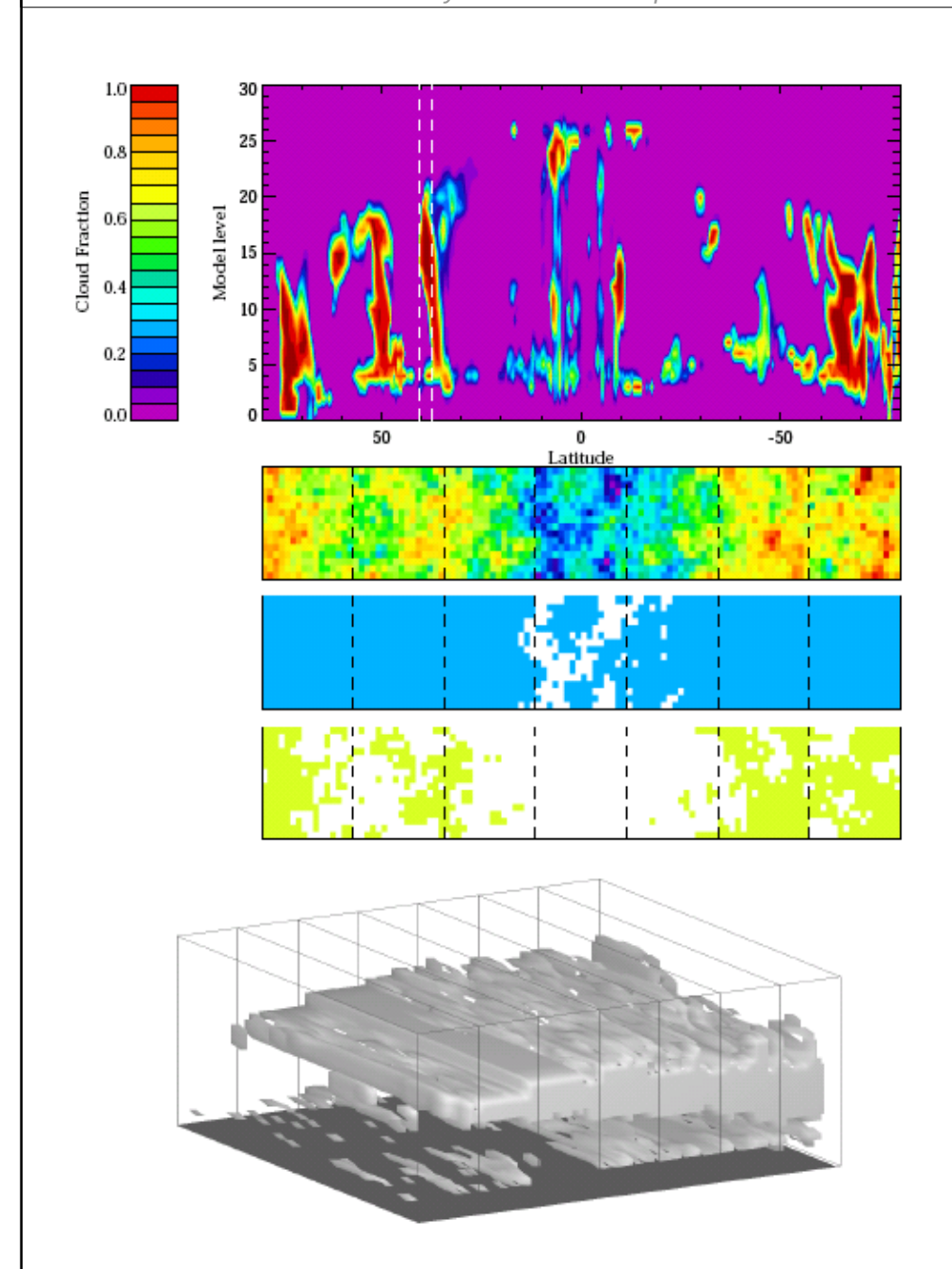


Figure 13: Cloud fields at sub model-box resolution. The derivation of cloud fields at sub model-box resolution. To panel shows the ECMWF cloud horizontal fraction orbit cross-section. Dashed vertical lines indicate the area of interest considered in the panels beneath. Centre panel shows a cloud field (arbitrary units) constructed to follow a random 1/v2 power law distribution. This field over-samples the ECMWF model boxes by a factor 16 in each direction, the horizontal extent of the model boxes considered is delimited by the dashed lines. Bottom panel shows a cloud field for the same model boxes constructed by the method described in the text.



Figure 14: "True-colour" nadir-viewing image calculated by SHDOM assuming a pseudo-random cloud field based on ECMWF model data. Solar viewing conditions correspond to 9am local solar time, with solar azimuth of 60 degrees measured clockwise from the vertical (hence observed shadows in nadir image).

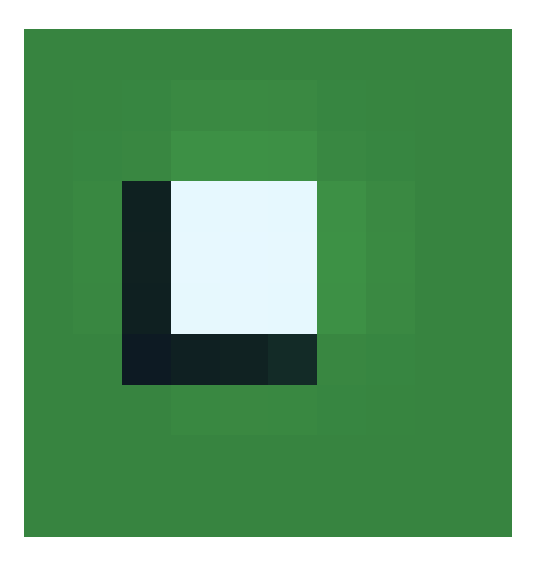


Figure 15: Similar true colour image for a simple square ice cloud, with triangular vertical profile peaking at 8km altitude with 1km full-width-half-maximum, optical depth 20 at 0.55 microns and effective radius 10 microns. Same solar conditions as previous figure.



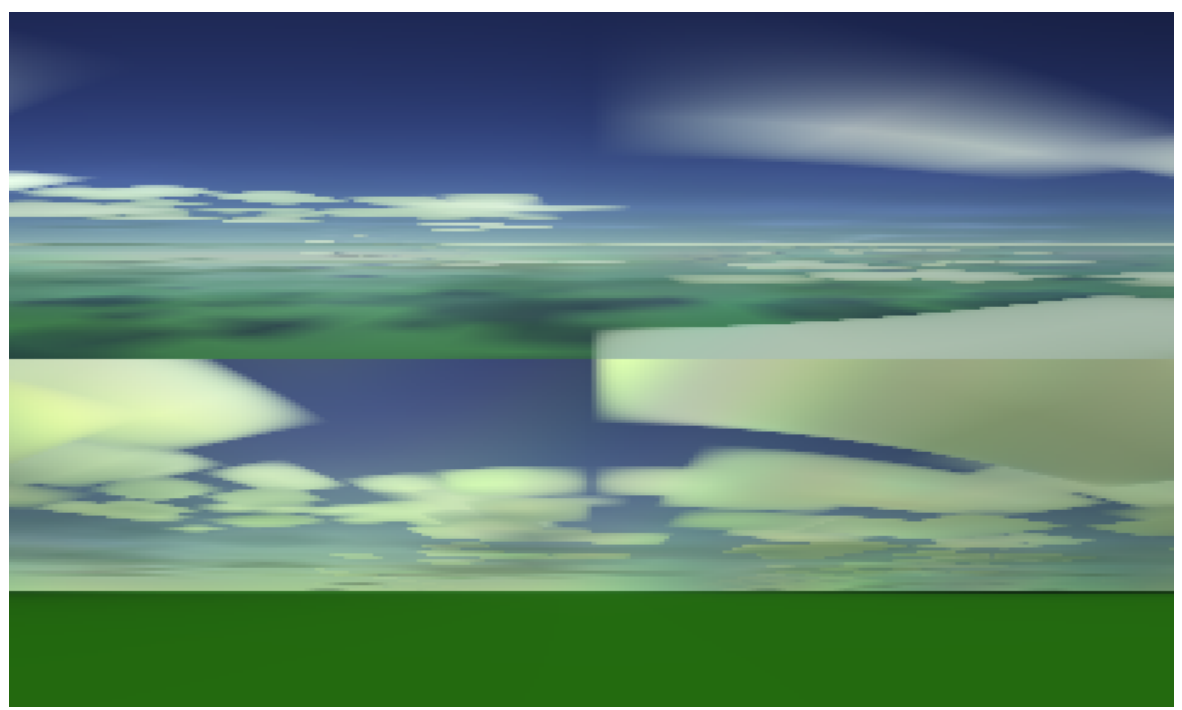


Figure 16: "True colour" images based on the cloud field shown in Figure 14. Horizontal position of the observed is 5 pixels in from the left hand edge of field and the centre vertically, viewing over a range of azimuth angles from 60 to 120 degrees (towards the right of Figure 14) and elevation angles from -10 to 20 degrees. Views from two vertical positions, 3km and 10m, are shown in each pane. The top and bottom panel shows the results at 06:20 and 09:00 local solar time, respectively.

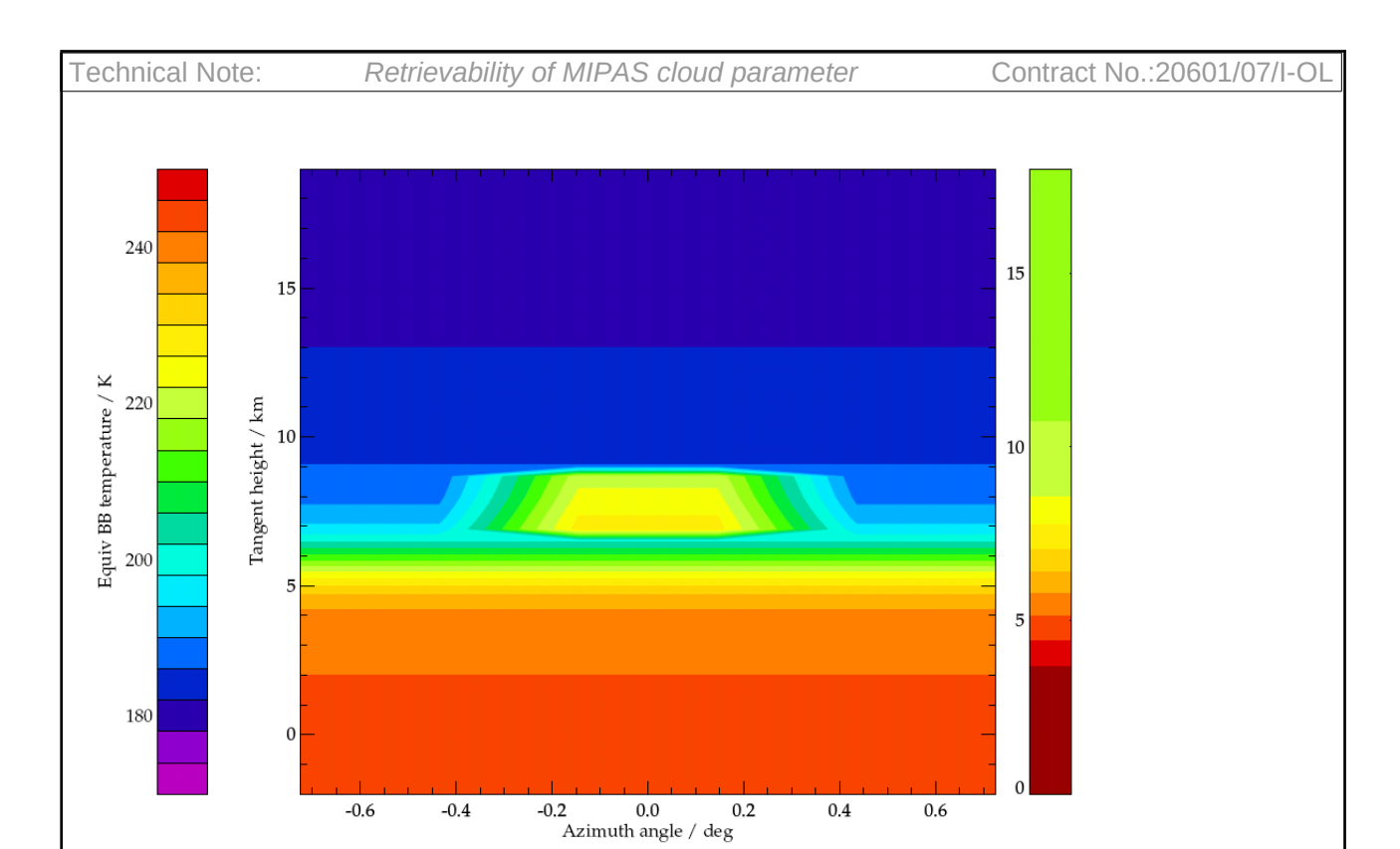


Figure 17: 12 micron limb sounder brightness temperatures (from 820km altitude) viewing the cloud shown in Figure 15. The bar on the right shows the atmospheric temperature profile on the same colour scale.

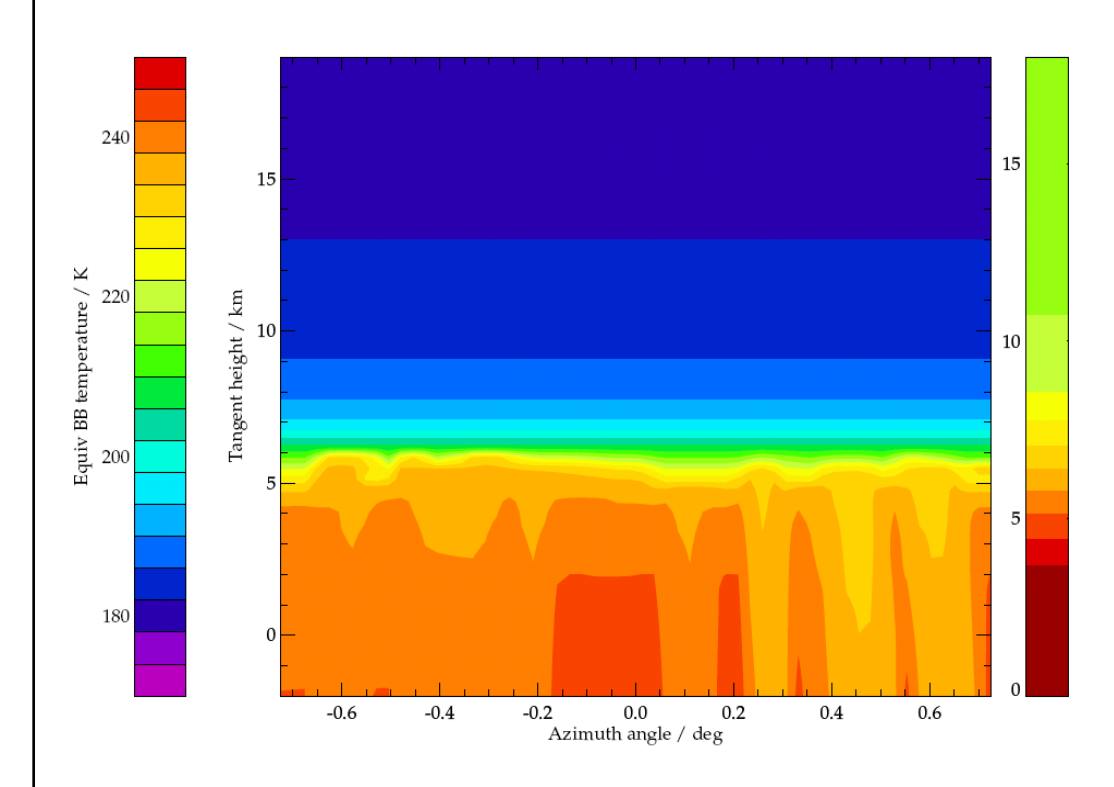


Figure 18: 12 micron limb sounder brightness temperatures (from 820km altitude) viewing the cloud shown in Figure 14 (observer to the left of the field viewing towards the right).

2.11.4 CPU times

FM2D/SHDOM solves RTE in two steps (i) SHDOM is used to compute the diffuse source for a complete 3-D field, in a directions (all grid points on which optical properties are defined and for each spherical harmonic); (ii) Once the diffuse source field is obtained, radiances in given viewing directions can be computed.

For the example illustrated in Figure 18 the complete run time was 494s, comprising

- 107s to compute the source field for the field with dimensions 40 x 40 (horizontal) x 21 (vertical) grid points.
- 342s to compute all the individual views shown in the figure i.e. 60 azimuth x 60 zenith angles = 3600 views.

	16	streams	were used t	o represent the	angular de	ependence o	f the	diffuse :	radiation	field.
--	----	---------	-------------	-----------------	------------	-------------	-------	-----------	-----------	--------

3. Cloud Identification

3.1 Operational Cloud Detection and Problems

Cloud detection is a fundamental quantity in the study of clouds enabling satellite systems, such as that for MIPAS, to supply essential information for cloud clearing, for scientific use, and for meteorological or numerical weather prediction systems. The original MIPAS cloud detection algorithm was designed by Remedios and Spang, 2002, and has been applied to a number of scientific MIPAS processors. The scheme is based on the ratio of integrated signals in cloud microwindow pairs (Spang et al., 2004) with one pair defined in each of 3 MIPAS bands (A, B and D). It was particularly suitable for MIPAS operational processing, as it is fast, does not involve iterative retrievals (to save CPU time) and classifies cloud influences on measured spectra independently of the altitude of the cloud.

The tests operate hierarchically so that the cloud index in band A (CI-A) is tested first, and then the other bands if required because of the unavailability of band A. Hence CI-A is normally the cloud index used. The microwindows and settings currently used in the MIPAS operational processor are shown in Table 15.

Cloud Index	MW1	MW2	Cloud Index	In-flight altitude
MIPAS Band	(cm ⁻¹)	(cm ⁻¹)	threshold	range
			value	(km)
CI-A	788.20 - 796.25	832.3 – 834.4	1.8	6-45
CI-B	1246.3 - 1249.1	1232.3 – 1234.4	1.2	10-40
CI-D	1929.0 - 1935.0	1973.0 - 1983.0	1.8	12-32

Table 15: Cloud detection settings for MIPAS

One of the distinctions of the cloud index approach is that it also allows an assignment of cloud top height (CTH) as the tangent altitude for which a cloud is detected in a MIPAS spectrum. An example of the global cloud top height map obtained from the analysis of 3 days of MIPAS measurements from 15 September 2002 is shown in Figure 19. The highest cloud heights are found, as expected, in the tropical upper troposphere (cirrus) and in the Antarctic polar vortex (polar stratospheric clouds). The polar stratospheric clouds in this period were the final ones observed prior to the unusually early break-up of the vortex in that year.

The cloud detection algorithm works well as a gross cloud test and should be implemented as a tool for users to apply to MIPAS spectra as required; operationally cloud index data will be calculated and output as part of the new level 2 processor but a specific tool will have more flexibility.

Although the cloud detection approach is well-justified, there are some necessary improvements. First of all, the thresholds given in Table 15 are those considered appropriate to "cloud clearing" as opposed to "cloud detection" for the purposes of cloud. For example, for PSCs, Spang et al. (2005a) validated the detection of PSCs against satellite and lidar measurements and demonstrated that CI-A with a threshold of 4.0 could be used to track the evolution of PSCs throughout a winter period. Spang et al. (2005b) extended this analysis to Antarctic winter 2003 and showed the differing characteristics of Antarctic versus Arctic winters with much stronger PSC intensities and more dramatic decline in cloud top threshold through the winter season in the Antarctic compared to the Arctic. The uncertainty in detection increases as CI-A increases, nonetheless Kramer (2004) showed that a threshold of 5.0 can be used for PSC detection (albeit of very low infrared opacity) in the Artic and Antarctic at altitudes between 15 and 24 km. Hence better thresholds need to be identified with the cloud detection tool such that these thresholds are appropriate to cloud particle identification.

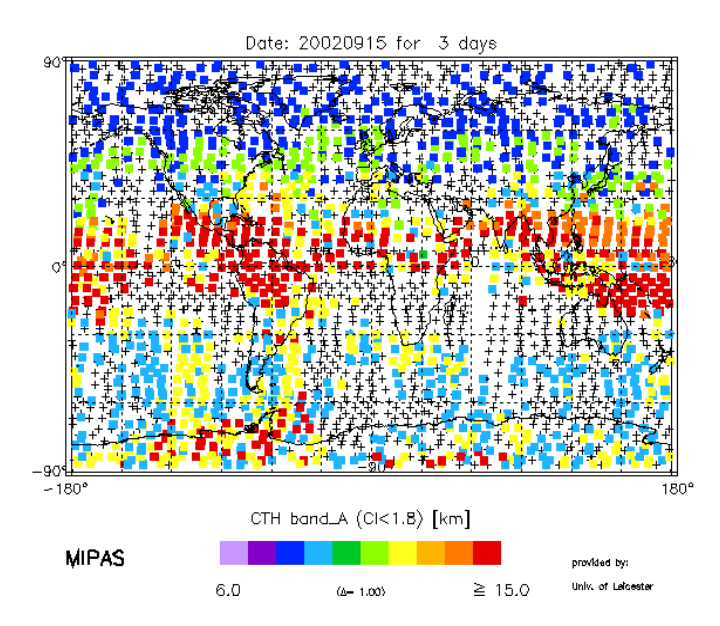


Figure 19: Global cloud top height map from MIPAS data (OL data) for three days from 15 September 2002. Plus signs (+) indicate limb scans for which no clouds were found, i.e. the entire profile was cloud free. The highest cloud heights are found, as expected, in the tropical upper troposphere (sub-visible cirrus) and in the Antarctic polar vortex (polar stratospheric clouds or PSCs). The PSCs in this period were the final ones observed prior to the unusually early break-up of the vortex in that year.

A second limitation to the cloud detection approach is that whilst CI-B, the index in Band B, correlates very well with CI-A, the correlation is less strong for CI-D (the cloud index for band D). This is particularly true at cold temperatures (less than 200 K) in which typically many PSCs and tropical cirrus occur. Even for CI-A, the uncertainty on a single determination of CI-A can increase to greater than 10% at temperatures of 180 K.

The interpretation of CI-D is also more difficult as CI-D is potentially more prone to solar scattering, suggesting that information on particle size might be present in certain MIPAS spectra. Finally, it is worth noting that there could be many microwindows with information on cloud particles and a flexible tool is desirable which can identify or comment on suitable microwindows.

3.2 Improvements for colour ratio based cloud detection

Work in this area is concentrating at looking at better thresholds for existing cloud indices, a better understanding of the relationships between cloud indices and more fundamental properties such as composition and cloud radius, and new simple cloud detection methodologies.

The objective of this work package is:

- to optimise the cloud identification thresholds (operational processor method)
- to investigate new cloud microwindow pairs

The work will examine the existing MIPAS operational method and microwindows and use histogram tests and simulations of clear sky radiance to demonstrate methods for deriving and values for cloud identification thresholds (CITs). The utility of simultaneous use of all current operational cloud MWs will be investigated (sequential hierarchical use only in current processor). The work will also investigate new cloud microwindow pairs using the spectra and Jacobians present in the CSDB in order to define windows which are 1) better and more robust indicators of cloud parameters, e.g. less sensitive to water vapour; 2) more sensitive to specific cloud microphysical parameters such as cloud composition and mean size. Additionally, the investigation will also focus on optimising the colour ratio approach in respect to detection sensitivity and extension of altitude.

Investigation of current spectral ratio techniques

A literature survey has been carried out to determine which infrared spectral regions that overlap with the MIPAS spectral range have been utilised as colour ratios and also which spectral regions are known to have ice particle/aerosol signatures.

(a) Spectral features observed in nadir and limb infrared emission and absorption spectra

Several methods such as Geometric ray-tracing (GOM1) or anomalous diffraction theory (ADT) can be used to determine the single scattering properties of ice crystals. Yang et al, (1997) used these approaches to examine the extinction efficiency and single scattering albedo particles with varying size distributions and found two significant extinction minima exist at wavelengths around 2.85 micron and 10.5 micron. These minima are associated with the extinction properties of ice crystals with small size parameters - (10 microns or less). Small ice crystals are important because they can contribute to/dominate solar albedo and infrared emission. Extinction efficiency and single scattering albedo are important properties to measure as they help to determine the optical depth and emissivity of cirrus clouds at IR wavelengths.

Also examined were the Christiansen bands where the extinction minima are produced by the strong absorption of ice coupled with the real part of the refractive index close to unity. Therefore the extinction minima are associated with absorption processes rather than scattering.

Similarly, Yang et al (2003) examined ice and water particle spectral signatures between 800 and $1200~\rm cm^{-1}$ using simulations of mixed-phase clouds. Certain features are seen in the $8-13~\rm micron$ ($1250-740~\rm cm^{-1}$) range and in particular the extinction, absorption efficiencies, optical thickness and brightness temperature of mixed-phase clouds are examined. For ice crystals, the greatest extinction efficiency of 2.2 is observed close to 8 microns, gradually reducing to 2 at 10 microns before dipping down to 1.4 at 10.5 microns. The curve gradually increases from 1.5 at 11 microns to 2 at 13 microns. For absorption efficiency, from 8 to 10 microns, it remains low (0.7 \sim) and then increases gradually from 10 to 13 microns over 0.7 to 1.1 range. The most significant impact on the spectral signature comes from smaller particles in mixed phase clouds.

Several studies have examined spectral features in infrared polar stratospheric cloud spectra in particular from the MIPAS-B and MIPAS-E instruments. Hoepfner et al (2002) examined MIPAS-B PSC emission spectra measured over Kiruna, Sweeden in which key features observed in the spectral regions of 800 to 1300 cm⁻¹ were a step-like feature from 819 – 825 cm⁻¹, side-lobes of CO2 features and inverted H2O lines at 950 and 1200 cm⁻¹. Hoepfner et al (2004) performed a simulation study of MIPAS PSC spectra using the IMK KOPRA model with varying aerosol/cloud parameters to determine the distinction between PSC signatures under specific conditions. For a mode radius of 0.1 microns: Some features around 1270 cm⁻¹ and 1450 cm⁻¹ are observed and thought to be signatures of NAD-spectrum. NAT peaks observed at 1390 cm⁻¹. For larger particles the biggest differences are in the 800 – 1500 cm⁻¹. PSC signatures are strongly related to particle size between 1 and 7 microns. Daytime/solar measurements scattering is more important above 1700 cm⁻¹ region and further.

More recently, Hoepfner et al (2006) investigated signatures of NAT, STS and ice in MIPAS spectra. Using simulations of MIPAS PSC spectra and comparisons to MIPAS Antarctic PSC spectra, certain features are fitted in this study. It is found that Beta NAT fits well in the 1220 – 1490 cm⁻¹ spectral range and there is possibly a NAD feature at 810 cm cm⁻¹. Based on refractive index calculations, NAT features are apparent at 820, 1380 cm⁻¹ and 1450 cm⁻¹.

(b) Colour ratios used in nadir and limb infrared emission and absorption spectra

Using an infrared 'split' window technique is suitable for determining signatures of cirrus clouds, ice particles and water droplets in cloudy spectra predominantly in nadir sounding instruments. For a bi-spectral approach, it is common for the 11 micron (~ 900 cm⁻¹) and 12 micron (~820 cm⁻¹) channels to be used due to a distinct spectral dependency of cloud absorption in this region. Giraud et al (2001) used this method in terms of brightness temperature differences to examine cloud signatures in spectra from the ATSR and POLDER instruments. Generally higher BTD's were related to semi-transparent liquid clouds and lower BTD's for cirrus clouds in the measured spectra.

An extension of the bi-spectral method is to use a tri-spectral technique (Ackerman et al, 1990; Strabala et al, 1993) to allow better recognition of cirrus and water clouds and cloud properties in nadir infrared spectra. The BTD's calculated from the 8, 10, 11 and 12 micron regions can be useful in indicating cloud signatures because of the low trace gas absorption in these regions with the 8 micron region included to allow for weak water vapour effects. The tri-spectral method consists of examining the BTD scatter between the 8 – 11 micron channels against the 11 -12 micron channels. Generally, it is found that cloud-free regions have negative difference in BT8-BT11 due to absorption by near surface water vapour and positive differences due to optical properties of ice. Differences between 11 and 12 microns are positive whether viewing cirrus or clear sky. Addition of 8 microns removes any ambiguity in using 11 and 12 only.

Using the colour ratio method in limb spectra can be done by using similar spectral regions to obtain a spectral ratio that indicates cirrus signatures without conversion to BTD units. Spang et al (2001) described a colour ratio for high resolution CRISTA spectral measurements that consisted of the mean radiances in 788 – 796 cm⁻¹ region divided by the mean radiances in the 832-834 cm⁻¹ region (CR-CI). These regions were specifically chosen because of weak trace gas absorption, weak temperature effects and strong cloud and aerosol emission signatures and are used in the MIPAS operational cloud detection method. Spang and Remedios (2003) enhanced the use of this colour ratio for the detection of polar stratospheric cloud spectral signatures in the 820 cm⁻¹ region. Observing the spectral features in radiance enhancement (RE) of 819-821 cm⁻¹ /788- 796 cm⁻¹ against the CR-CI can show RE's are related to NAT particles for PSC's. Spang et al (2004) extended this analysis to use the MIPAS CI further to determine a scattering index to indicate absorption lines in emission spectra. The cloud scattering index (CSI) is calculated as (803.50-803.60) – (803.70-803.90)/ (803.50-803.60) +(803.70-803.90) where negative values indicate the presence of an absorption line and therefore scattering.

Recently, Spang et al (2007) have used the BTD method traditionally used for nadir spectral cloud examinations in the limb measurement mode to detect clouds and upper troposphere water vapour contributions. This can distinguish between continuum contributions by cloud extinctions and water vapour. The spectral regions of interest for this method are the brightness temperatures in the microwindows of MW1 = 784 – 785 cm⁻¹ and MW2 = 787-788 cm⁻¹. The BTD is calculated as MW1/MW2 and the relationship against the CR-CI can be examined. For background aerosol/low cloud extinctions – BTD tends to increase with increasing water vapour to maximum of 40 K. Large mixing ratios and lower altitudes the increasing water vapour continuum and lower transmission reduces the BTD as a consequence the CI ratio. Under conditions of enhanced extinctions but mean water vapour mixing ratios, the CI-BTD is under a transition zone of low water vapour/extinction and high water vapour/extinction.

Infrared spectral signatures of clouds/aerosol/H₂O in the MIPAS infrared spectral range

Figure 20 summarises colour ratios and spectral regions of potential interest to this study. It can be seen that the majority of microwindow pairs lie within MIPAS band A and modifications of microwindow regions if necessary can be within this range. For discovery of new colour ratios, it is possible to look for patterns of radiance enhancements near regions of distinctive spectral features

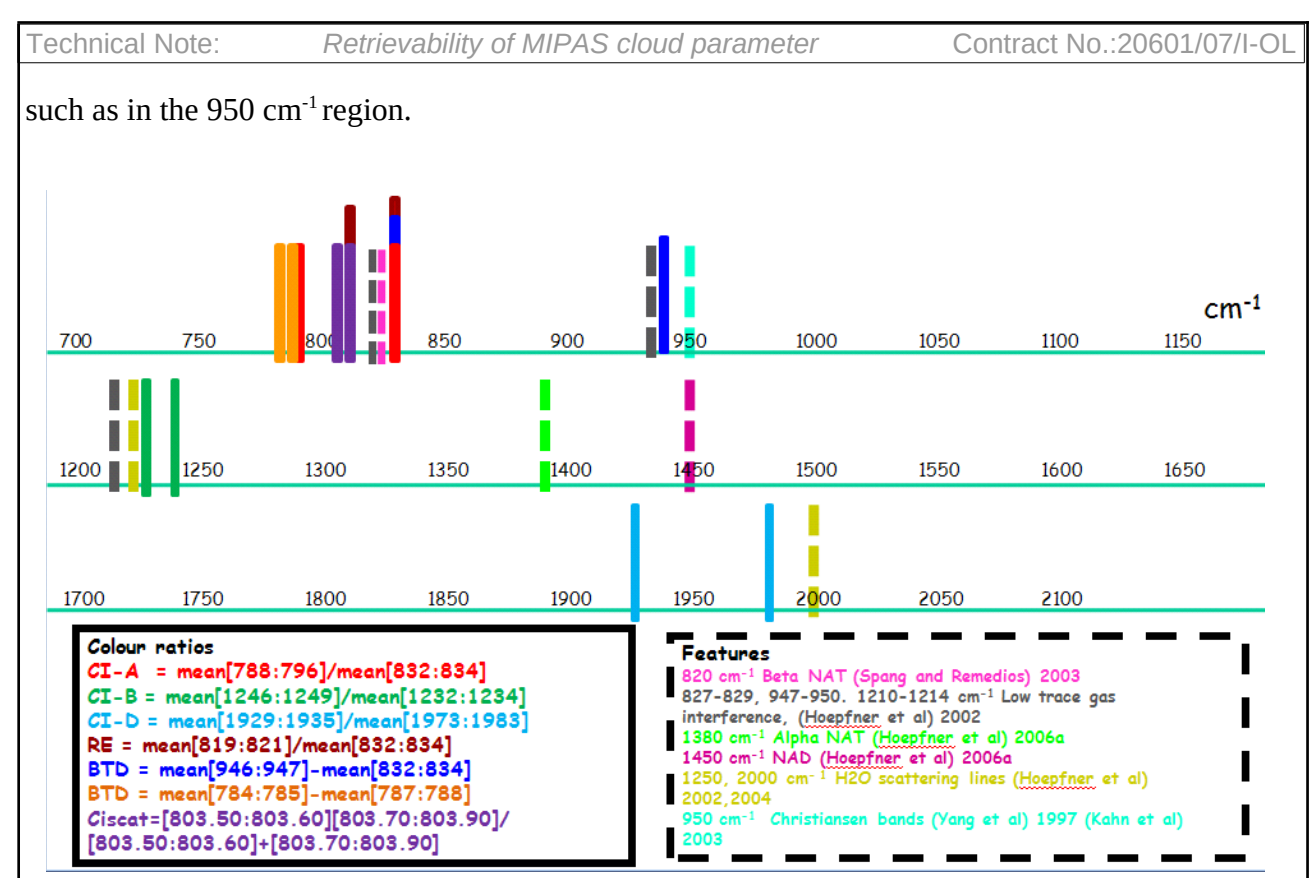


Figure 20: Summary of infrared spectral signatures of clouds, water vapour and aerosol in the MIPAS spectral range. In the diagram, solid lines of matching colours denote microwindow pairs and dotted lines denote spectral features.

3.2.1 Application of methods to the CSDB

Using the results of the survey above, infrared spectral ratios and spectral regions that hold spectral signatures of ice particles can be used to infer more robust or new cloud microwindow pairs for MIPAS cloud detection.

In this investigation several conventional and new cloud ratios are tested:

- MIPAS CI-A = mean [788:796]/ mean [832:834]
- MIPAS CI-B = mean [1246:1249]/ mean [1232:1234]
- MIPAS CI-D = mean [1929:1935]/ mean [1973:1983]
- RE 1 = mean [819:821]/mean [832:834]
- RE 2 = mean [948:952]/mean [832:834]
- RE 3 = mean [1247:1250]/mean [832:834]
- BTD = mean [946:947] mean [832:834]
- CSI = [803:50:803.60]-[803.70:803.90]/[803.50:803.60]+[803:70:803:90]

The second focus of this study is to examine the altitude dependency, if any, in these colour ratios when applied to the spectral database.

Colour ratios and radiance enhancements: Investigation on tropical and mid-latitude cirrus

In this section, various combinations of the colour ratios discussed above have been applied to the mid-latitude cirrus, mid-latitude liquid clouds and the tropical cirrus clouds CSDB spectra.

Mid-latitude liquid clouds



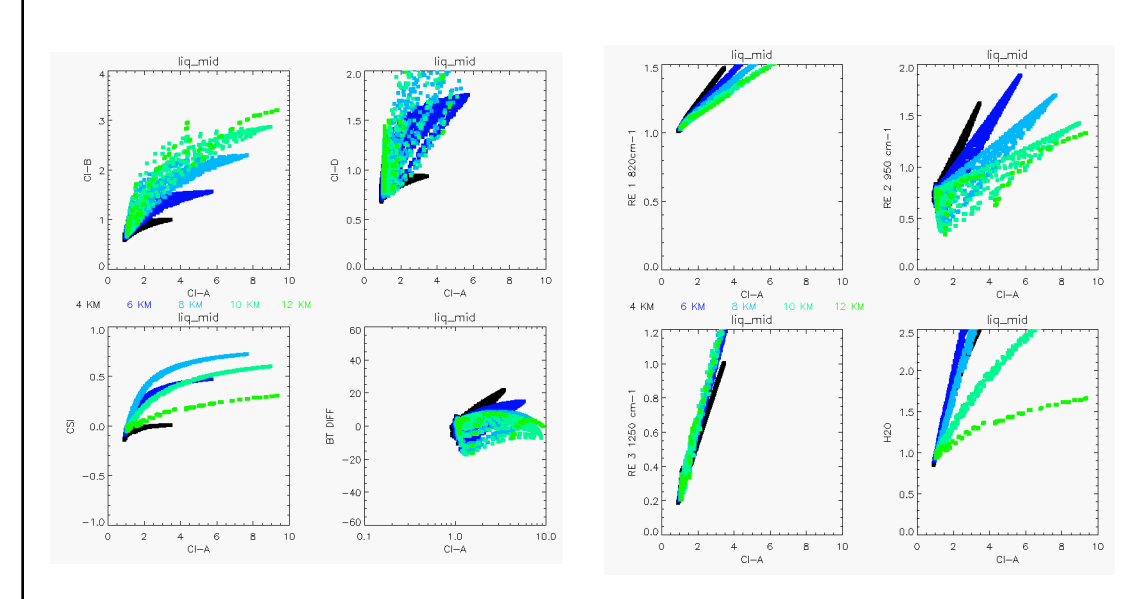


Figure 21: Various colour ratios and radiance enhancements applied to the CSDB mid-latitude liquid cloud spectra

Mid-latitude cirrus clouds

Technical Note:

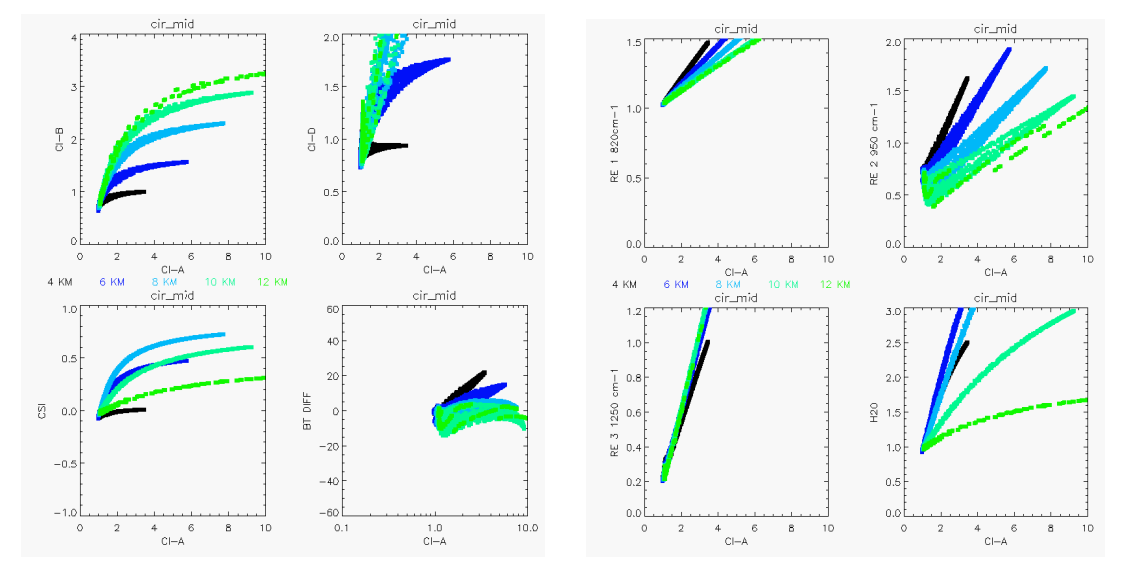


Figure 22: Various colour ratios and radiance enhancements applied to the CSDB mid-latitude cirrus spectra

Tropical cirrus clouds

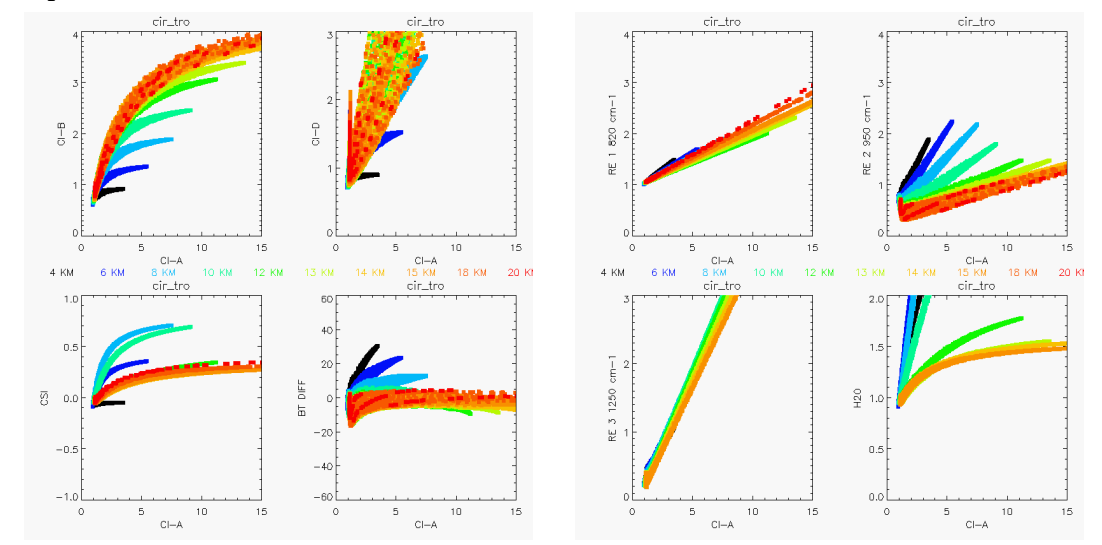


Figure 23: Various colour ratios and radiance enhancements applied to the CSDB tropical cirrus cloud spectra

Key findings:

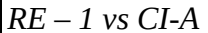
- 1. For liquid clouds, the shapes for each colour ratio and radiance enhancement is similar to the cirrus but with more scattered points over the ratios and the corresponding CI-A values. Some regions, such as RE-3 (fig. 21) still show a compact relation even for the liquid clouds case.
- 2. CI-B against CI-A tends to follow a curve that ranges from CI-B = 0.5 to 3.2 with the largest CI-B changes occurring at higher altitudes (fig. 22)
- 3. The CSI (fig. 23) shows a similar shape against CI-A but lower CSI values are obtained at for higher altitude spectra (12 km)
- 4. BT-DIFF and RE-2 show a distinctive 'tick' shape at low BT-DIFF and low RE-2 close to CI-A = 1.2 (fig. 23).
- 5. For H₂O-dominated regions, the higher altitude spectra have a smaller gradient compared to lower altitude spectra (as expected), particularly for the H₂O (BT), RE-2 and BT-DIFF ratios (fig. 23).
- 6. Tropical cirrus clouds show similar patterns to the mid-latitude cirrus for the various colour ratios examined but some ratios such as CI-B and CI-D appear to be more scattered.

Things to investigate:

- How do these relationships change when the clouds are restricted to the MIPAS field of view?
- Do width or shift variations in the chosen microwindow regions alter the relationship between CI-A and other ratios or enhancements?
- What is the dependence of these colour ratios and radiance enhancements on latitude?

Radius enhancements and their relation to particle radius: Tropical cirrus

In the following figures, radiance enhancements (RE) are shown plotted against the strongest colour ratio (CI-A) with respect to particle radius and ice water content. The RE have been selected because enhancements in these regions are likely to be connected to certain spectral features belonging to particular types of clouds. In which case, these investigations are performed to see if the RE or CI-A captures some of this behaviour with respect to cloud microphysical properties.



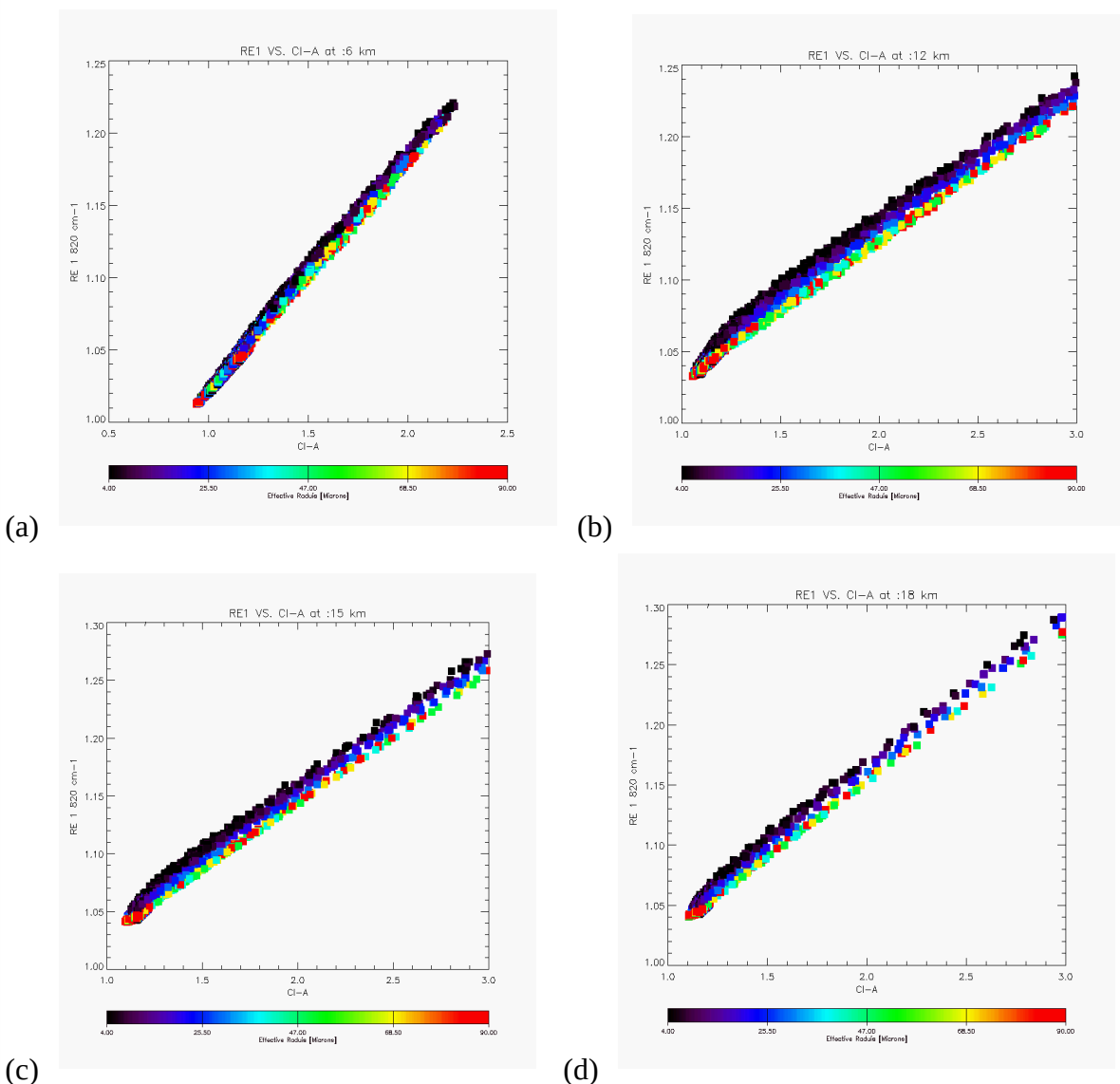


Figure 24: CI-A against RE-1 for (a) 6 km, (b) 12 km, (c) 15 km and (d) 18 km colour coded with particle radius

(c) (d) Figure 25: CI-A against RE-2 for (a) 6 km, (b) 12 km, (c) 15 km and (d) 18 km colour coded with particle radius.



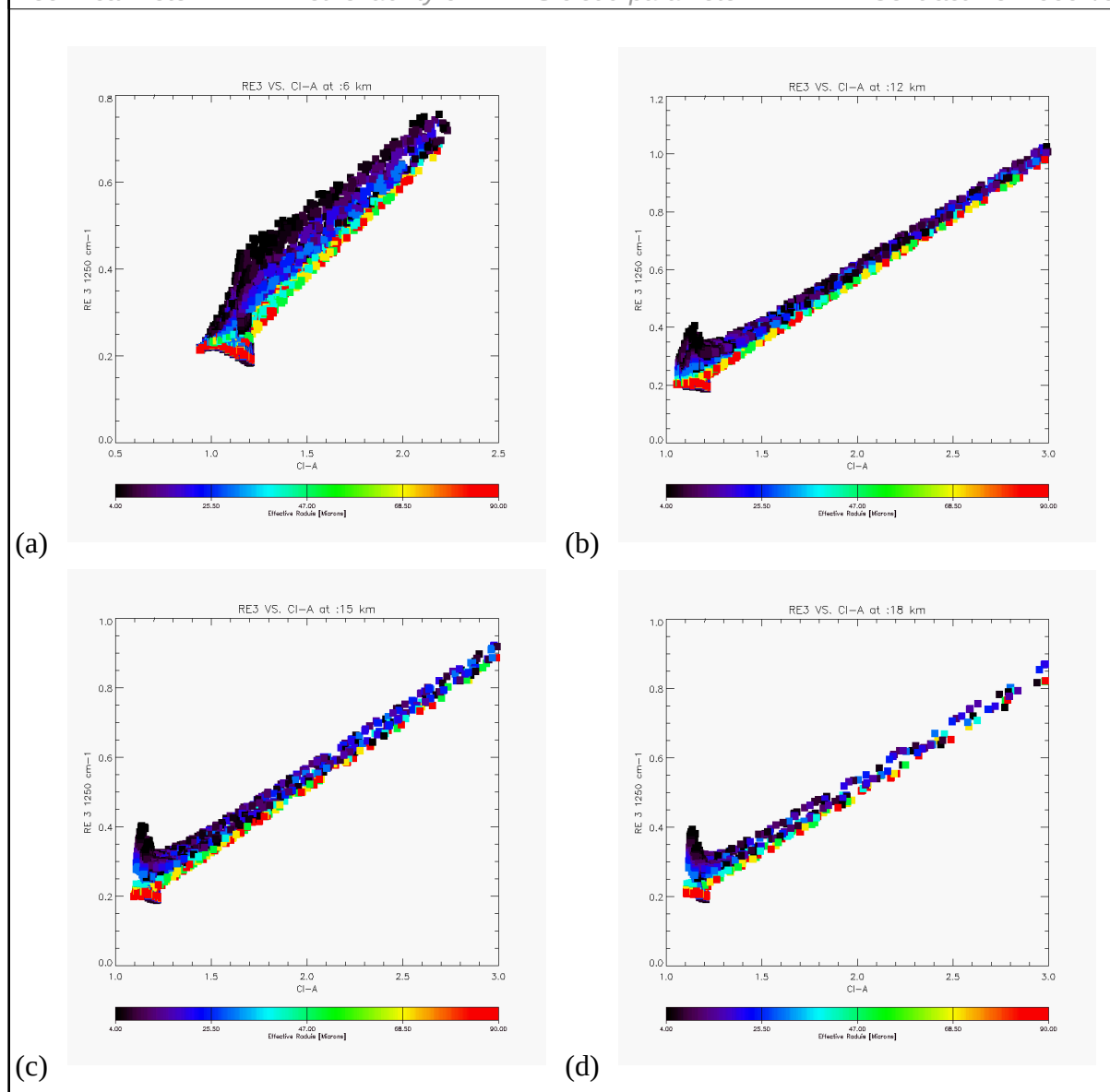


Figure 26: CI-A against RE-3 for (a) 6 km, (b) 12 km, (c) 15 km and (d) 18 km colour coded with particle radius.

Key findings:

- RE-1 shows a compact relation with CI-A for all altitudes (figs 24(a) to 24(d)) and its dependence of particle radius is such that for each CI-A in the range, a lower RE-1 are found for larger radii, however, the RE-1 range is small (no more than 0.3 nW/cm² sr cm⁻¹ in all cases.)
- RE-2 against CI-A shows a different behaviour at different altitudes: at 6 km (fig. 25(a)), a sharp saturation point is evident at CI-A = 1.2 but with little variation in RE-2 (~0.6). This point it dominated by larger particles (~ 90 microns) that are also distributed over higher CI-A values.
- At the altitudes of 12 km, 15 k and 18 km (figs. 25(b) to 25(d)), there is a large scatter of RE-2 between values of 0.3 and 0.7 over a CI-A range of 1 to 3.
- A more distinct particle radius dependence at these altitudes is clearly observed: for points in the regime of CI-A > 1.2 and RE-2 < 0.5, particle radius of 4 to 30 microns is more sensitive and for the regime of CI-A > 1.2 and RE-2 > 0.5, particles radius of 30 to 90 microns becomes more important.
- For increasing CI-A between 1 and 3, RE-3 also increases but over a small range of 0.2 to 0.8 nW/cm² sr cm⁻¹. At CI-A < 1.2 (saturation point), the data seems to show an 'arrow'

shape with particles of radius close to 90 microns corresponding to RE-3 = 0.2 nW/cm² sr cm⁻¹.

Things to investigate:

- . The dependence of ice water content on these radiance enhancement regions
- . How do these relationships change when MIPAS field of view restrictions are applied?
- . Are there any particular cases in which the RE values significantly deviate from what is seen above?

Conclusions and further work

A literature survey carried out has helped to identify and collate infrared spectral information related to detection and classification of cirrus cloud parameters. The results of this survey have been applied to the CSDB for mass analysis of mid-latitude and tropical cirrus cloud spectra. The main objectives of analysis of this kind are two-fold: first, what can we *detect* with the chosen spectral regions? In what situations do the relationships for each CI and RE change? and secondly, can we *classify* the type of clouds observed in the spectra by relating the CI and RE's to microphysical cloud parameters?

More specific work is now in progress that is based on more intensive analysis of the 950 cm⁻¹ region for improved cloud detection and definition of better thresholds for operational band D. Using the methodologies and results presented in sections 4.1 and 4.2, work will continue on classification of cirrus/liquids with cloud top height restrictions. Results from these areas will contribute to defining suitable microwindows for the operational processor.

3.2.2 Hight Dependent Cloud Index Thresholds

The assumption of an constant threshold value with altitude is a limitation for the sensitivity in cloud detection. Like the example in Figure 27 illustrates, it is quite obvious that 'clear sky' colour ratio profiles have a characteristic altitude dependence (illustrated by a dashed grey line). The CI profiles for NH and SH polar winter conditions show a strong variability. The dark grey curves are highlighting profiles which are marked as 'cloudy' by a CI-threshold value of CI<4. The extended threshold is restricted to 14 to 30 km. The shaded box areas indicates the cloudy area in the CI-height space for the MIPAS operational processor (light grey CI=1.8).

The rough pre-selection of cloudy profiles with the extended threshold allows to compute a mean CI-profile for none-PSC profile, here for log(CI) (dashed line). A log(CI) +/- 2 x standard deviation of log(CI) is superimposed for the profiles not marked as PSCs (thick grey) to illustrate a potentially better hight dependent threshold. The mean profile looks quite stable over the season. Therefore it is a reasonable approach to transfer such a kind of analysis to various latitude bands and seasons to define a background CI and consequently a CI-threshold climatology. For altitudes around and below the tropopause the pre-selection demands some refinements for proper handle of cirrus clouds.

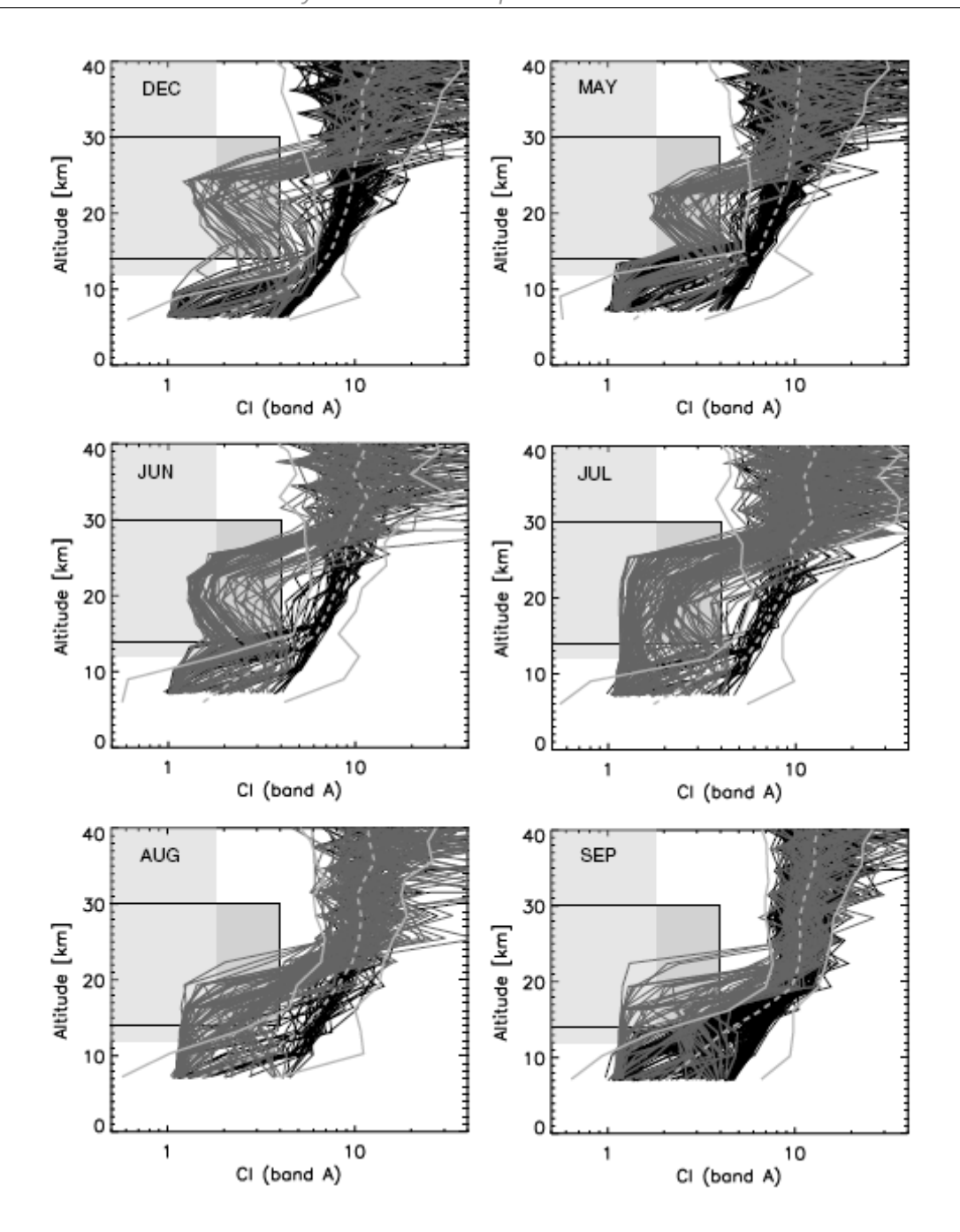


Figure 27: Cloud index profiles for the MIPAS for December 2002 in the northern hemisphere and May to September 2004 in the southern hemisphere. Only subsets are shown (1-3 days of observations) of profiles for the specific months north and south of 60° and –60° latitude, respectively (adopted from *Spang et al.*, 2005).

3.2.3 A climatology of CI-threshold values

In a first step a climatology for 2003 of the probability densities for the standard MIPAS Band A cloud index has been created with aim to setup a more objective cloud index threshold, depending on altitude, latitude and season. An example for March 2003 is shown in Figure 28. Obviously an altitude dependent threshold makes more sense then the current constant one. Different latitudes and seasons looking quite similar in the PDF distribution, however polar winter conditions with high occurrence frequencies of PSCs show a quite different behaviour. The example in Figure 29 represents a larger noise in CI at high non-cloudy levels (>30 km) and due to the high cloud occurrence no local minimum in the distribution width around the tropopause is existing, which is typical for nearly all other latitude bands and months.

Obviously a simple median or mean profile would not represent the a best estimate of CI-threshold profile. Therefore we optimised the procedure by applying different criteria above, at, and below the altitude, where the PDF starts to become a bi-modal distribution (in the two examples at around 19 and 25 km respectively, the altitudes where the cloud occurrence starts). For example, the precentile 0.1 was chosen for a lower background value with small negative offset in log10(CI) to go bellow all potentially non-cloudy values with the CI-threshold.

Finally the analysis ended up with a climatology of threshold profile, which allow a much more sensitive cloud detection, especially at higher altitude like around the tropopause. An example for the latitudinal and temporal evolution of the CI threshold profiles is shown in Figure 30. The results are very promising, showing a smooth transition from the equator to poles as well as realistic and smooth variation over the year for a fixed latitude band. All threshold profiles have been checked by eye in comparison to the PDFs to sort out spurious events in the used radiance profiles, which can cause significant outliers in the profiles.

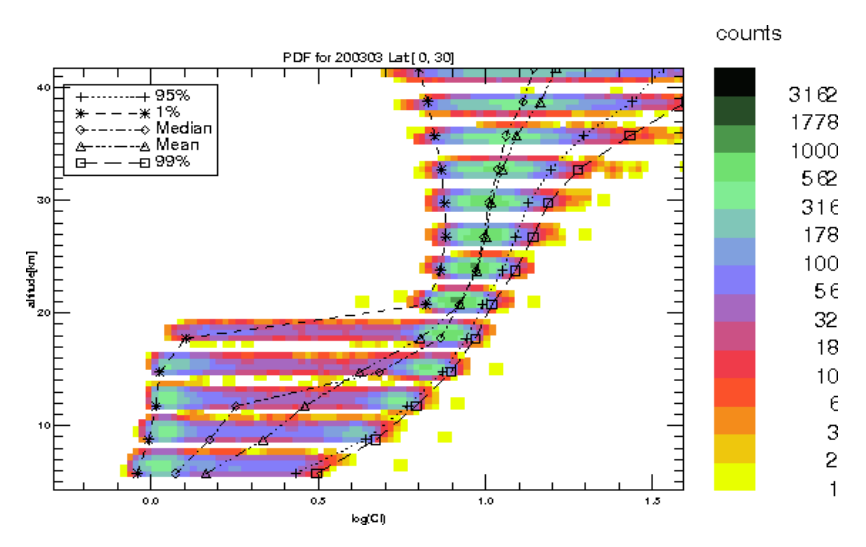


Figure 28: Example for MIPAS band A cloud index color ratio PDF with altitude. Here for March 2003 at 0-30°N. Superimposed are various precentiles and mean for log₁₀(CI).

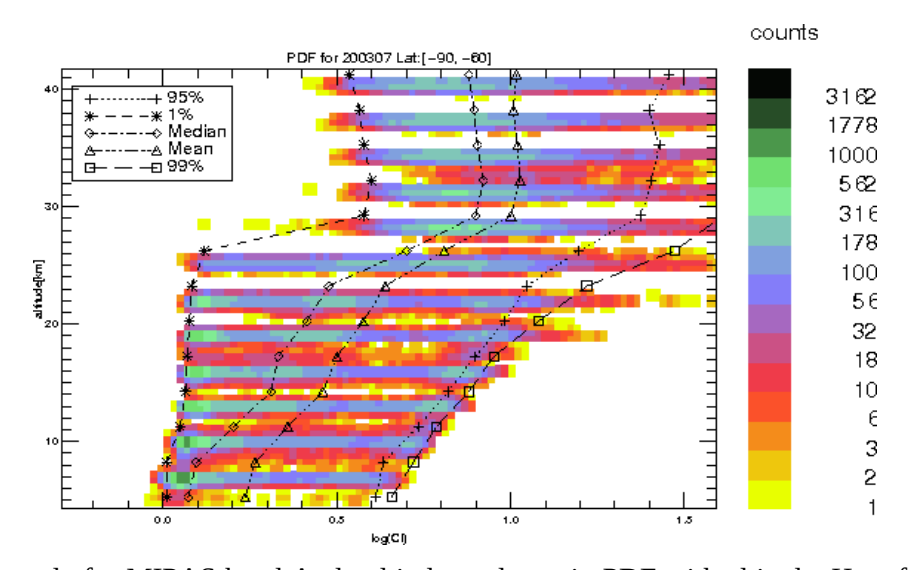
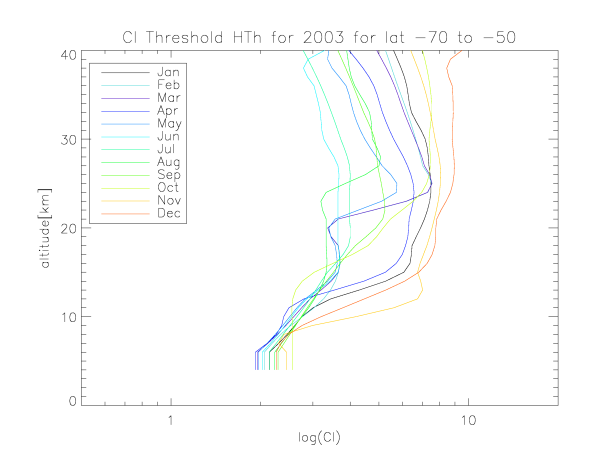


Figure 29: Example for MIPAS band A cloud index color ratio PDF with altitude. Here for July 2003 at 60°S-90°S. Superimposed are various precentiles and mean for log₁₀(CI).



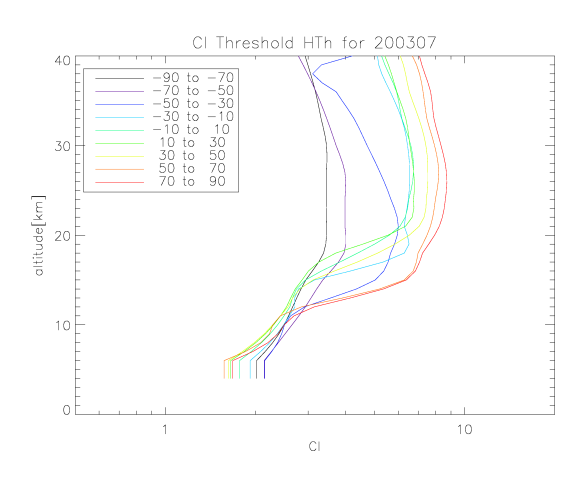


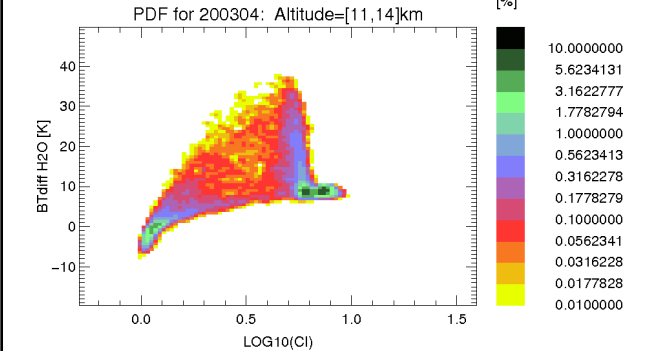
Figure 30: (a) Seasonal development of the retireved CH-threshold profile for a latitude band -90 to -70 deg. (b) Zonal variation of CI-threshold profiles for August 2003.

3.2.4 Analysis of MIPAS cirrus spectra in respect to water vapour

From various analyses of MIPAS spectra in comparison to modelled forward calculations it is obvious that high water vapour mixing rations in the free troposphere falsify the operational cloud flagging in the MIPAS processing, by overestimation the occurrence of clouds (e.g. S2003). This is especially a problem well below the tropopause (3-6km), where water vapour mixing ratios between 1000 and 10000 ppmv reduces significantly the cloud index colour ratio. A second colour ratio or a brightness temperature (BT) difference sensitive to water vapour can significantly improve the cloud detection method - like analyses of the airborne CRSITA-NF instrument already showed (Spang et a. 2007). We applied the method to MIPAS for the year 2003 for various months and latitude bands. Examples are given in Figure 31 by the probability densities in the two parameter space, standard cloud index CI_A versus BT difference for water vapour. The results show very compact correlations for cloud with no water vapour influence (basically only in CI with constant low BTdiff) and non-cloudy conditions with water vapour enhancement (basically only in BTdiff).

A separation in different regimes of the scatter plot is suggested in Figure 32 where model calculations for a slightly different and simplified setup for the airborne CRISTA-NF measurements are presented. In the model runs water vapour was varied for constant background extinction profile and extinction vice versa for five reference background atmospheres. The results show a qualitatively correspondence with Figure 26, with a clustering in different regimes of the scatter plot with regions for high water vapour and regions by enhanced cloud extincton.

A corresponding analysis using the CSDB for cirrus clouds will afford to define an improved cloud indicator for a more unambiguous classification of cloud spectra and non-cloudy spectra with high water vapour content. However, Figure 32 also shows that there are transition regions where a definite differentiation will be difficult, areas where a mixture of enhanced extinction by clouds and high water vapour content prevails. Further investigations on characteristic cloud signatures by cirrus and liquid clouds in the spectra might help to solve this problem.



[%]

log10(CI)

BTdiff H20 [K]

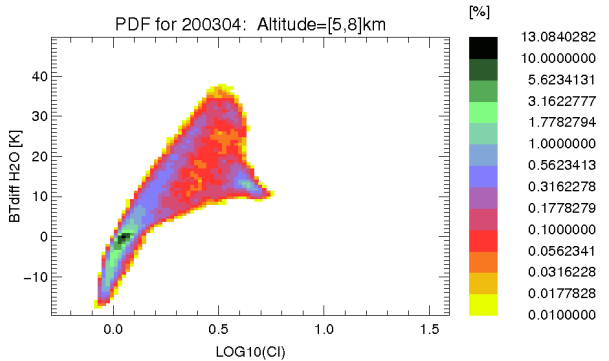


Figure 31: Example of probability densities (PDF) for cloud-index MIPAS band A versus Brightness Temperature difference sensitive to water vapour (784.0-784.8 cm⁻¹ and 787-788 cm⁻¹ mean radiance) for April 2003. **Top left**: PDF contour plot of the total number. All other plots are given in percentages of the total number of observations. Top **right:** High altitudes with only tropical cirrus clouds (log CI < 0.5) and mainly cloud-free conditions (log CI~1) Bottom left: Spread from cloud-free to enhanced water vapour (large BTdiff) and large amount of optically thick conditions (log CI and/or negative BTdiff) for tangent heights around 12 km. Bottom right: low attitude observations with steepening in correlation distribution.

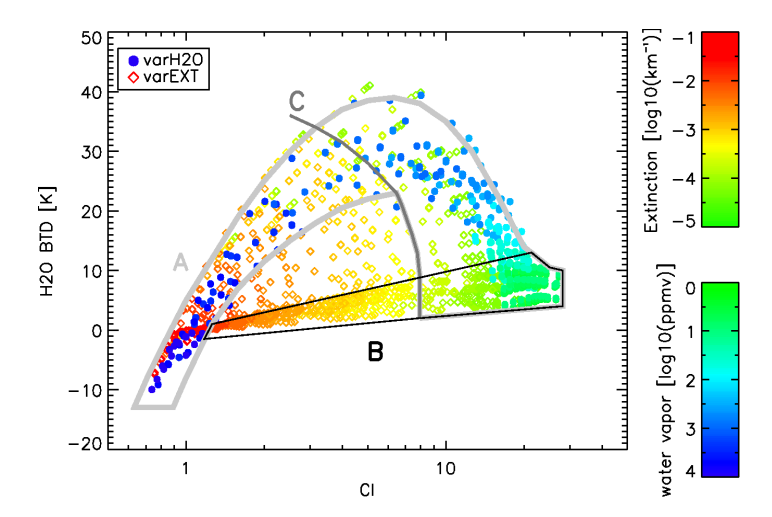


Figure 32: Model calculations for various background atmospheres without scattering for aircraft geometry of the CRISTA-NF cloud index colour ratio (MW1: 791- 793 cm-1; MW2: 832-834 cm-1) versus a brightness temperature differences which is sensitive to water vapour (MW1': 784-785 cm-1 minus MW2': 787-788 cm-1). Top colour bar are related to open symbols of varied extinctions and lower colour bar to filled dots with varied water vapour in the radiative transfer calculations. Superimposed lines indicate regions where enhanced water vapour with potentially enhanced extinction (A) and enhanced extinctions with low water vapour (B) are dominating. The curve C separates on the right hand side enhanced water with low extinctions with the transition region of enhanced extinction and/or enhanced water vapour on the left hand side (Spang et al., 2007).

3.2.5 Quantification of the CI restrictions due to high tropospheric water vapour

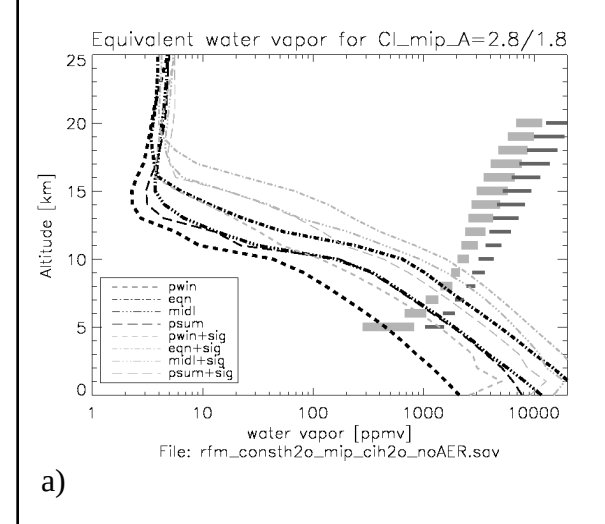
The simple CI color ratio (CR) is quite sensitive to tropospheric water vapour like already pointed out for the CRISTA-NF measurements (see above). Figure 33 illustrates the problems with water high vapour continuum at lower altitudes. RFM runs using the five reference atmosphere with varied H2O at the tangent height in the range 0.5 to 50,000 ppmv have been performed and analysed in respect to the threshold where which amount of H2O is producing a CI-CR a corresponding CR-value (here 1.8 and 2.8 in Figure (a)).

Obviously high water vapour makes the detection of clouds with CI-CR ambiguous for values above 1000-3000 ppmv for most altitudes. But it is more the question at which altitudes one can expect such high values. Based on the reference atmospheres from Remedios et al. (ACPD, 2008), which were used in the model calculations, the profiles have been added with climatological standard deviation (1 sigma). From this it becomes clear, that for the tropics below 9 km, midlatitudes at 8 km, and polar regions between 7 and 5 km, cloud detection becomes difficult.

A potential solution to that problem was suggested by Spang et al. (2007) and is already introduced above. The brightness temperature difference (BTD) of a water vapour at 784 cm-1, only prominent in the free troposphere (> 10 ppmv), and the radiances close to the line at 787 cm-1 gives a reasonable proxy for high water vapour values. Figure (b) shows the good correlation for BTD[784-787] with water vapour for each background atmosphere. But for extreme high values (>1000 ppmv) BTD is shrinking, which makes the differentiation between high water vapour continuum and clouds difficult again (only for altitudes > 6 km below the tropopause). However, the analysis of each MIPAS BTD profile would allow to analyse if high BTD are already detectable above the TH of interest. If this is the case, small CI-CR values at the TH of interest are most likely caused by the water vapour.

Improvements achieved:

A color ratio for cloud detection in a wavelength region less sensitive to water vapour could help to bypass the water vapour continuum problem. However, the BTD approach is getting problematic for $\rm H2O > 1000$ ppmv. Potentially, new CI-CR less sensitive to $\rm H2O$ would allow a better differentiation between enhanced water vapour continuum and clouds.



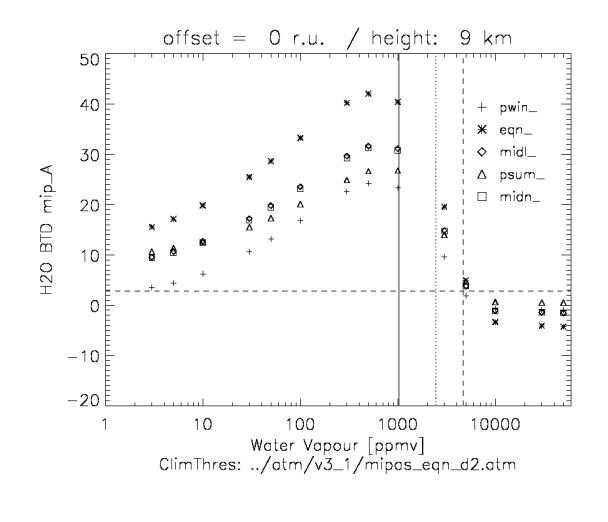


Figure 33: (a) Equivalent range water vapour necessary to produce CI=1.8 (thick horizontal gray bars) and CI=2.8 (thin) for 5 reference atmospheres. Overlaid by the H2O profiles and profile plus standard deviation. (b) Modeled BTD values for 5 climatological profiles with enhanced H2O at the tangent height layer (x-value). Vertical lines indicate H2O at 9 km for equator, equator plus climatological standard deviation, and maximum value of the reference atmosphere (Remedios et al., ACPD, 2008). Details see text.

b)

3.3 Optimised MircoWindows / Cloud Effective Fraction (CEF) approach

3.3.1 Introduction

The current operational cloud detection consists of taking the ratio of average radiances in a pair of microwindows (788.2-796.25)/(832.3-834.4) and testing this ratio against some threshold value (1.8). If the ratio is smaller than this threshold then the spectrum is assumed to be cloud-contaminated. The actual microwindows used, and the threshold value, have been chosen subjectively, although based on experience with the CRISTA experiment.

The aim of this section is to investigate whether a better pair of microwindows, and/or a better threshold value, can be found using objective criteria based on simulated spectra with known cloud amounts.

3.3.2 Spectral database

The database used for this part of the study consists of RFM-simulated A-band spectra (0.025cm⁻¹ resolution) for all combinations of

Tangent Height: 6, 9, 12, 15, 18, 21 km

Cloud-Top Height: -2,-1.5,-1,-0.5,0,0.5,1.0,1.5,2.0 km

Cloud extinction: 0.1, 0.01, 0.001 /km

The cloud is modelled as a simple grey absorber and the CTH is defined relative to the centre of the FOV. The spectra with crH=-2km represent the 'cloud-free' case. For an individual atmosphere this generates spectra. Sets of 162 spectra were generated for 4 reference atmospheres corresponding to mid-lat night, equatorial day, polar winter (night) and polar summer (day) conditions, plus the 4 atmospheres perturbed by 1-sigma climatological variations (Remedios, 2001). Thus a total of 1296 spectra are used in this analysis.

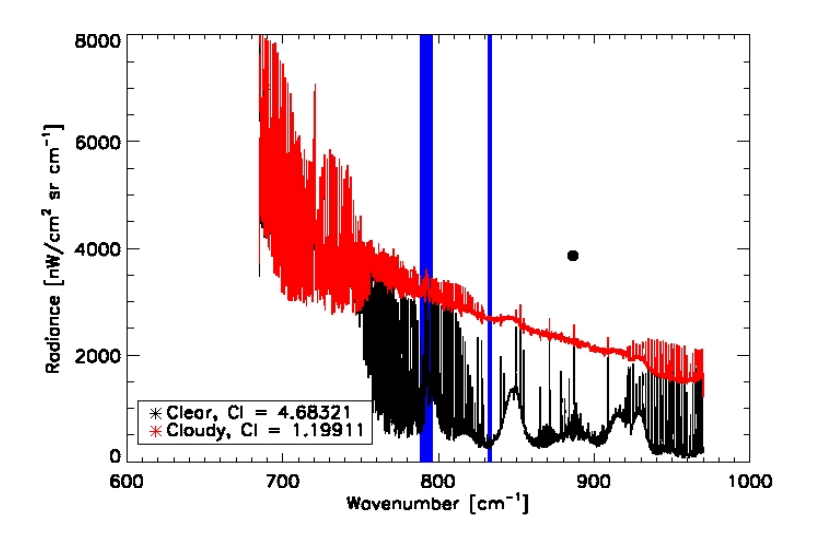


Figure 34: Samples of clear (black) and cloudy (red) MIPAS spectra at 9km with the locations of the current CI MWs overplotted (blue).

3.3.3 Cloud Effective Fraction (CEF)

The phrase 'cloud detection' implies a simple yes/no decision is required based on some sort of threshold test, but the question is more complicated than that. For example, how do we compare a small amount of thick cloud within the field of view with a larger amount of thin cloud? To resolve this, we introduce the concept of "Cloud Effective Fraction" defined formally as

$$CEF = \int_{FOV} \left(1 - e^{-k * x(z)} \right) * \Psi(z) dz$$

where k is the cloud extinction (/km), x is the integrated distance along a pencil beam within the cloud, is the normalised field-of-view response function, z is the tangent height.

The advantage of defining the CEF is that all types of cloud contamination of a field-of-view (including non-uniform cloud) can be represented by a single parameter which has a physically meaningful interpretation.

Thus the question of 'cloud detection' can be reduced to a particular threshold value of the CEF.

3.3.4 CI versus CEF

The CI value for a particular pair of microwindows can be plotted against the CEF value calculated for each of the 1296 simulated spectra and CI plotted against CEF.

An ideal pair of microwindows chosen for cloud-detection would provide a robust relationship between CI v CEF for a variety of different conditions (atmospheres, cloud-types, tangent heights).

Unfortunately the form of this relationship is not predictable. However, plotting the $\log^{(CI)}$ v $\log^{(CEF)}$ for the current pair of CI microwindows shows a reasonably linear relationship and this is the form that will be assumed.

$$\ln\left(CEF\right) = a * \ln\left(CI\right) + b$$

where a,b are parameters chosen to minimise

$$\chi^2 \!=\! \sum \left[\left(\ln \left(C\!E\!F \right) \!-\! a\!*\! \ln \left(C\!I \right) \!-\! b \right)^2 \!+\! a\!*\! \sigma^2 \right]$$

where i is the expected variance in $\frac{\ln(CI)}{\ln(CI)}$ due to instrument noise (i.e. narrow microwindows are 'noisier'). The 'best' pair of microwindows are those for which i, or the root mean square deviation between the actual CEF and predicted CEF, is a minimum.

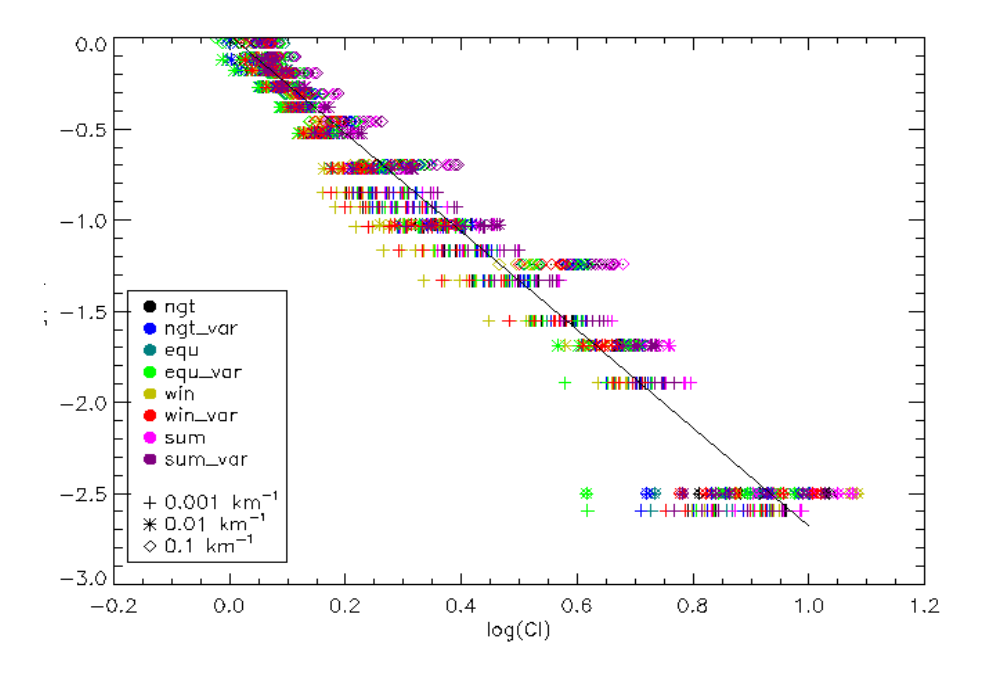


Figure 35: Shows approximately linear relationship of current CI MWs, for all tangent heights and relative CTHs, with color-coding for different atmospheres used and different symbols for different K_{ext} s.

3.3.5 Iterative optimisation of CI microwindows

A pair of CI microwindows are defined by 4 parameters corresponding to the upper and lower boundaries of each microwindow. In the MIPAS A-band, even restricting to the region 750-970cm⁻¹ where the atmosphere is reasonably transparent, there are several thousand spectral points making a systematic search through the entire parameter space unfeasible.

The approach adopted by Desmond (2007) was to search through microwindows with integer wavenumber boundaries and then, for each 'coarse' microwindows, iterate moving each boundary one grid point at a time. Using this technique he identified a better pair of CI microwindows

	Lower MW	Upper MW	RMSE
Operational MWs	788.200- 796.250	832.300 - 834.400	0.181
Optimised MWs	774.075 - 775.000	819.175-819.950	0.157

However, he also noted that the iteration on the 'coarse' microwindow boundaries never proceded beyond a few steps (note the optimised MW boundaries in the table above remain close to the integer wavenumber intervals used for starting points), suggesting that the + parameter space is not smooth enough for such an approach to guarantee that the actual minimum has been found.

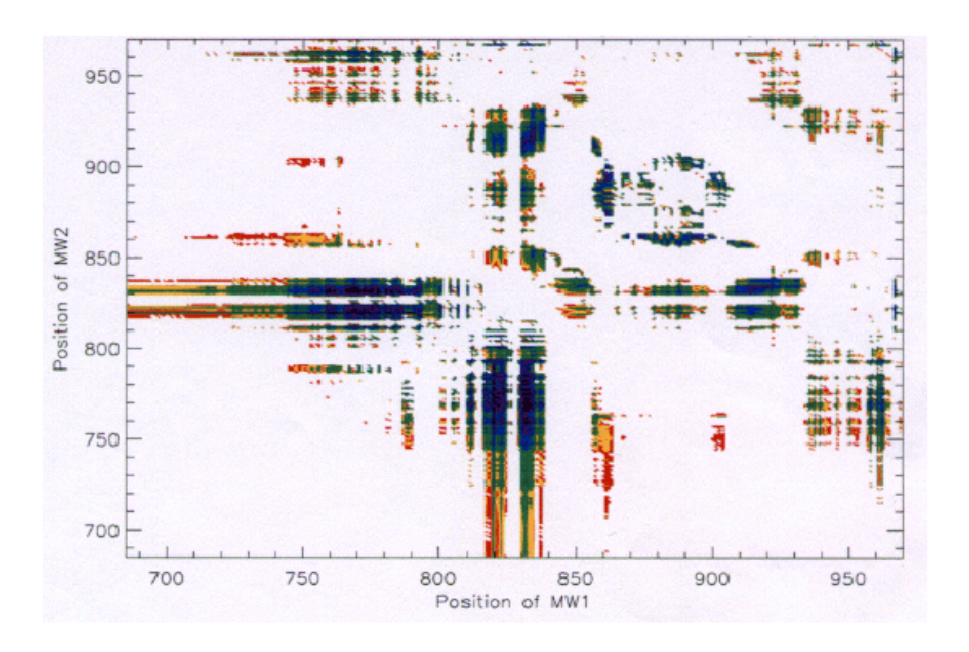


Figure 36: Plot showing the RMSE for the linear fit of $\log(CEF)$ as a function of $\log(CI)$ for CI calculated from MWs one wavenumber wide located throughout the A band. Darker colours represent lower RMSE. From Desmond (2007).

3.3.6 Monte-Carlo approach to CI optimisation

Following on from Desmond's recommendation, a slightly different approach to the optimisation is being investigated. This consists of using randomly-selecting microwindows from the domain (specified by mid-point and width) - not just integer wavenumbers - and using these as starting points for the iterative adjustment of the wavenumber boundaries.

In such a run, 10000 different microwindow pairs randomly selected from the entire 750–970 cm⁻¹ are used as starting points. By making a contour plot of the resulting RMSE values on axes represented by the midpoints of MW1 and MW2 (Figure 37), a particular region can be determined where these RMSE values approach a minimum. A further run will then be performed randomly selecting 10000 MW pairs just within this region, and the process repeated until the region is sufficiently small that successive runs return the same 'best' MW pair.

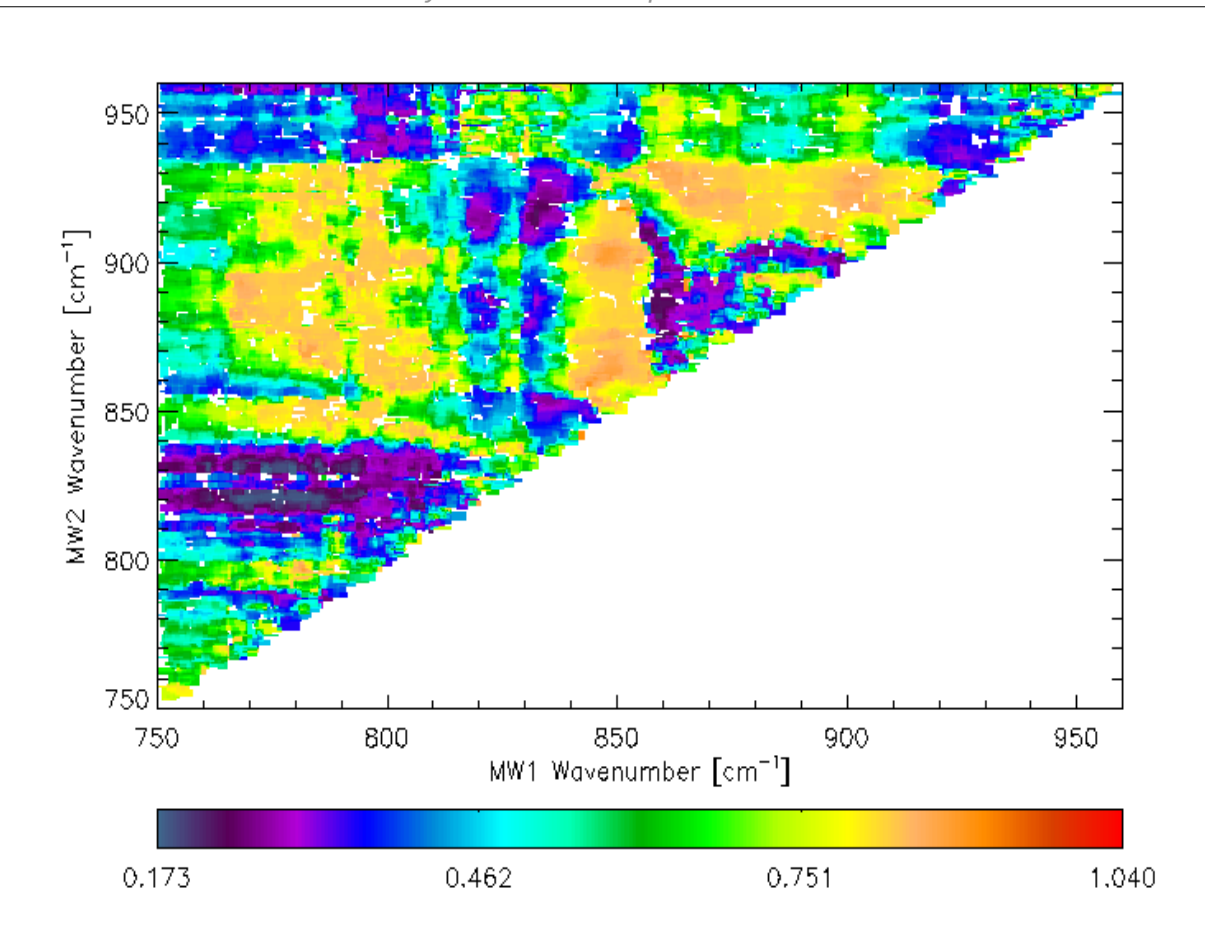


Figure 37:Plot showing average RMSE of CI microwindows selected randomly as being within a MW for 10000 random cases and then iterated towards minimum each time, whereby it has been specified that MW1 occurs spectrally before MW2. The next iteration narrowed the range to [760,795] and [815,835] cm⁻¹ - and third iteration of this test (currently running) has narrowed it further to [766,786] and [817,823] cm⁻¹.

3.4 Cloud detection using SVD

3.4.1 Introduction

Singular Value Decomposition is a well-known mathematical technique for detecting patterns in a large dataset. It relies on the fact that any $m \times n$ matrix A can be decomposed into

A = VDU

where V and U are $m \times m$ and $m \times n$ orthonormal matrices containing left- and right-singular vectors and D is an $m \times m$ diagonal matrix containing singular values. In this case, A represents a set of m spectra each of length n. Each row of U is a singular vector representing the spectral 'pattern' (of length n) within the dataset whose significance is represented by the magnitude of the corresponding singular value n.

The usefulness of this technique is that it can be used to reduce a potentially large amount of information (represented by the m X n elements of A) to its principle components, represented by the singular vectors and their associated singular values, where only a few (<< m) singular values

are significant.

3.4.2 Application to cloud detection

Given that the presence of cloud affects many different points within a MIPAS spectrum, it may be possible to use SVD to identify particular patterns within the spectra associated with cloud-contamination. This would have an advantage over conventional detection techniques in using all the information in the spectrum rather than particular microwindows.

The obvious approach might be to apply a SVD to an ensemble of spectra, real or simulated, and look for a particular pattern that can be associated with cloud contamination. However, this turns out not to be useful since the singular vectors that emerge, or particularly their associated singular values, do not bear any strong relationship with the degree of cloud-contamination as represented, for example, by cloud index or cloud effective fraction.

A more sophisticated approach is required in order to try and separate the cloudy components from the components representing normal atmospheric variability.

3.4.3 Clear sky singular vectors

The first step is to consider just an ensemble of simulated cloud-free spectra representing a variety of atmospheric conditions and tangent heights (simulated spectra are preferred to real spectra since they can be guaranteed to be cloud-free).

The simulations are given by combinations of 6 tangent heights * 16 different atmospheres represented by the 4 standard atmospheres, the 4 atmospheres plus 1-sigma climatological variability in every parameter, and then each of these varying just one of temperature, pressure, water vapour and ozone separately (these last 8 spectra are additional to those used in the CI optimisation).

Only simulations for the A-band were considered, and just taking the range 827.5-970.0cm⁻¹ (ignoring the opaque lower half of the A band which would not be expected to contribute any cloud information).

First, the average spectral radiance is subtracted (section 3.4.5) and an SVD analysis performed on the resulting spectral dataset (Figure 38). For the 9 km tangent height 90% of the total variation is captured using just the first three singular vectors (Figure 39).

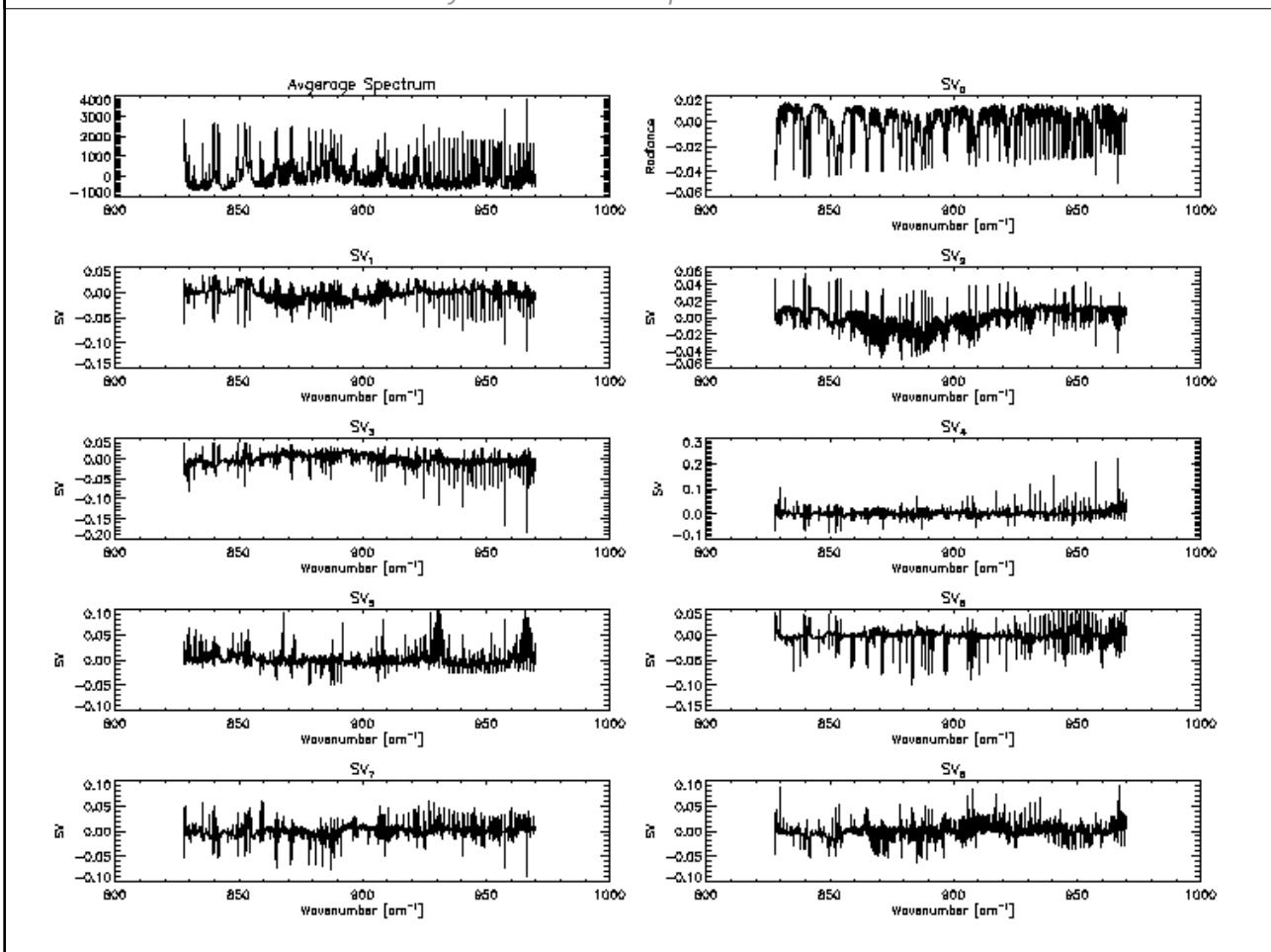


Figure 38: Average clear spectrum for the 9.0 km clear ensemble along with the first eight singular vectors.

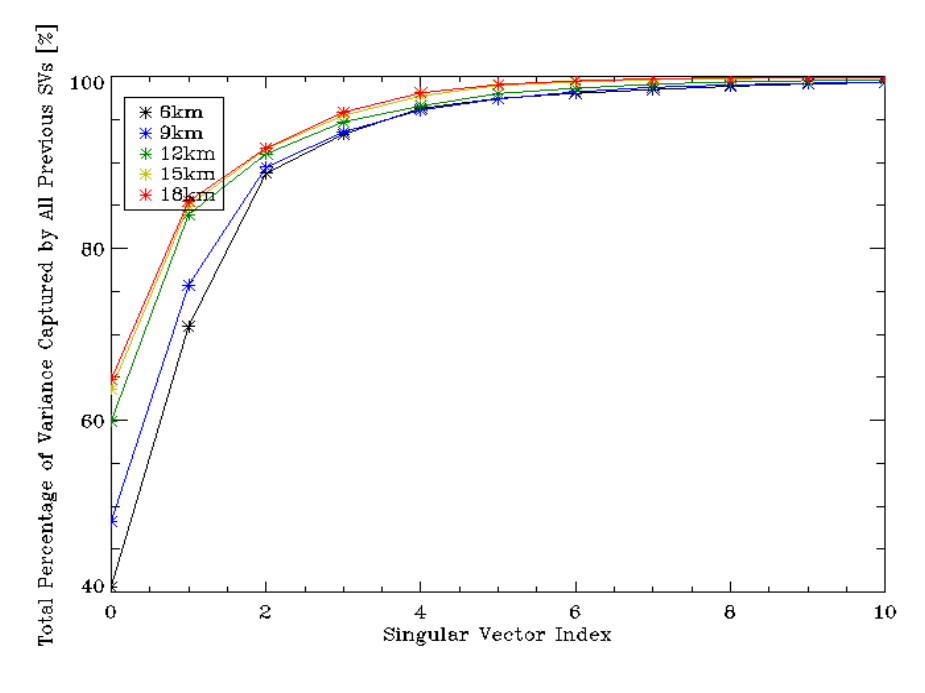


Figure 39: Percentage variance captured by each successive SV for various tangent heights clear decompositions.

3.4.4 Cloudy singular vectors

Now the various spectra with different levels of cloud-contamination are added to the analysis. As before, the first step is to subtract the mean radiance. Then the previously derived clear-sky singular vectors are fitted, and subtracted.

This leaves a set of 'cloudy residual spectra' which can then be decomposed into additional 'cloudy' singular vectors which will be orthogonal to the 'clear' singular vectors.

The net result of this two-stage approach is to derive a set of N+M orthogonal singular vectors, of which the first N represent the variability of molecular absorption features and the second M represent the variability of cloud continuum-like features (had a simple SVD analysis been performed on the full set of mixed cloudy and cloud free spectra there would be no such distinction between the cloudy and cloud free singular vectors that result).

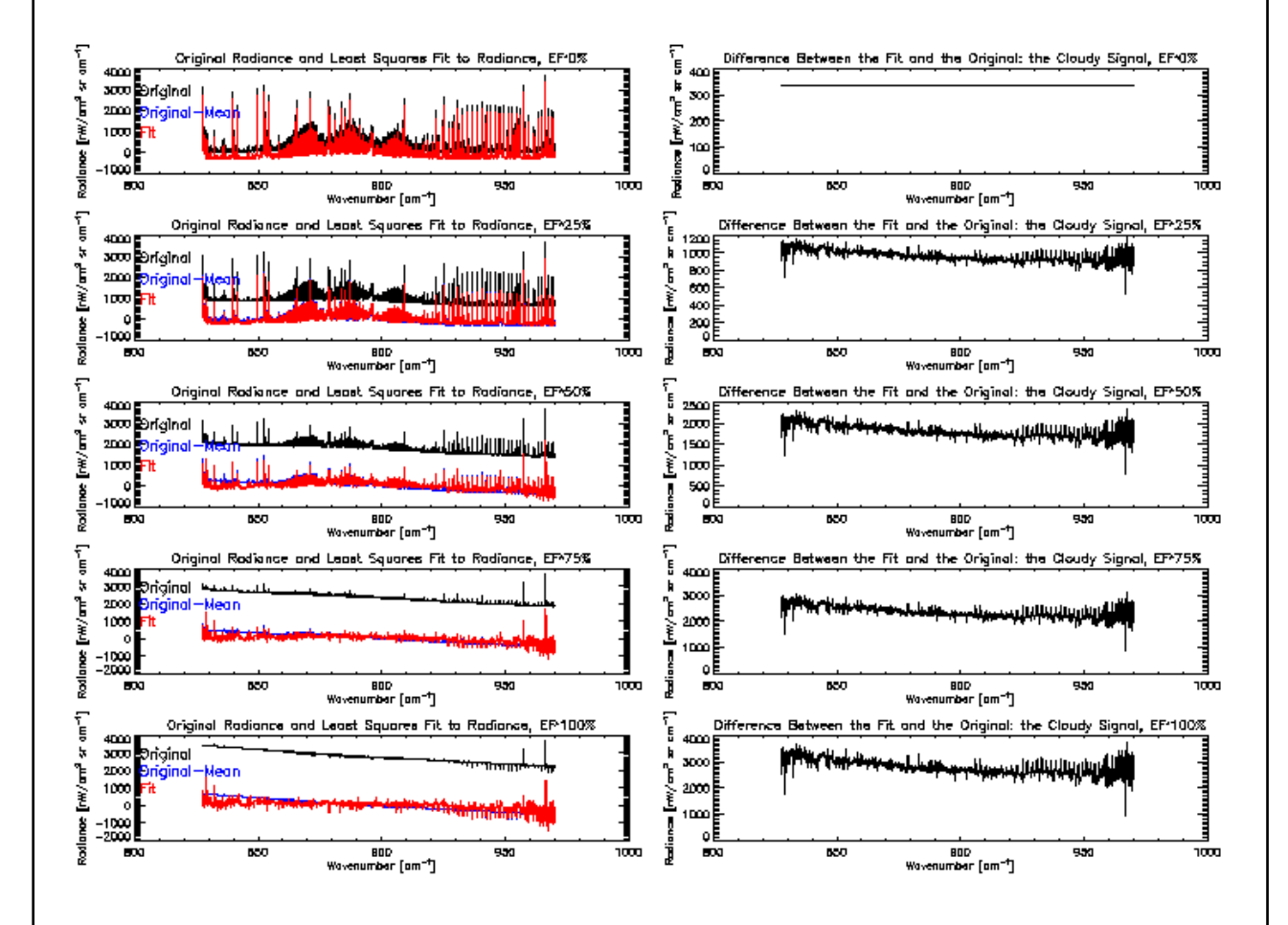


Figure 40: Fitting of cloudy signal by clear singular vectors to obtain cloud-only signal component for cloud in a 9 km tangent height FOV, using simulated data. From top to bottom of the plot, cloud effective fraction increases in equal increments of 25% from 0% to 100%. **Left panels:** the original signal containing varying amounts of cloud is shown in black, the spectrum with the mean subtracted in blue, and the clear singular vector least squares fit in red. **Right panels:** the component of the original signal attributed to the cloud (including mean radiance offset).

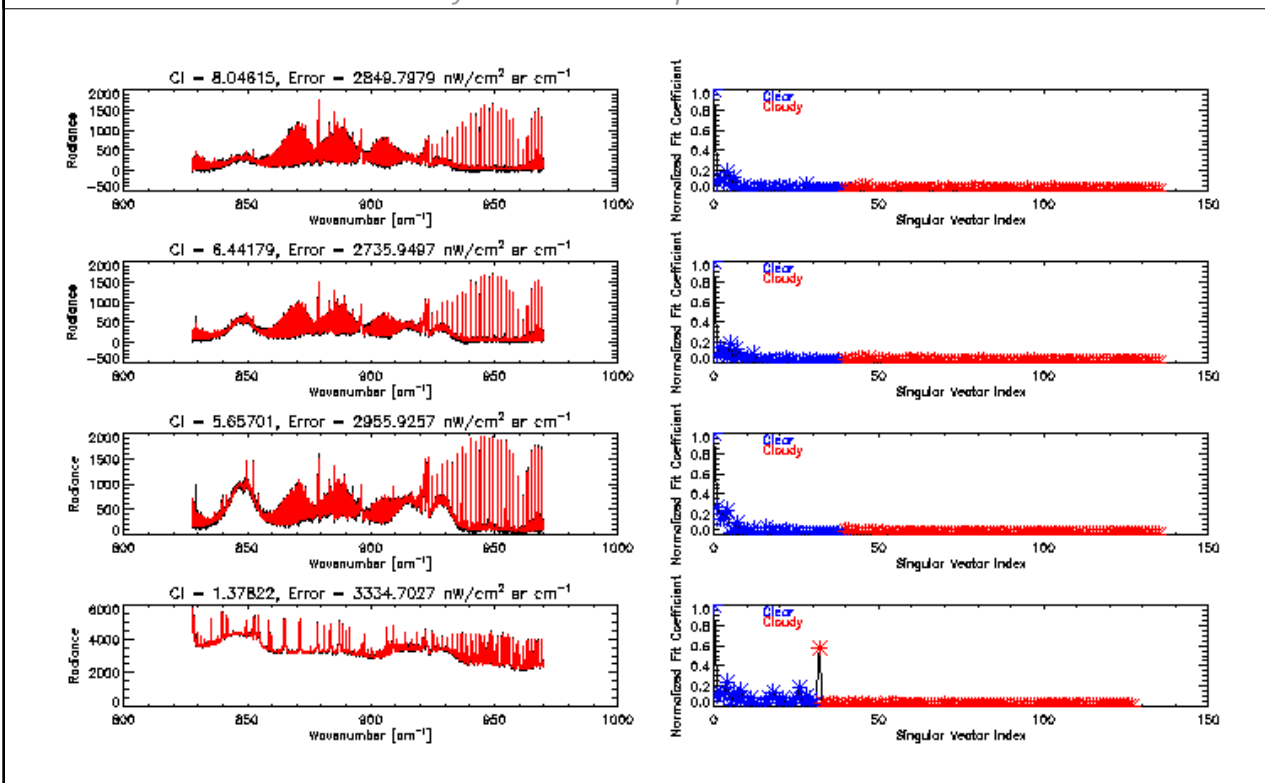


Figure 41: Fitting of actual MIPAS spectra by clear and cloudy singular vectors. From top to bottom, downwards through the scan pattern: 15.0 km, 12.0 km, 9.0 km and 6.0 km tangent heights. **Left panels:** linear least squares fit using both clear and cloudy singular vectors (red) overplotted on original input signal (black). **Right panels:** magnitudes of fit coefficients corresponding to the singular vectors used in the fit (clear in blue, cloudy in red), normalised such that the largest fit coefficient has a magnitude of unity. The lowest panel represents a cloud-contaminated spectra, indicated by the CI (1.38) and the peak in the amplitude of the first cloudy singular vector.

3.4.5 Subtraction of Mean Radiance

The assumption in the above analysis is that the cloud-contaminated spectra represent a linear combination of orthogonal clear-sky and cloudy contributions with the physical explanation that the presence of cloud reduces the magnitude of the molecular spectral features (and possibly inverts them) while increasing the magnitude of the continuum-like features.

However, if we attempt to fit just the clear sky singular vectors directly to cloudy spectra, we find that the clear sky vectors often have much larger singular values (and often of opposite sign), than for actual clear sky spectra. This is because the presence of cloud usually contributes an increase in the radiometric baseline in optically thin regions of the molecular absorption spectrum. Such increases cannot be represented by physically reasonable combinations of clear sky singular vectors.

An ad-hoc solution for this problem is to subtract the mean radiance of all spectra beforehand, which has the effect of removing the baseline offset and providing measurements which more closely fit our assumed behaviour.

(The mean radiance itself is a measure of the cloud contribution but tests show that it is highly correlated with the first cloudy singular vector so the actual value need not be incorporated into the cloud detection.)

3.4.6 Cloud Detection method 1 - 1 ratio test

Having established a technique for decomposing measured spectra into clear and cloudy singular vectors, two different cloud-detection tests have been investigated.

The first of these is based on a chi-squared test

$$\chi^2 = \sum_{i} \frac{\left(L_i^{meas} - L_i^{fit}\right)^2}{(n-m)\sigma^2}$$

where L_i^{mos} are the measured spectral points, L_i^{t} are the spectral points reconstructed from the fitted singular vectors, n is the total number of spectral points, m is the number of fitted singular vectors, and ℓ is the noise variance. If the spectra are well-characterised by the singular vectors the ℓ value should approach 1.

The i statistic is calculated using just the clear singular vectors, χ^2_{cloudy} , and using a combination of clear+cloudy singular vectors, χ^2_{cloudy} , and the ratio of the two is taken

$$R = \frac{\chi_{clear}^2}{\chi_{cloudy}^2} .$$

If this ratio approaches 1, then adding the cloudy singular vectors has little impact on improving the fit so the spectra are assumed to be cloud-free, whereas if the ratio is larger than one then adding the cloudy singular vectors has improved the fit so some cloud-contamination is assumed to be present.

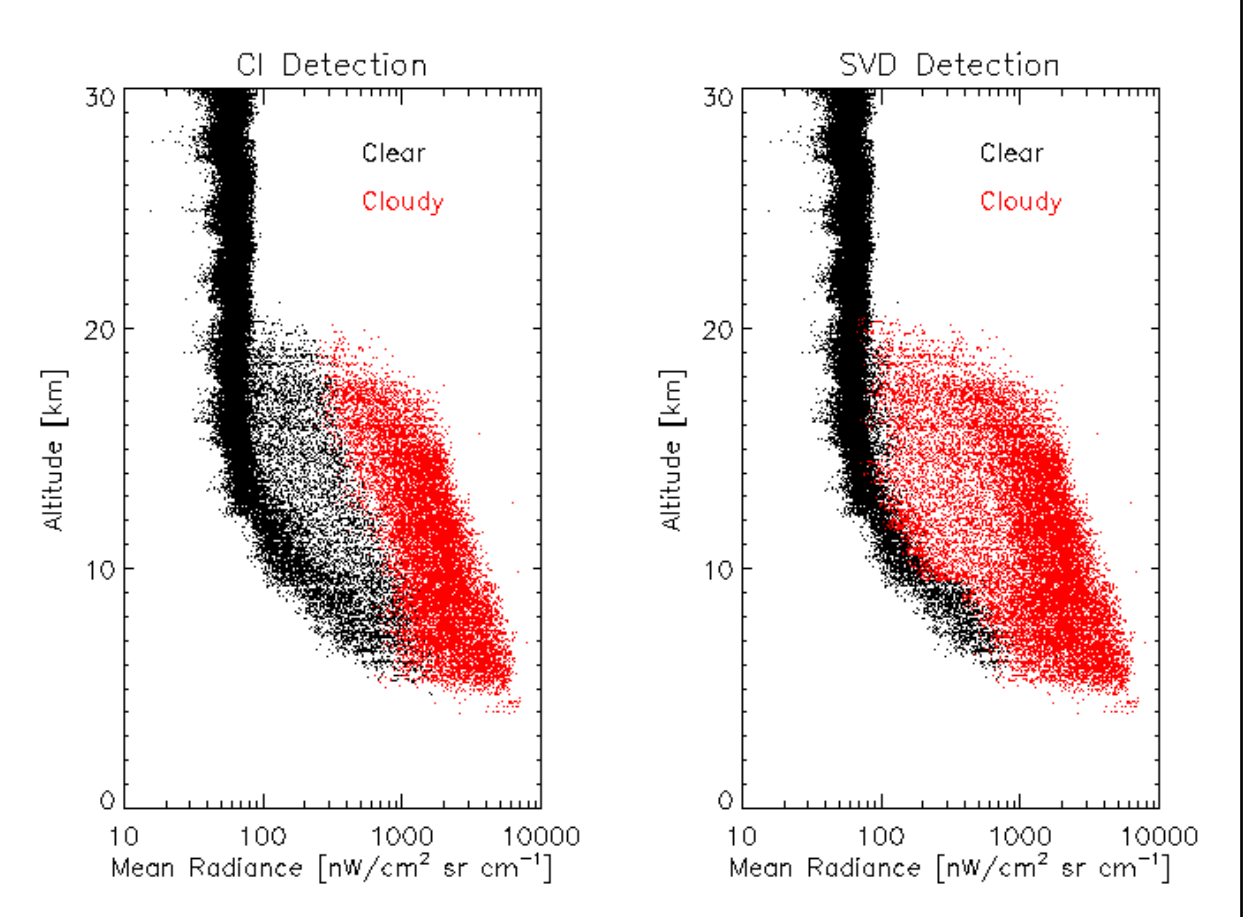


Figure 42: Profiles of average radiance in 960.0 - 961.0 cm⁻¹ atmospheric window from MIPAS spectra for 2003. **Left panel** indicates in red those cases flagged as cloud by the CI Method. **Right panel** indicates in red those cases flagged as cloud by SVD // Ratio Method. The SVD method appears to show a clearer distinction between two types of radiance, although this is not necessarily evidence that this is the better method.

3.4.7 Cloud Detection method 2 - Integrated Radiance Ratio

A second method of determining the degree of cloud-contamination is to use the clear and cloudy singular vectors to reconstruct an integrated radiance signal.

$$I = \frac{1}{n} \sum_{i} L_{i}^{fit}$$

where I is the integrated radiance and ¹/₁ are the fitted singular vectors summed over n spectral points (representing, for example, the spectral window 960-961cm⁻¹). Again taken the ratio of I calculated with just the clear singular vectors to that calculated using clear+cloudy singular vectors

$$R = \frac{I_{clear}}{I_{cloudy}}$$

This ratio is expected to vary between 1 and 0 with increasing cloud contamination.

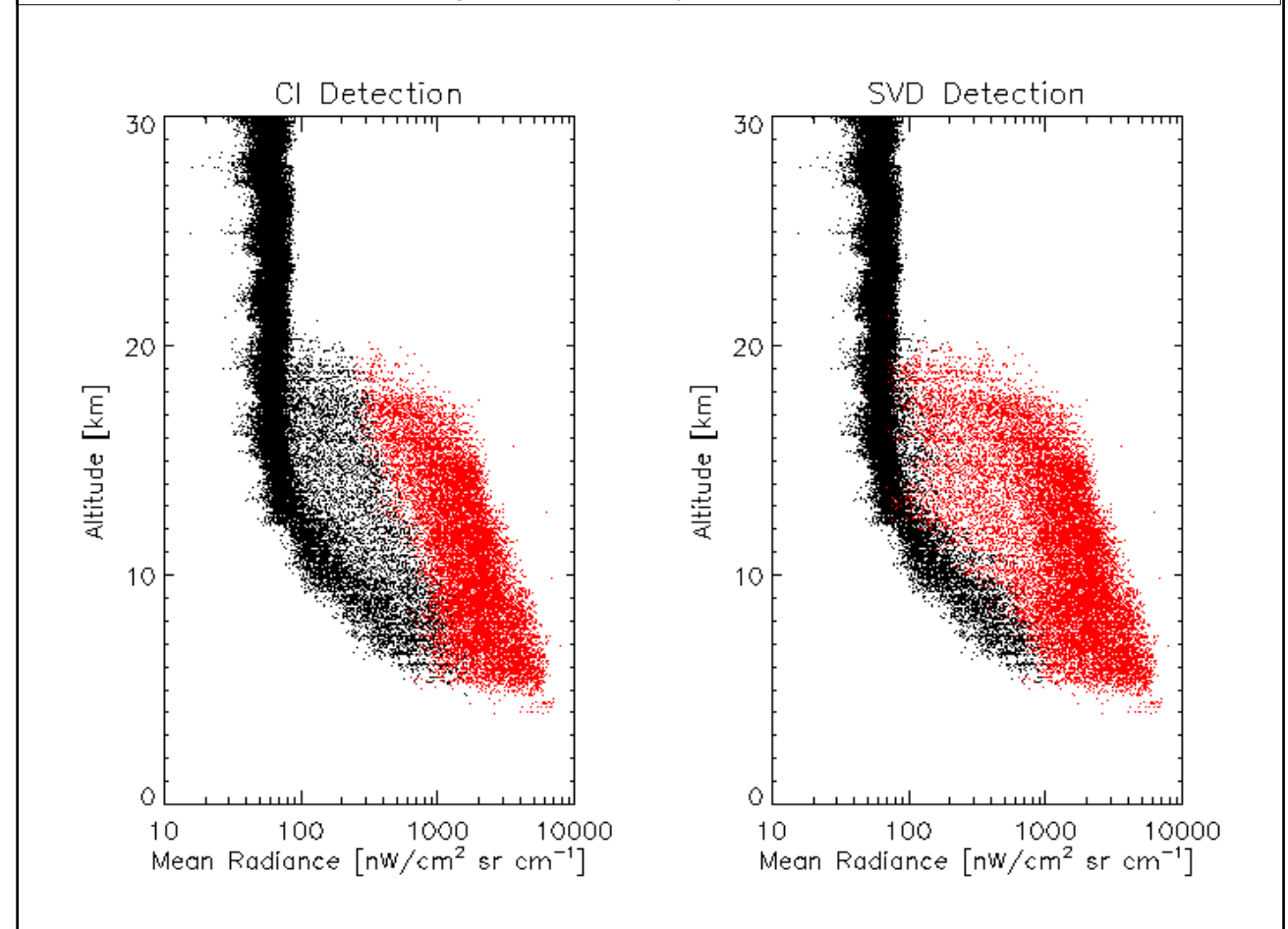


Figure 43: As for Figure 35, except showing the integrated radiance ratio method in the right hand panel.

3.5 Comparison of Cloud Detection Methods

3.5.1 Introduction

Several different methods of cloud detection have been identified, and all can be expressed in terms of a threshold test applied to some scalar parameter

- 1. Current Operational Cloud Index
- 2. Optimised CI microwindows (section 3.3.6)
- 3. SVD chi-squared ratio (section 3.4.6)
- 4. SVD integrated radiance ratio (section 3.4.7)
- 5. Simple radiance threshold

(Test 5 is based on the radiance measured at 960.7cm⁻¹, a point at which molecular absorption is a minimum).

In the absence of any absolute truth, the problem is to determine which of these tests gives the most reliable cloud-detection. The method adopted here will be to compare retrievals (using, for convenience, the Oxford L2 processor MORSE) of 'well-mixed' gases assuming that using spectra with residual cloud will either result in retrievals which deviate significantly from climatology, or at least show up in enhanced fit of the continuum signal within each microwindow.

3.5.2 Threshold Normalisation

Before such a comparison can be made, it is necessary to set the thresholds of each of the methods so that they identify approximately the same proportion of spectra as cloud-contaminated. For a particular nominal tangent height, the cloud-detection parameter is calculated for each spectrum using each of the five methods.

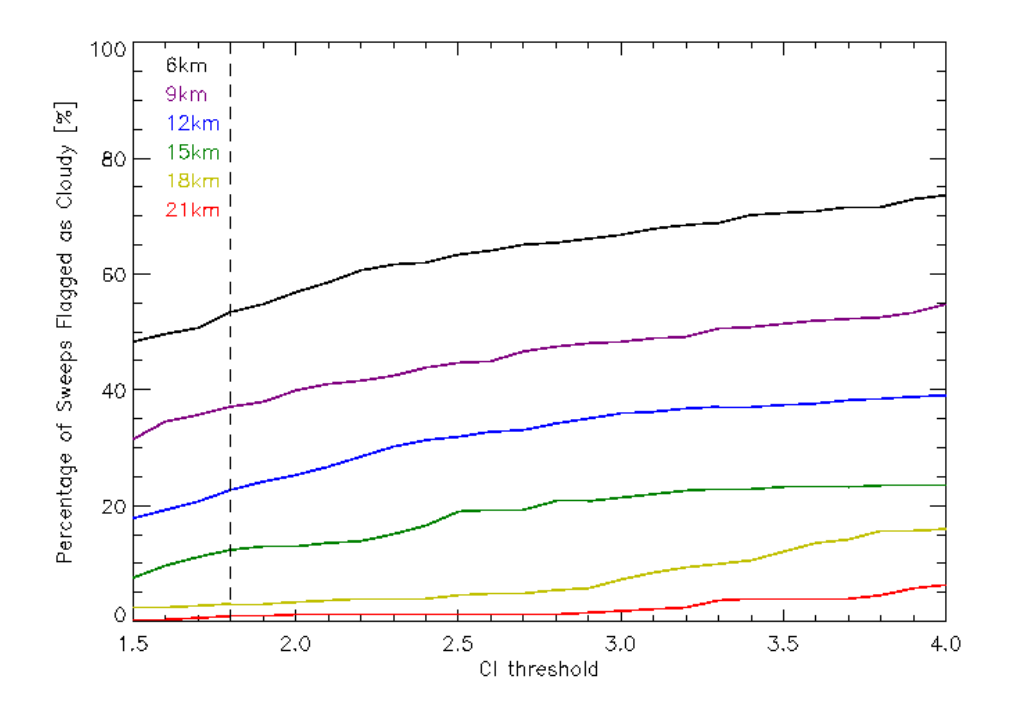


Figure 44: Percentage of sweeps identified as cloudy at each tangent height (colours corresponding to different tangent heights) by CI method as a function of CI threshold. Dashed line shows location of current CI threshold at 1.8.

The percentage of cloud-contaminated spectra for each tangent height is then calculated using the operational CI method (with a threshold of 1.8). Thresholds for the other techniques are then set so that the same fraction of spectra are rejected.

3.5.3 Selecting Intercomparison Cases

For one particular tangent height (ie sweep within the scan), all the scans in the analysed dataset can be classified into one of 3 cases

- 1) All cloud-detection methods flag the tangent height as cloudy
- 2) All cloud-detection methods flag the tangent height as clear
- 3) Different cloud-detection methods disagree over whether it is clear/cloudy

Retrievals are analysed only for those scans conforming to Case (3) and only for the methods which flag the sweep as clear. Since approximately the same number of cloudy/clear scans are detected by each method, it follows that each method will also contribute the same number retrievals to the analysis.

3.5.4 VMR Results

The initial results, based on the analysis of spectra from 15 Aug 2003, are shown in Figure 45. There is no clear best technique, although the chi-square ratio SVD (blue) and the optimised CI

(yellow) generally seem to perform well.

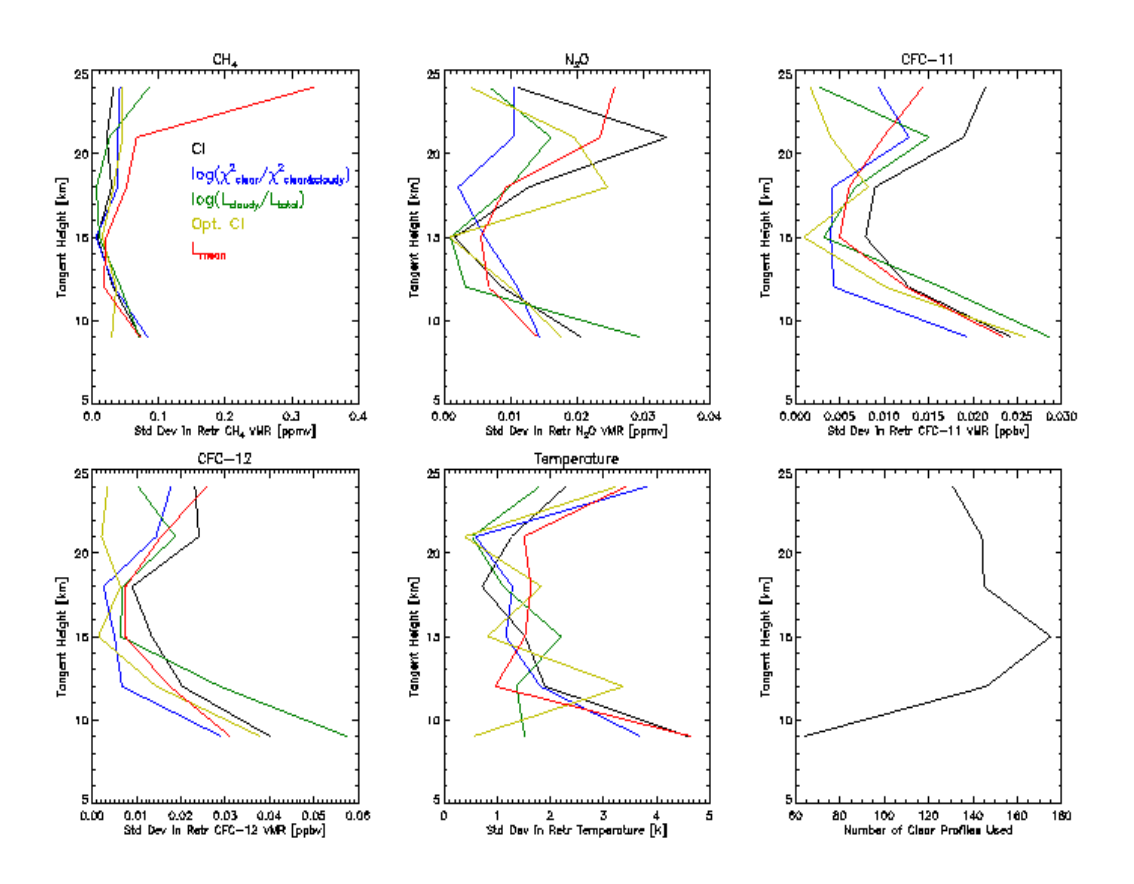


Figure 45: SD of retrieve profiles compared to climatology using the five different detection methods for profiles/tangent altitudes where cloud detection differs. The lower right plot shows the number of such cases as a function of altitude (no cases were found for 6km).

4. Cloud Classification

A classification scheme of the cloud type which is based only on the IR spectra would significantly reduce the complexity to retrieve microphysical parameter. The classification of the spectra in respect to the most likely composition of the events is already a valuable product for scientific analyses. For example the occurrence for PSC types in the MIPAS observations over various winter gave already new insights in the formation mechanisms of Arctic and Antarctic PSCs (e.g. Spang et al., 2005 and Höpfner et al., 2006a/b).

4.1 Status of PSC classification

A multi-colour ratio based on the standard cloud index (CI band A) and a second color ratio sensitive to enhanced emissions by a specific PSC type has been used in various analyses for the MIPAS and CRISTA instrument. An example for the characteristic spectral signature of NAT (nitric acid trihydrate) particles is shown in Figure 46. Höpfner et al. (2006a) [abbreviation: H2006a] showed that the enhancement between 815 and 825 cm⁻¹ is unambiguously related to NAT. NAD (nitric acid dihydrate) is also a candidate for solid PSC article, which show a similar enhancement in modelled spectra, but significantly shifted to 810 cm⁻¹ with its center wavenumber. Latter type of spectra have not been observed so far in the MIPAS data (H2006a). But should be tracked in the future prototype processor system.

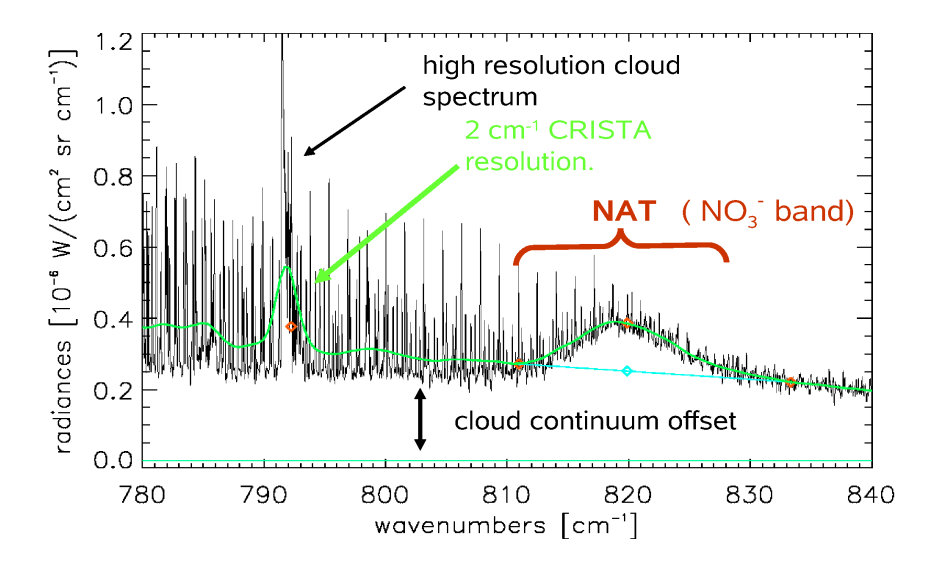


Figure 46: Example for the NAT enhancement at 820 cm observed by MIPAS. Superimposed a reduced resolution spectrum in green.

The detection works due to the compact correlation between the standard cloud index (CI band A) versus a color ratio for NAT by the mean spectra intensity at 819–821 cm⁻¹ divided by the intensity at 788.2–796.25 cm⁻¹. This is illustrated in Figure 47 for MIPAS measurements and in Figure 48 for modeled spectra at 20 km of the CSDB. Figure 47 highlights the separation in different regimes (H2006a/b). R1 contains NAT particles with mean radii smaller than 3 µm. Ice PSCs are located in R3. R2 data are most likely STS, but large NAT or thin ice layers cannot be excluded. In R4 it is difficult to distinguish among ice, STS and large NAT. Due to the larger amount of possible scenarios than used in H2006a the CSDB will now allow to improve the separation criteria.

First examples of the sensitivity in the correlation diagram is shown in Figure 48-50 for NAT, STS and ice. The high sensitivity in respect to radius is very well shown in the modeled scatter plots at 24 and 16 km. STS and ice how no indication for crossing the separation line for CI-values < 4-5 (cloudy conditions). The separation line used in the Figures is the originally empirical fit to CRISTA results (Spang and Remedios, 2003). H2006a developed a separation line based on their small database. It is based on a fit of the compact correlation of ice and STS. The curve is then shifted to separate NAT particles smaller than 3 μ m from larger particles. The new CSDB approved this approach quite well. The NAT model runs shows the well defined separation with particle radius. In contrast larger NAT particle are difficult to differentiate between STS and ice. However, ice shows the smallest CI-values due to the larger possible volume densities, like illustrated in the measurements. This allows the classification for ice clouds of large optical thickness or respectively large slant ice water columns in the limb path (CI < 1.3).

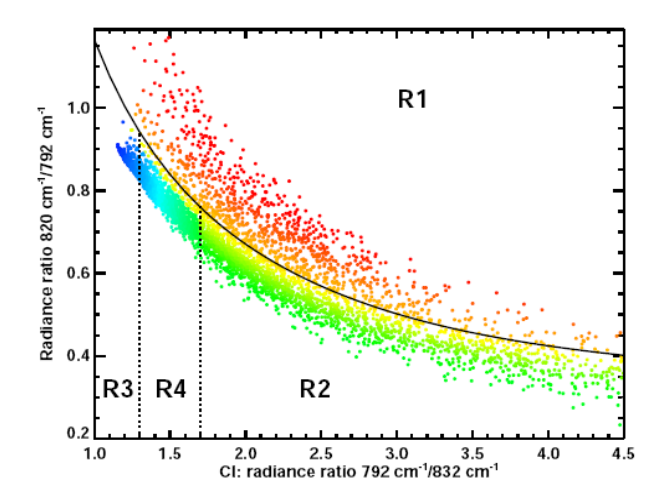


Figure 47: Standard cloud index versus NAT colour ratio (details see text) for MIPAS measurments (left) and modelled CSDB spectra for NAT (right) at 20 km altitude. On the left side seperation lines

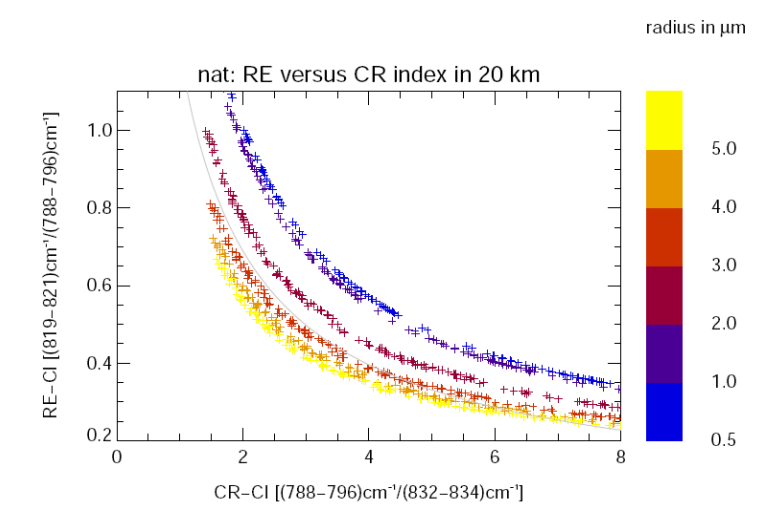


Figure 48: Standard cloud index versus NAT colour ratio (details see text) for modelled CSDB spectra at 20 km.

Figure 49: Standard cloud index versus NAT color ratio for modelled CSDB spectra at 20 km.

NAT type similar particles have been observed in various in-stitu measurements in the UTLS region (e.g. Voigt et al., 2006). Despite the detection will be very difficult due to the little amount of HNO3 in this region, the analysis method outlined above should applied to the tropical an midlatitude observations as well. The large number of MIPAS observations might allow to detect peculiar events of NAT type clouds under certain conditions.

4.2 Improved PSC classification based on CSDB

Various brightness temperature differences (BTD) have been tested for the classification of cloud types in combination with the CI-CR and a second BTD. Scatter plots are a well established method for the differentiation of cloud classes, if a combination of two parameters are creating a distinctive separation in two or more classes/areas.

Differentiation ICE and STS

In this example (Figure 50) a MW-pair has been used, where a significant separation between ice and STS can be observed, also for optically thinner conditions (2 < CI-CR < 5). For example a BTD<-7K and CI>1.5 is definitely not related to NAT and vice versa for STS. However, the third type NAT allows not an easy straight-forward classification (see next section).

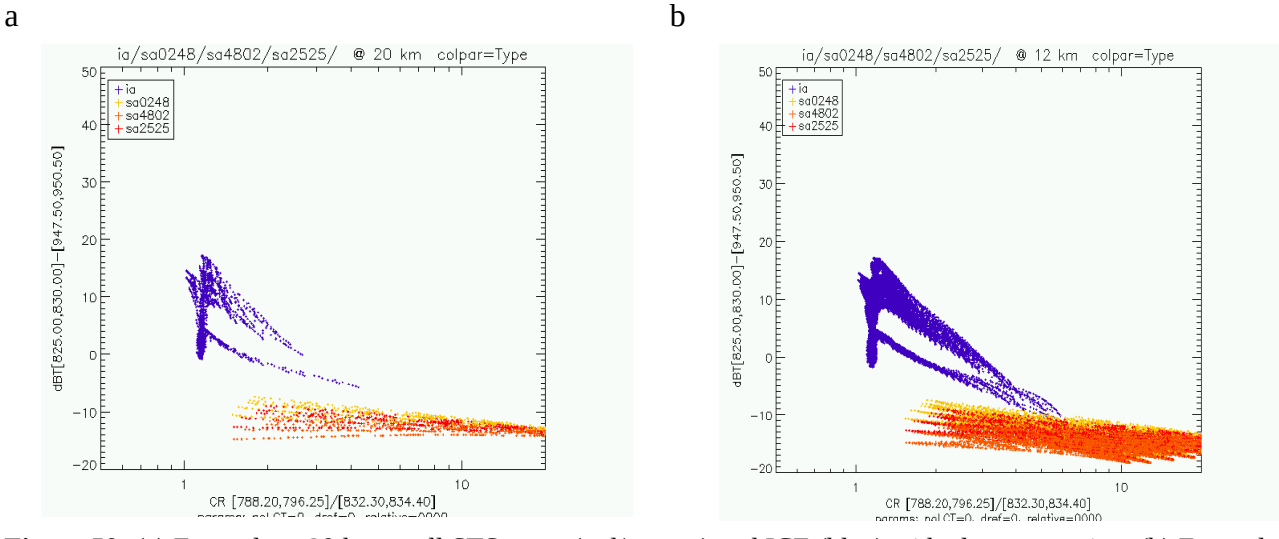


Figure 50: (a) Example at 20 km or all STS types (red/orange) and ICE (blue) with clear separation. (b) Example 12 to 18 km altitude for all STS types (red/orange) and ICE (blue). Obviously STS and ICE are still well separated, but are merging slightly together around BTD=-10K and moderate CI-CR= 4 to 5.

Differentiation NAT and ICE:

This is working very similar to STS. We changed the MW1 for BTD in direction away from the 820cm-1 to 832-834cm-1. The distributions are changing not very much to different altitude levels but show some more overlap between STS and ice for CI-CR around 2-4 and BTD around -5 to +5 K (Fig. 51a) than the STS/ice plots. This is obviously (Fig. b) the case for large ice particles but small NAT particles. For small NAT particles in interplay with the 820 cm⁻¹ NAT-bump it will be possible to set up a more unambiguous differentiation scheme.

Constrains:

The possibility that even thinner ice PSCs (larger CI-CR) are formed than assumed in the CSDB is quite unrealistic. However FOV effects can reduce the signals in a way, that it is similar to an even optically thinner ice PSC. This has to be investigated in the future. Optically thinner ice PSCs, better described with smaller slant/limb Ice Water Path (IWP) (Fig. d) or with area density path (ADP, see also section 5.2.5), might extend the BTD to negative values and would cause more overlaps with the NAT area. Optically thicker NAT clouds are also realistic. Extreme values in the HNO3 amount in the polar stratosphere would extrapolate the NAT CI-CR in direction close to 1.

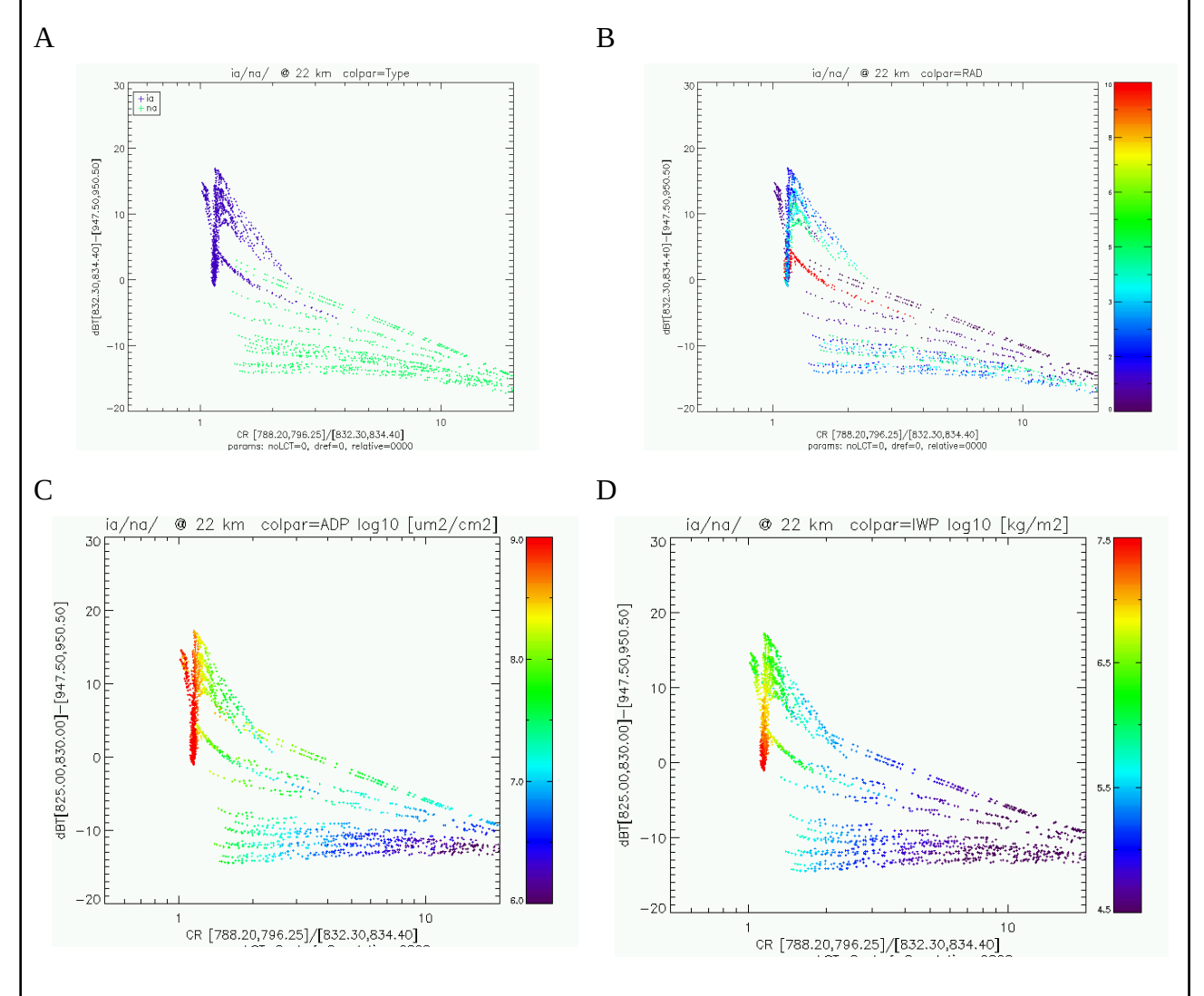


Figure 51: CI-CR versus dBT sensitive for solid/liquid particles for PSC ice and NAT at 22 km. Colour coded (a) for cloud type, (b) particle radius, (c) area density path, and (d) limb ice water path.

Summary: Despite some limitations in the differentiation, ice is the only candidate of all PSC types for dBT(830-947) > 0 (4) K, which seems a quite robust classification.

Differentiation STS and NAT

This is a very difficult task, due to the quite similar refractive indices and typical volume densities. The following example show the altitude dependence at 19, 15 and 24 km, but a indications for a clear separation between STS and NAT, where one BTD is sensitive to the 820 cm-1 NAT bump for small particles (r<3-4microns) and one BT difference sensitive to radius (and possibly cloud type as well).

The STS events fall always between the small and the large particle radius for NAT (Figure 52), with some mixture for radii around 1.5 micron (Fig. b). However the well established differentiation of small NAT particles up to 2-3 micron radius (section 4.1) is a solution for this dilemma. Whereby the figures below show show a significant sensitivity to separate large NAT particles.

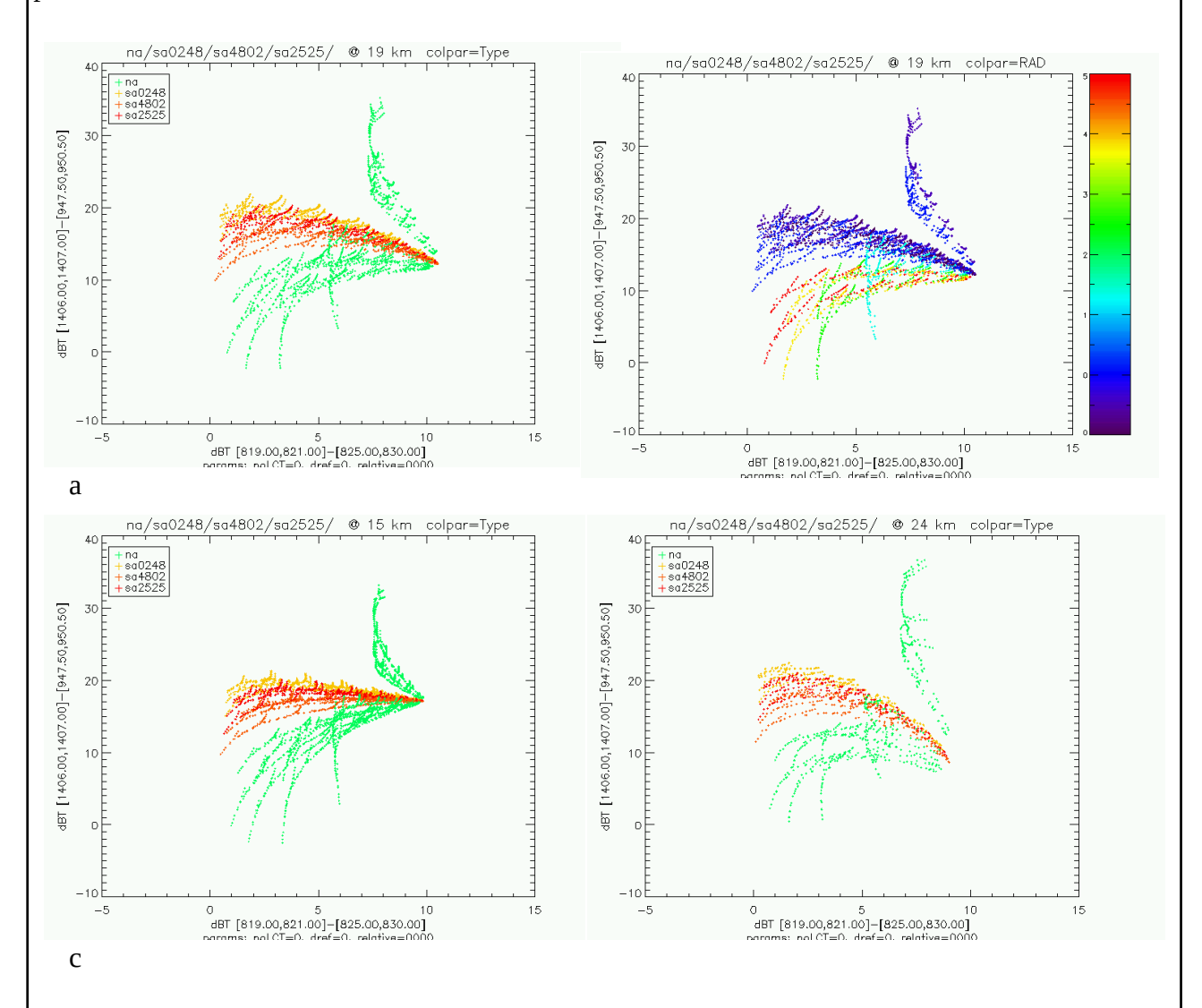


Figure 52: Examples for BTDx versus BTDy for NAT and STS at various heights (blue and orange/red in a,c,d) and in respect to effective radius (b), details see text.

Some further investigation with the same MW-pairs show a rough separation in different regions for all three PSC types (next figure) over all altitudes. Ice seems well separated to NAT. STS is spread in the vertical between the two regimes. The two regions are schematically highlighted by the dashed line in Figure (a). Obviously the STS/NAT classification is still difficult. The variation with BTDx is mainly caused by the varying area density path for STS and NAT type clouds like

illustrated in Fig. (e) (in parts also by altitude and radius, but these have a bigger impact on BTDy).

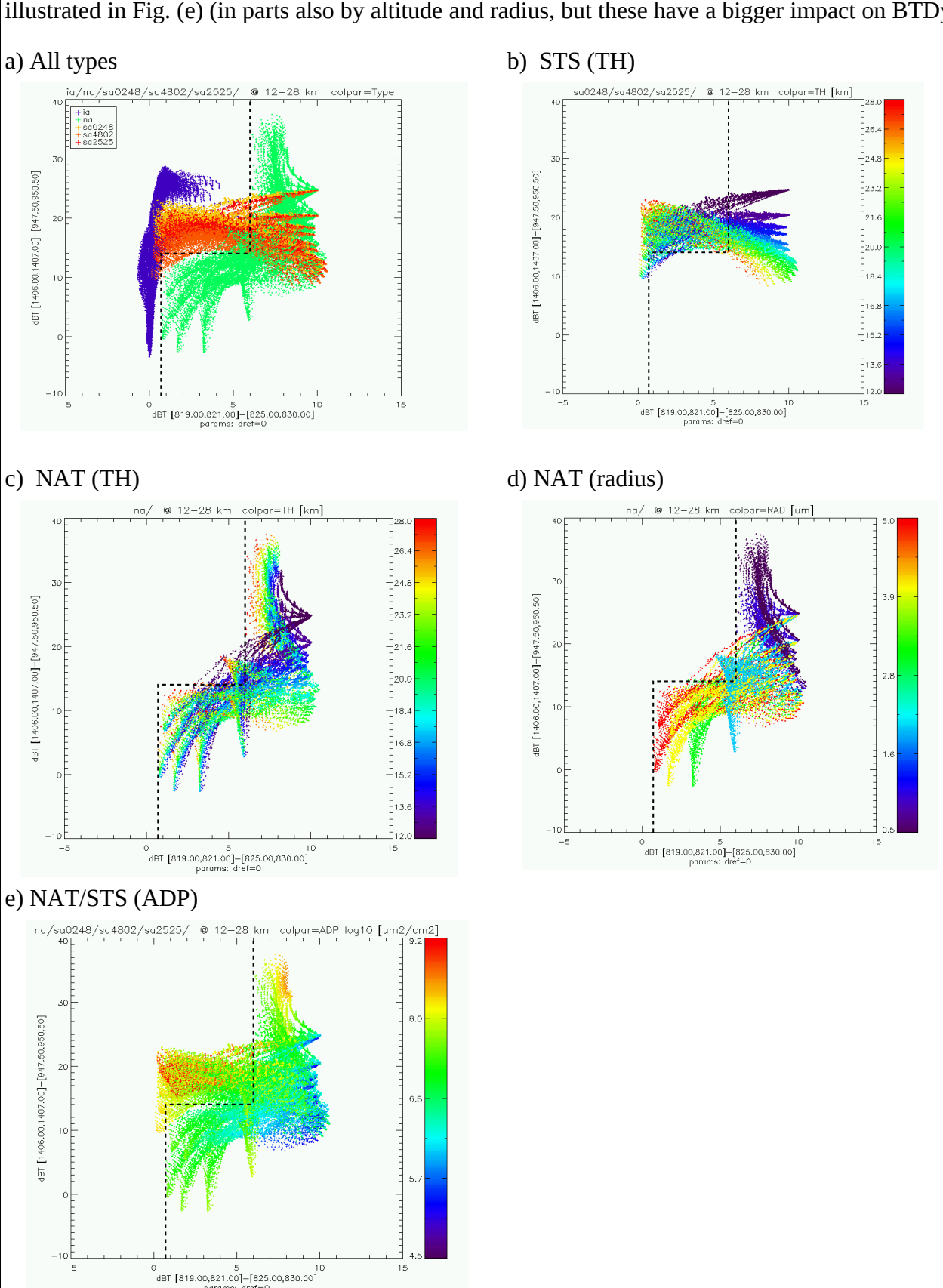


Figure 53: BTD scatter plot sensitive to composition (a) colour-coded for PSC type, (b-c) STS and NAT colourcoded THs, and (d) NAT colour-coded particle radius, (e) only STS and NAT in respect to area density path (ADP).

4.3 Differentiation of Cirrus and Liquid clouds based on CSDB

The first try to differ between liquid and solid particle was not promising. The refractive indices are looking too similar over a broad region. However, there should be contrast between 925 cm-1 (10.8 um) and 833 cm-1 (12 um), typically used by nadir instruments for this kind of application. (e.g. Li et al., 2003, Strabala et al., 1994 in J. Appl. Meteorology).

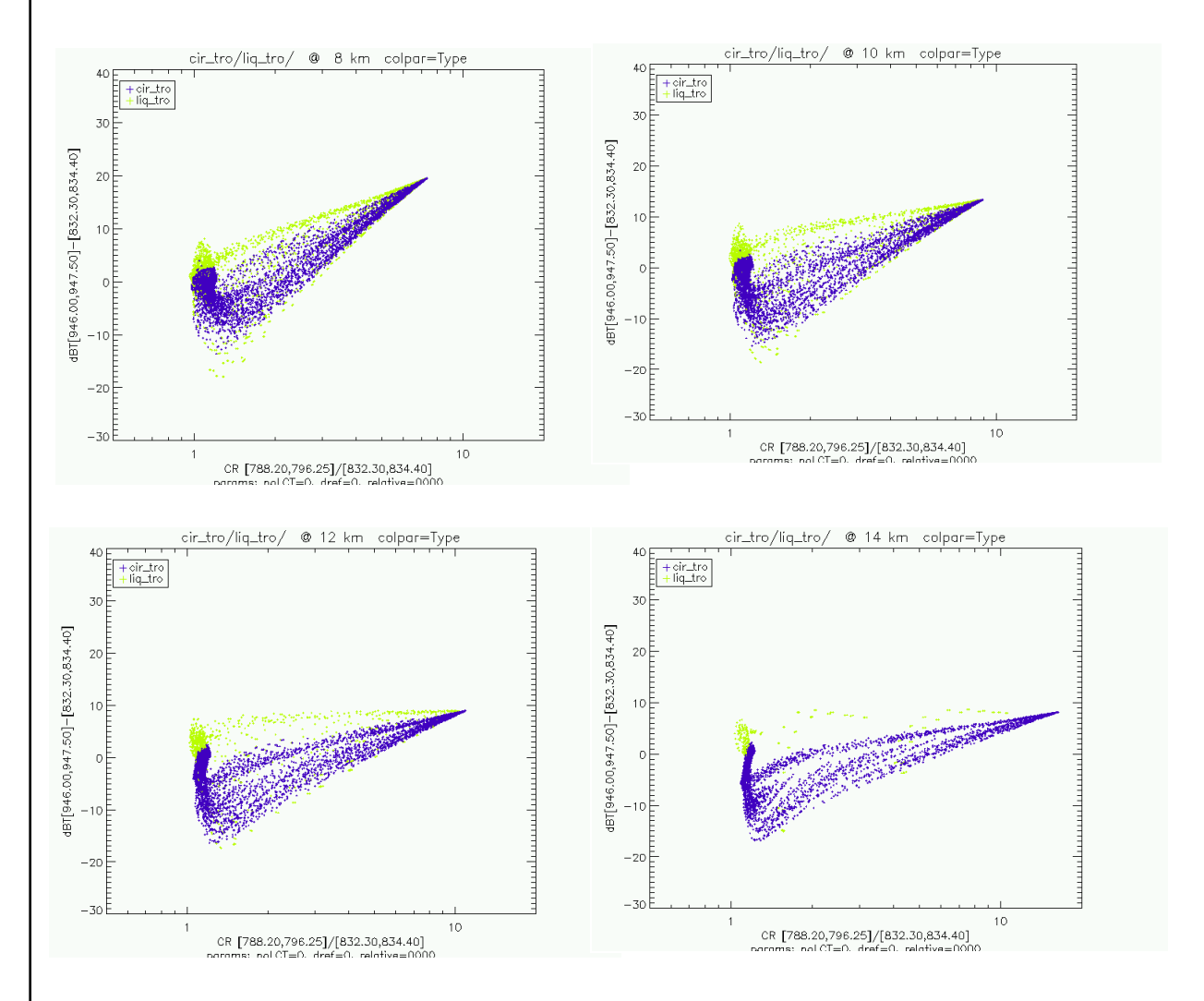


Figure 54: CI-CR versus BTD typically used for liquid/solid differentiation for nadir instruments for CSDB spectra of liquids an cirrus particles at various altitudes for tropical conditions.

Examples for the nadir wave lengths with CI-CR on the x-axis. There is a strong overlap (difficult to see) for small 1<CI<1.3 around BTD=0K for liquid and cirrus particles. This highlights the difficulties to differentiate optical thick cloud scenarios. Optically thinner conditions have the tendency to separate (BTD>0 for liquids and BTD<0 for solids), but a part of the liquid scenarios are just spread in the area typical for cirrus. This overlap is mainly caused by PSD with small liquids particles (Reff<5um) as illustrated in the Figure 55. This shows a strong dependence on the BTD between 830 and 950 cm⁻¹, which can be observed for a number of the 900 wavenumber MWs. In consequence these BTD are better suited to retrieve radius information than type information.

Mid-lat and polar summer scenarios show a similar behaviour in the correlations but with different gradients at certain altitudes.

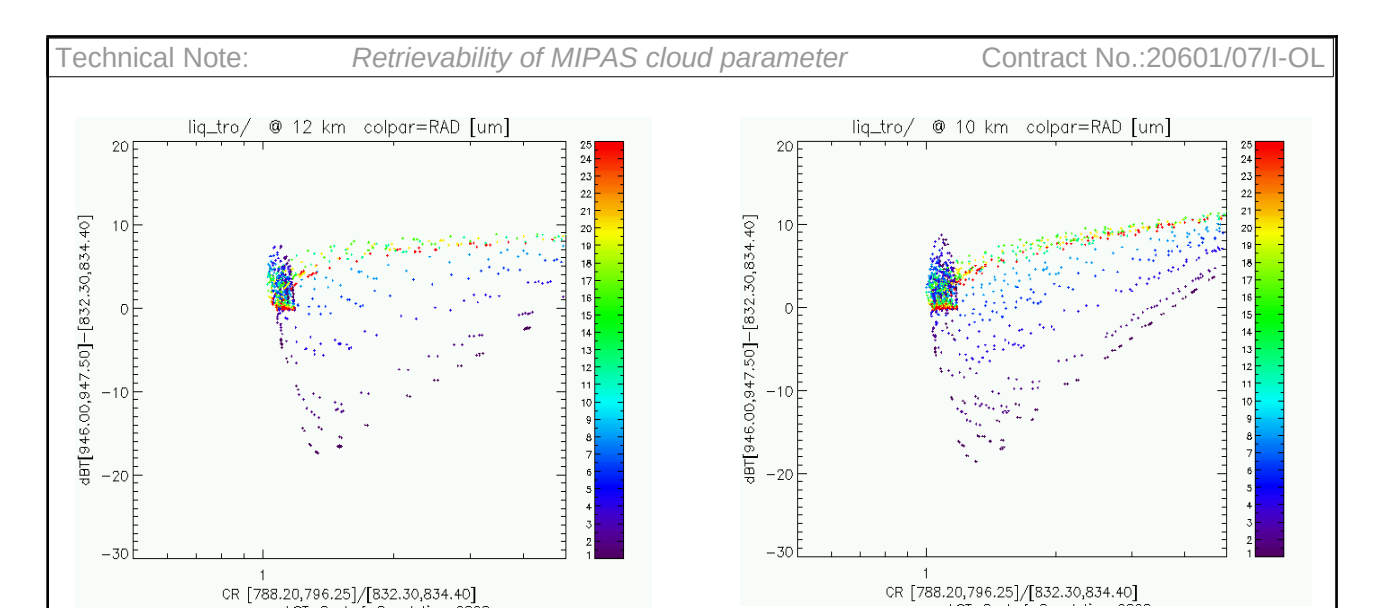


Figure 55: Same as figure before but for liquids with tropical profile at 12 and 10 km and color-coded effective radius.

Following pictures show the sensitivity with altitude for CI-CR in respect with the water index, originally used for the CRISTA-NF data (Spang et al., ASR, 2007). The CSDB shows higher BTD(H2O) than in the observations (see presentation Phase1PM) and a very strong altitude dependence, which is presumably caused by the vertical water vapour gradient (high water at low altitudes => potential for large BTD(H2O). More investigations are necessary to optimise a classification scheme. For example the variation of CI-CR in respect with varying water vapour background values has to be quantified (e.g. by climatological variability of H2O and cloud-free forward calculations, see above), similar to the CRISTA-NF analyses (Spang et al., ASR, 2007).

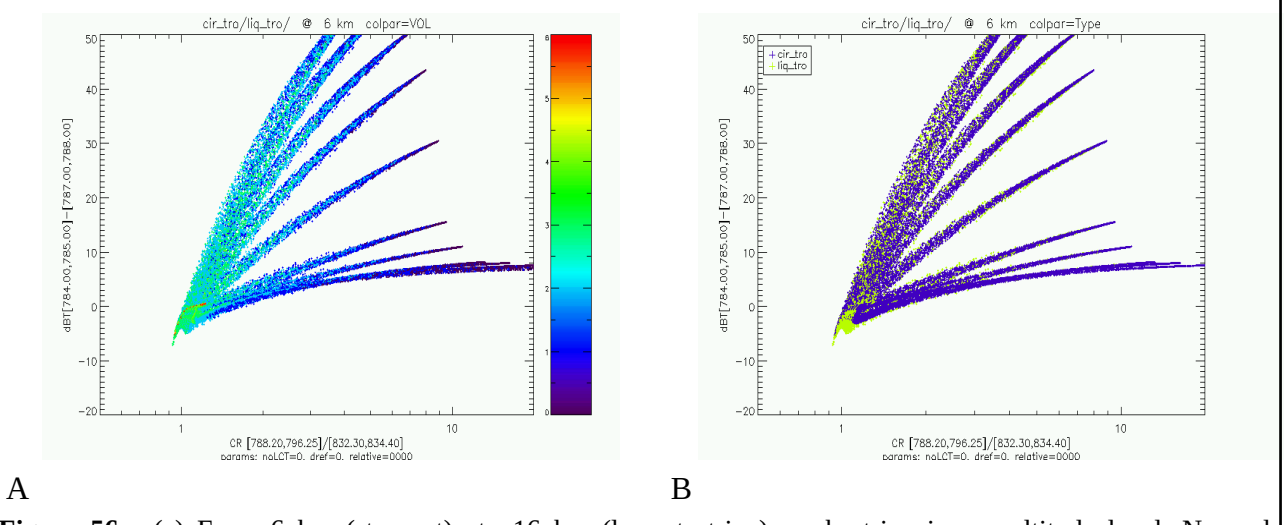


Figure 56: (a) From 6 km (steepest) to 16 km (lowest stripe), each stripe is one altitude level. No real correlation with Volume (the color code) can be observed. Liquids and cirrus show similar scatter in one stripe. (b) From 6 to 14 km only, but color-coded particle type.

Another important parameter for the classification for optical thick clouds is temperature, here would be the cloud top temperature CTT a helpful information. This can be retrieved for MIPAS by ecmwf analyses data respectively for the CSDB it is just the temperature of the climatology profile at CTH. First indication for this fact is the dependency with altitude (Figure 57a) of a BTD sensitive to liq/solid for low CI-CR (<1.2). Zooming into the optically thick area gives more information and show some indication for a separation between liquid and solids for optically thick conditions (0.8<CR-CI<1.2)

How good a separation works in the BT direction depends on the lowest altitude you use. Cirrus

bellow 8 km tends to fill the area dominated only by the liquids (top left and right corner). The separation line needs to be shifted for different background climatologies, which can be again a temperature effect and needs further investigations. The method seems to work for PSC as well (d), but volumes comparable to ice PSCs were not modeled. The amount of HNO3 the polar stratosphere causes a natural limitation of realistic NAT and STS volume densities. In consequence CI-CR < 1.3 seams here only related to ice PSCs. However, an update of CSDB will include higher volume densities for NAT and STS (using extreme HNO3 values). An update of this analysis is necessary with the extended CSDB.

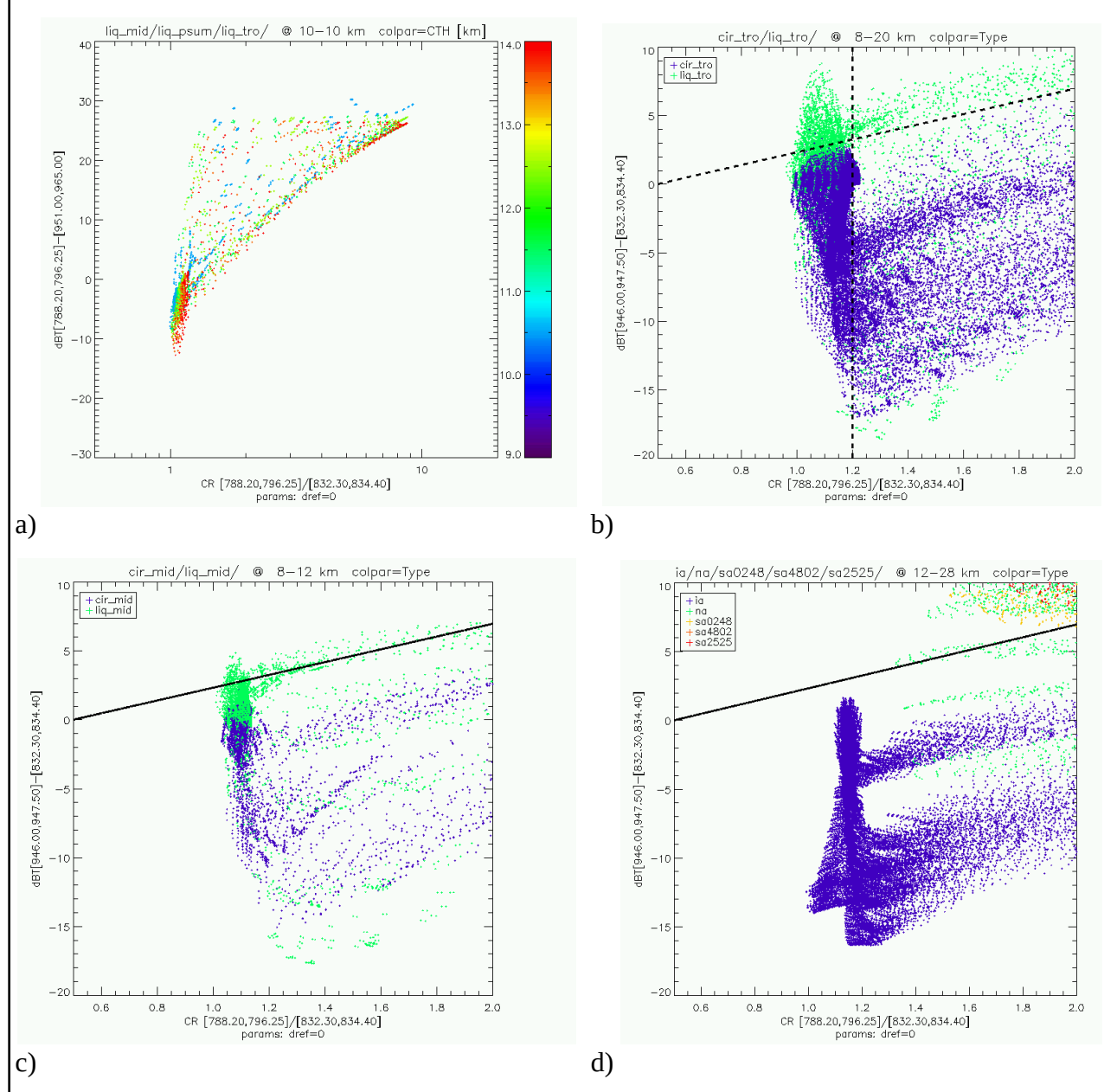


Figure 57: CI-CR versus various BTDs senstive to composition under various conditions. (a) Only liquids, (b/c) liquids togeter with cirrus for tropics and midlatitudes respectivelly, as well as (d) PSC types.

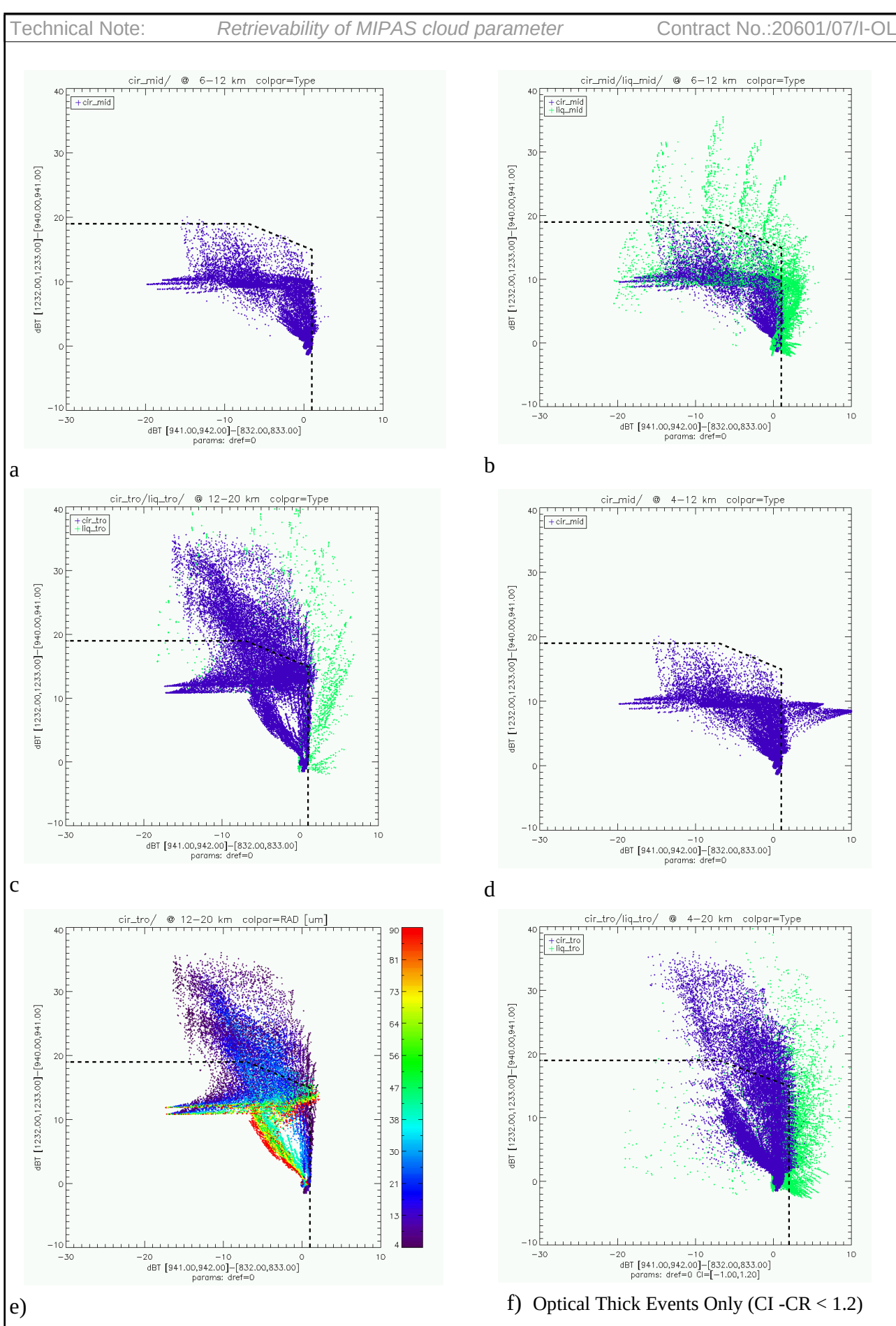


Figure 58: Multiple BTD scatter plot sensitive to composition under various conditions. See figure caption for details.

We tried to optimise the liquid/solid effects in the BTD correlation plots, by varying through as much as possible one-wavenumber combinations. Like already mentioned the 941-832 cm-1 difference is quite sensitive to the solid/liquid differentiation (Figure 58). But liquids can spread into the cirrus area for certain conditions. For mid-latitudes a simple separation line would work quite well. BTD > 1-2 K is only related to liquids. In addition, the BTD for 1232-940 cm-1 is > 20 K only for liquids as well. However, the last separation disappears, when looking into tropical latitudes. This is caused by the drift of small particles to higher BTD y-values (Fig. e) in the tropical case. This is associated with short path lengths (IWP) for large BTD values.

Unfortunately, the first good separation (BTD > 1-2 K) gets lost as well, when reaching lower altitudes (< 6 km for mid-latitude liquids Fig. (d), and < 8 km for tropical cirrus/liquids). But the classification still works if the analysis is restricted to optically thick clouds (CI-CR [796/832] < 1.2) like shown in Figure (f), where for the altitude range 4-20 km one can find only liquid particle with BTD[941-832] > 2-3 K.

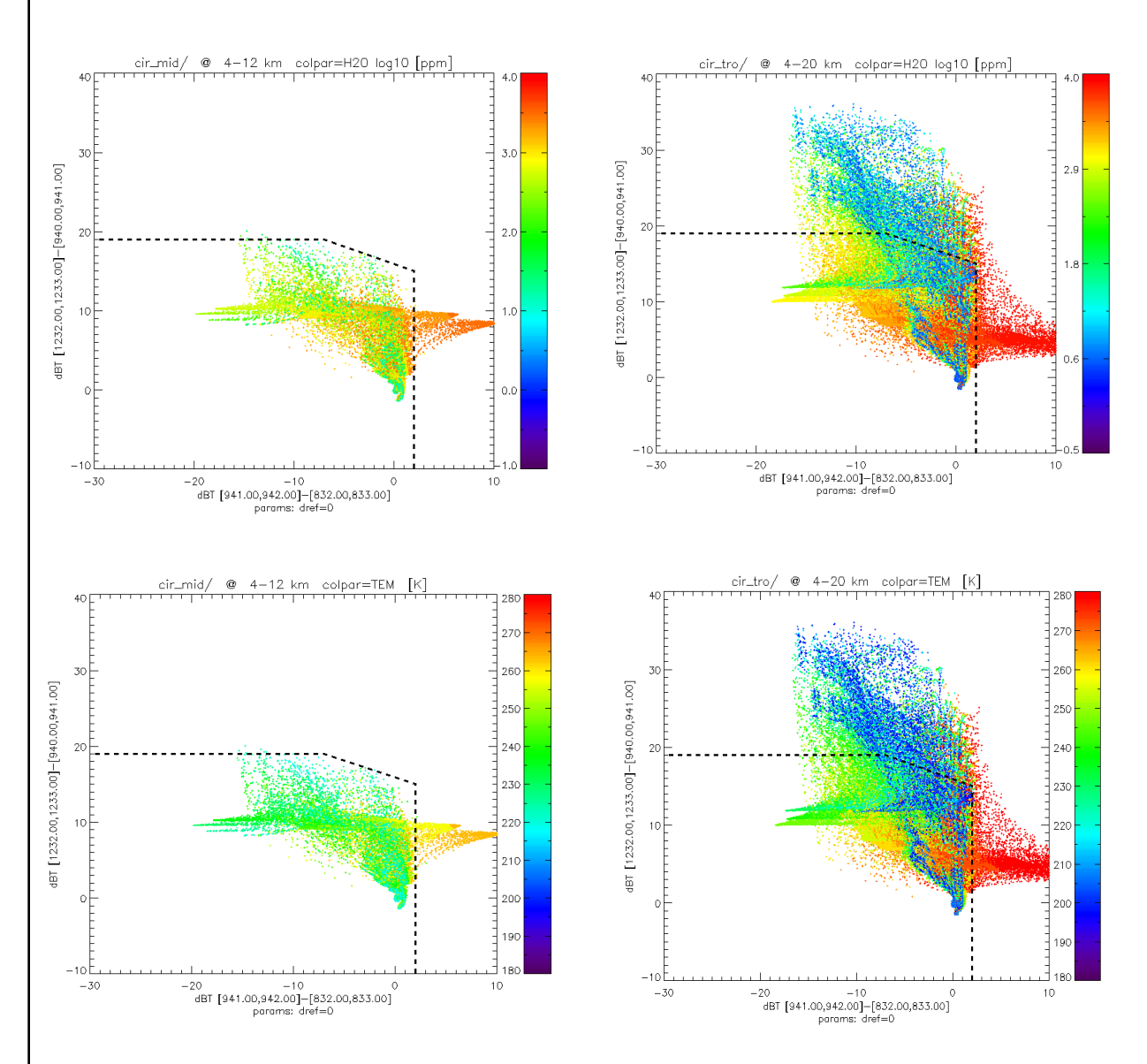


Figure 59: Water vapour (top) and temperature (bottom) dependence of all scenarios for mid latitudes (left) and tropics (right).

Temperature and water vapour might produce such altitude dependent changes. This is highlighted by the Figures 59 where lowest altitudes and in consequence warmest temperatures are linked to the enhancement in BTD[941-832] for mid-latitude and equator conditions.

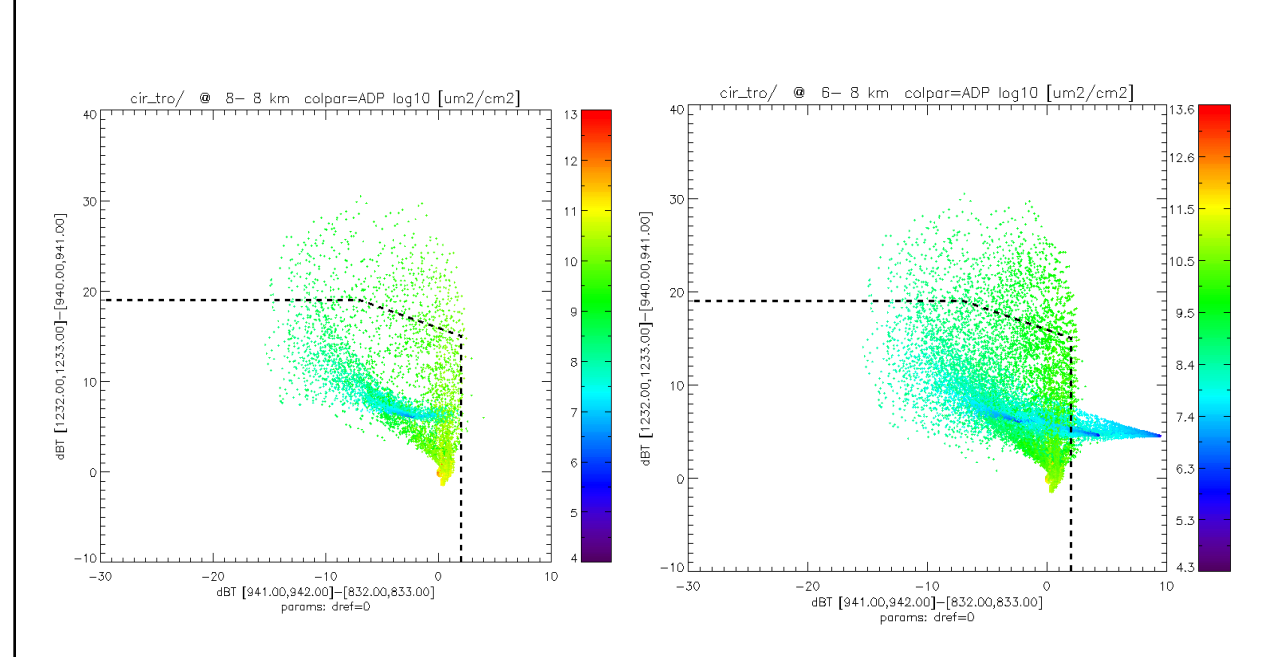


Figure 60: Separation in altitude for 8 km and 6-8 km of color coded area density path (ADP).

Figure 60 show that the enhancement in BTD[941-832] (<2K) at lower altitudes is caused by the spectra, where ADP is small. These events moving from negative to positive BTD with decreasing altitudes. The optically thin cloud spectra are changing the spectral form by the radiation of the lower altitudes, especially if the cloud layer is well above the tangent point.

Conclusions:

So far no unambiguous BTD or CR based differentiation scheme were found for ice particles. For liquid clouds a large amount of the scenarios result in a positive BTD[941-832] >1-2 K.

4.4 Index for scattered tropospheric radiation

In a first analysis of the CSDB we liked to proof if scattering effects of tropospheric radiations are obvious in the modeled spectra and how much particle size information might be extracted from this. Höpfner et al. (2002) showed already characteristic absorption features in balloon based IR spectra. Spang et al. (2003) (hereafter S2003) had investigated if it is possible to detect these events in MIPAS spectra around the tropical tropopause. They found quite a large amount (40%) of cloud contaminated spectra with indication of absorption features. Here, we investigated first if the modeled PSC spectra show the same features and might allow to retrieve information on particle size.

The Cloud Scattering Index (CSI) based on S2003 was applied to the CSDB by using MWs in the region of an absorbing H_2O line (MW1: 803.50-803.60 cm⁻¹) and a region close to it (MW2: 803.70-803.90 cm⁻¹). Computing the ratio for the mean MW-radiances [MW1-MW2]/[MW1+MW2], which is equivalent to half of the relative difference, negative values give immediately the indication for an absorption feature, like illustrated in the spectra of Figure 61 for the 803-805 cm⁻¹ and 947-950 cm⁻¹ range.

Figure 62 illustrates that quite a large number of scenarios for NAT and ice particles show this negative anomalies. The behaviour of the database is very similar to the MIPAS observations (Figure 63). STS composites show only very weak indications for scattered tropospheric radiation (not shown). This fact takes into account the typically smaller particle radii of STS with respect to

NAT and ice clouds, where Mie scattering is significantly less efficient. This was considered in the model runs by maximum median radius of 1 micron for STS compared to 5 and 10 micron for NAT and ice respectively.

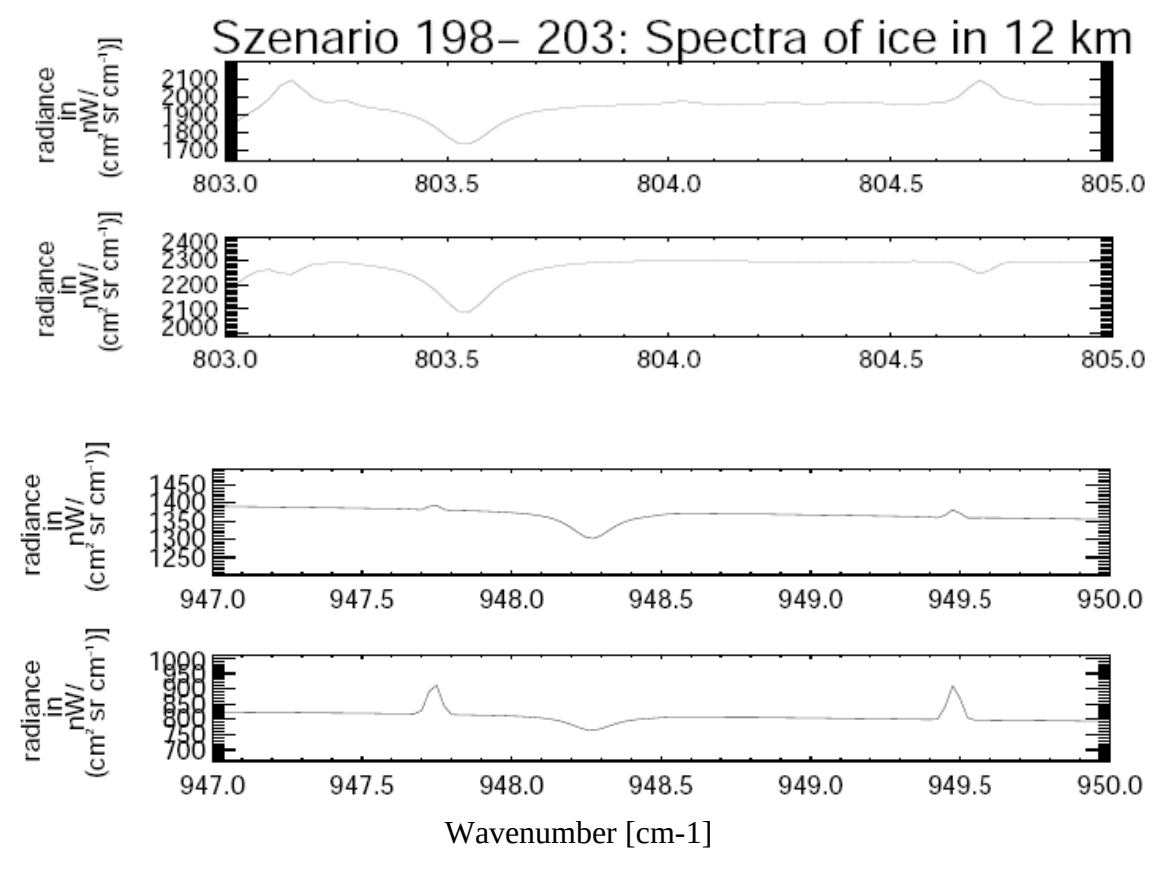


Figure 61: Example of modeled spectra in the 803-805 (top two) and 947-950 (bottom two) wave number range from the CSDB for a vertically thick and thin layers of PSC above the tangent height .

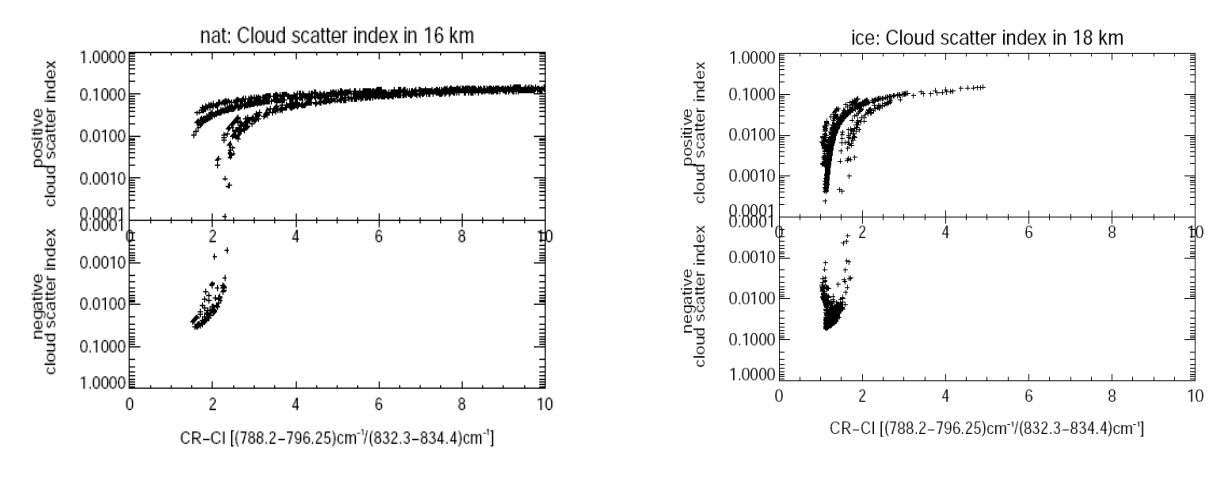


Figure 62: CI versus cloud scattering index based (CSI) for CSDB spectra for NAT at 16km and ice clouds at 18km. CSI becomes negative if absorption features occur in spectra. Here the CSI after Spang et al. (2003) have been applied.

Different wavelength regions might have an even better sensitivity for this effect, like illustrated in Figure 61 for the 947-950 cm⁻¹ region. The anomalies in the 803.60 cm⁻¹ are sometimes very close to the noise level of the corresponding detector band (A). We therefore made a simple test with MW1=948.25 cm⁻¹ and MW2=948.60 cm⁻¹. This index shows significant increasing negative anomalies with increasing radius (Figure 61). But this is only the case for scenarios where no tropospheric cloud layer (at 6km, see section 2) is modeled. These cloud layer seems to reduce the

incoming radiation for scattering effects just effectively that any absorption features disappear.

Summary

One can use a cloud scatter index for better and fast characterisation of the spectra dominated by large or small particles as well as further step for cloud detection. The sensitivity to particle size has to investigated in more detail, by consideration of the Jacobian spectra of CSDB to proof if a gross particle size information can be retrieved with sufficient accuracy.

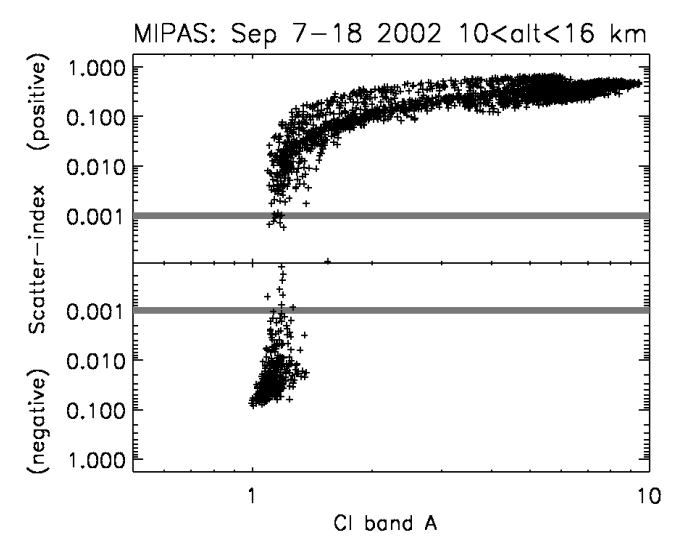


Figure 63: CI-A versus CSI from Spang et al. (2005) for MIPAS measurements in September 2002. Negative values implies absorption feature in the spectra at 803.5 cm⁻¹ region. Gray horizontal bars illustrate significant detection limits.

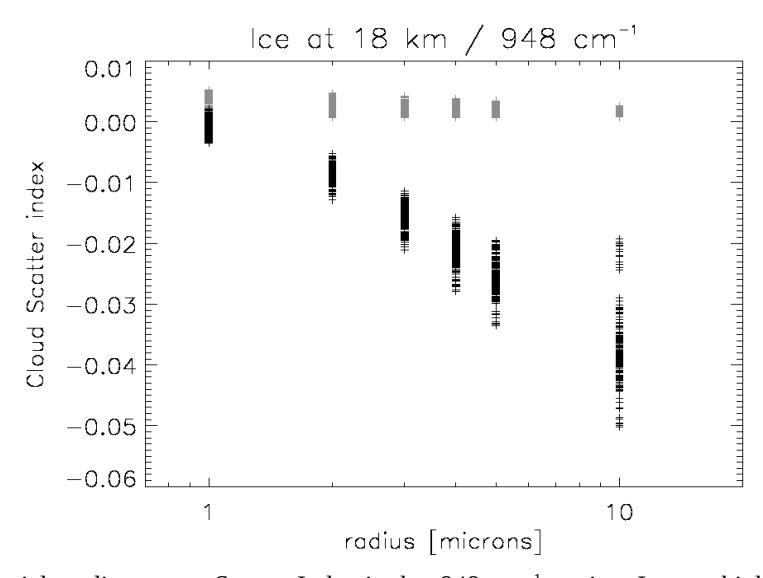


Figure 64: Modelled particle radius versus Scatter-Index in the 948 cm⁻¹ region. In grey highlighted the events with tropospheric cloud layer at 6km.

5. Retrieval of Physical Cloud Parameter

5.1 Marcophysical Parameter

5.1.1 Introduction

Macrophysical parameters refer to the bulk properties of clouds for which they can be treated as simple grey absorbers. Specifically these are:

Cloud Top Height (CTH) [km]
Cloud Top Temperature (CTT) [K]
Cloud Extinction (CEX) [/km]

5.1.2 Radiative Model

Neglecting the molecular contributions to atmospheric radiance, the macroscopic parameters are related to the transmittance of a line-of-sight path at tangent height z by

$$\tau(z) = e^{-k*x(z)}$$

where k is CEX, and x is the horizontal distance through the cloud given by Pythagoras theorem

$$x \approx 2\sqrt{2R(t-z)}$$

where t is the CTH, R is the radius of the earth ($_{R\gg_{z,t}}$ assumed).

The radiance L(z) of such a pencil beam is given by

$$L(z) = \int_{los} B(x) \frac{d\tau}{dx} dx$$

where B is a function of the temperature profile within the cloud, assumed to decrease from the cloud top temperature CTH at the wet adiabatic lapse rate.

And finally the measured radiance from nominal tangent height h is the convolution of the vertical radiance profile with the normalised FOV response

$$R(h) = \int_{FOV} L(z) \Psi(z-h) dz$$

5.1.3 Molecular Absorption

In practice, every part of the MIPAS spectrum contains some contribution from atmospheric gases which can appear as absorption or emission features superimposed on the cloud continuum radiance, depending on the thermal contrast between the cloud and the atmosphere above the cloud (and below the cloud in the case of thin cloud).

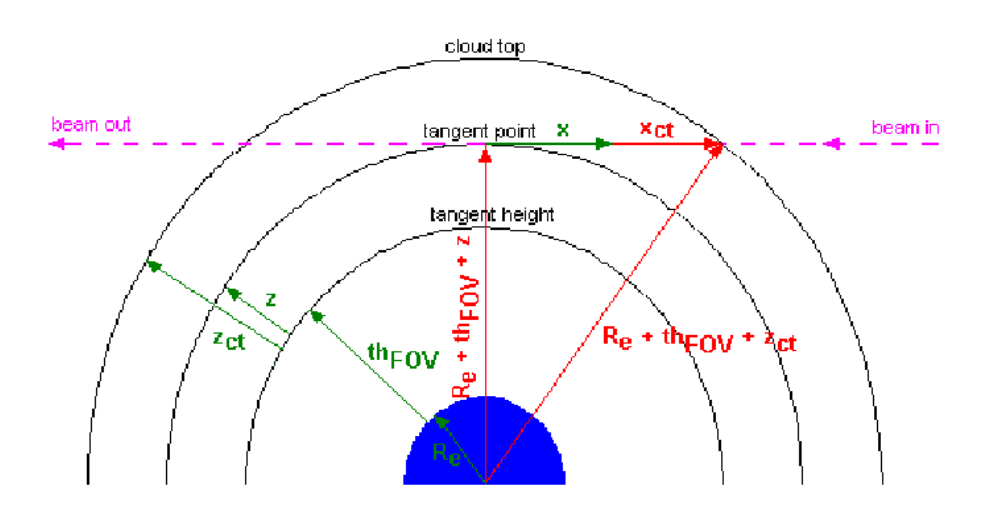


Figure 65: Schematic of the viewing geometry of MIPAS with a cloud in the FOV.

However, by selecting a microwindow for which the gaseous absorption is a mininum a simple correction for residual contributions can be applied by assuming that the net contribution will be the sum of a continuum term plus some fitted scaling factor multiplied by the gaseous emission spectrum

$$R_m = R_c + a * R_g$$

where $R_{\rm m}$ is the measured radiance spectrum in the microwindow, $R_{\rm c}$ is the continuum contribution due to cloud and $R_{\rm g}$ is the precomputed cloud-free molecular spectrum, and a is the fitted parameter. From this, the continuum radiance $R_{\rm c}$ is extracted.



Figure 66: sketch showing the treatment of radiance contributions from gaseous emission in the presence of cloud.

5.1.4 Thick Cloud Retrieval

To derive the three macroscopic parameters from a single partially cloudy radiance R clearly extra measurements or constraints have to be applied. The first assumption will be that, having identified the sweep containing the cloud top, the sweep immediately below will be view the same cloud (i.e. that the horizontal displacement from one sweep to the next is not significant). Figures 67 and 68 show simulated radiance measurements for such a pair of measurements assuming a fixed cloud-top temperature.



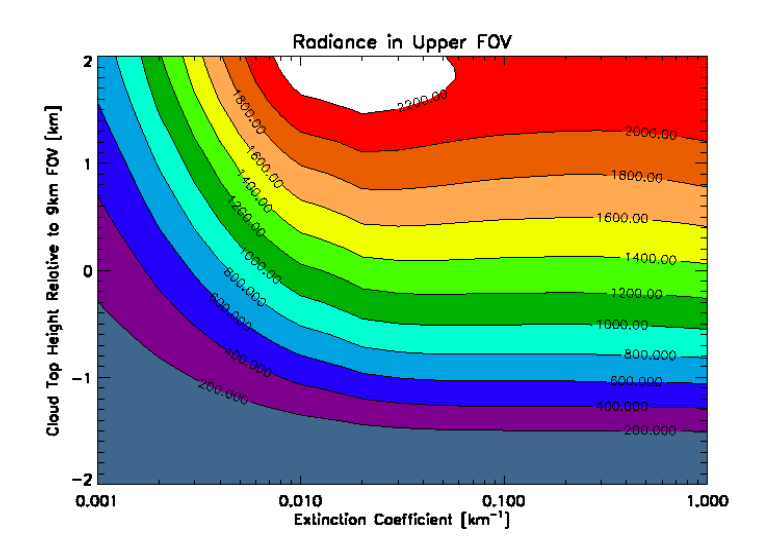


Figure 67: Radiance measured in the upper field-of-view, where cloud is first encountered as a function of relative CTH and of CEX. Here the cloud top is given in kilometers relative to a 9km tangent height.

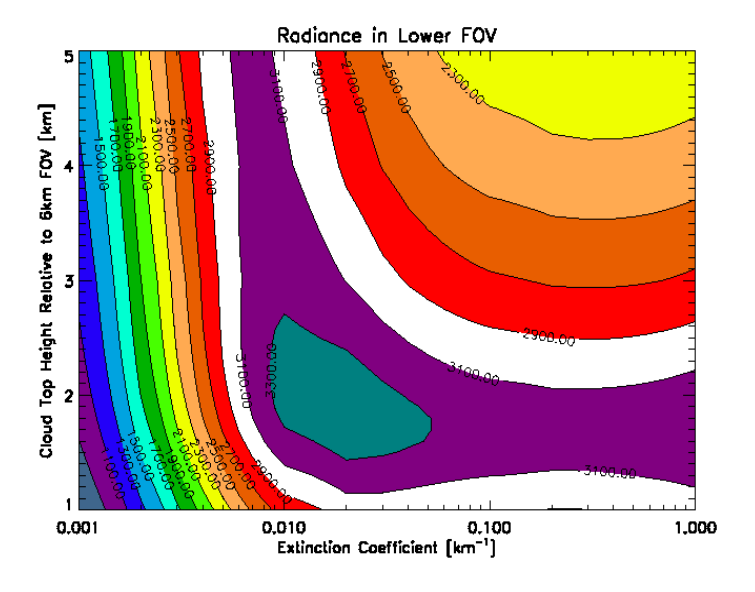


Figure 68: Radiance measured in the lower field-of-view, the sweep immediately below where cloud is first encountered as a function of relative CTH and of CEX . Here the cloud top is given in kilometers relative to a 6km tangent height.

If it is assumed that the cloud is thick (i.e. CEXIX) there is now sufficient information to retrieve both CTH and CTT: the continuum radiance from the lower FOV gives B(CTT) directly which, if compared to the measured radiance from the upper (partially filled) FOV, gives the fraction of the FOV containing the cloud, i.e. the height of the cloud top relative to the nominal tangent height.

5.1.5 Additional Constraints

While thick cloud may indeed be a reasonable assumption for much of the time, the more scientifically interesting cases tend to involve thin clouds (eg cirrus, PSCs) and so a 3 parameter retrieval is required.

For this two additional constraints are provided as a priori information

- 1) The Cloud Effective Fraction (CEF) is known (from the Cloud Index). This constrains the relationship between CEX and CTH, ie a given CEF can be explained by high cloud top within the FOV but thin cloud, or thick cloud but a low cloud top.
- 2) The temperature profile above the cloud is known, eg from climatology or ECMWF data, or the p T retrieval from near real time processing. Using the dry adiabatic lapse rate to describe the temperature profile from this point down to the cloud-top, this constrains the relationship between CTH v CTT.

Note that these are not direct a priori constraints in the traditional sense of being direct estimates of any the retrieval parameters, but constraints on the relationship between pairs of these parameters. As such, these can be represented as additional ('virtual') measurements:

$$y = (R_1, R_2, T_{rtv}, CEF)$$
 $x = (CTH, CTT, CEX)$ $x = Gy$

where

$$G = (K^T S_v^{-1} K)^{-1} K^T S_v^{-1}$$

where K contains the derivatives of $\frac{\phi}{h}$ and S_y is the covariance matrix for y.

5.1.6 Implementation

While there are theoretically enough constraints for a simple least-squares fit type of retrieval, this does not work too well in practice due to the non-linearity of the problem.

After some experimentation the following two-step approach has been found to be more robust

Step 1:

a = initial guess of x, S_a = large a priori covariance

$$y = (T_{rtv}, CEF)$$

 x', S_x = optimal estimation retrieval using a, y, S_y

Step 2:

a = x', $S_a = S_{x'}$ from Step 1

$$y = (R_1, R_2)$$

 x_{s,S_x} = optimal estimation using a,y,S_y

Further, the initial guess used for a in step 1 depends on CEF, with different assumptions for CEX depending on whether CEF > 0.2 or CEF < 0.2. The currently implemented scheme is shown in Figure 69.

Figure 69: Schematic of sequential retrieval scheme. The preliminary retrieval uses the retrieved temperature of the cloudy FOV and effective fraction as pseudo-measurements to estimate the state vector. The main retrieval uses the radiance measurements from the first FOV flagged as cloudy and those of the FOV immediately below.

5.1.7 Results with simulated data

Figure 70 shows the results of tests with simulated data.

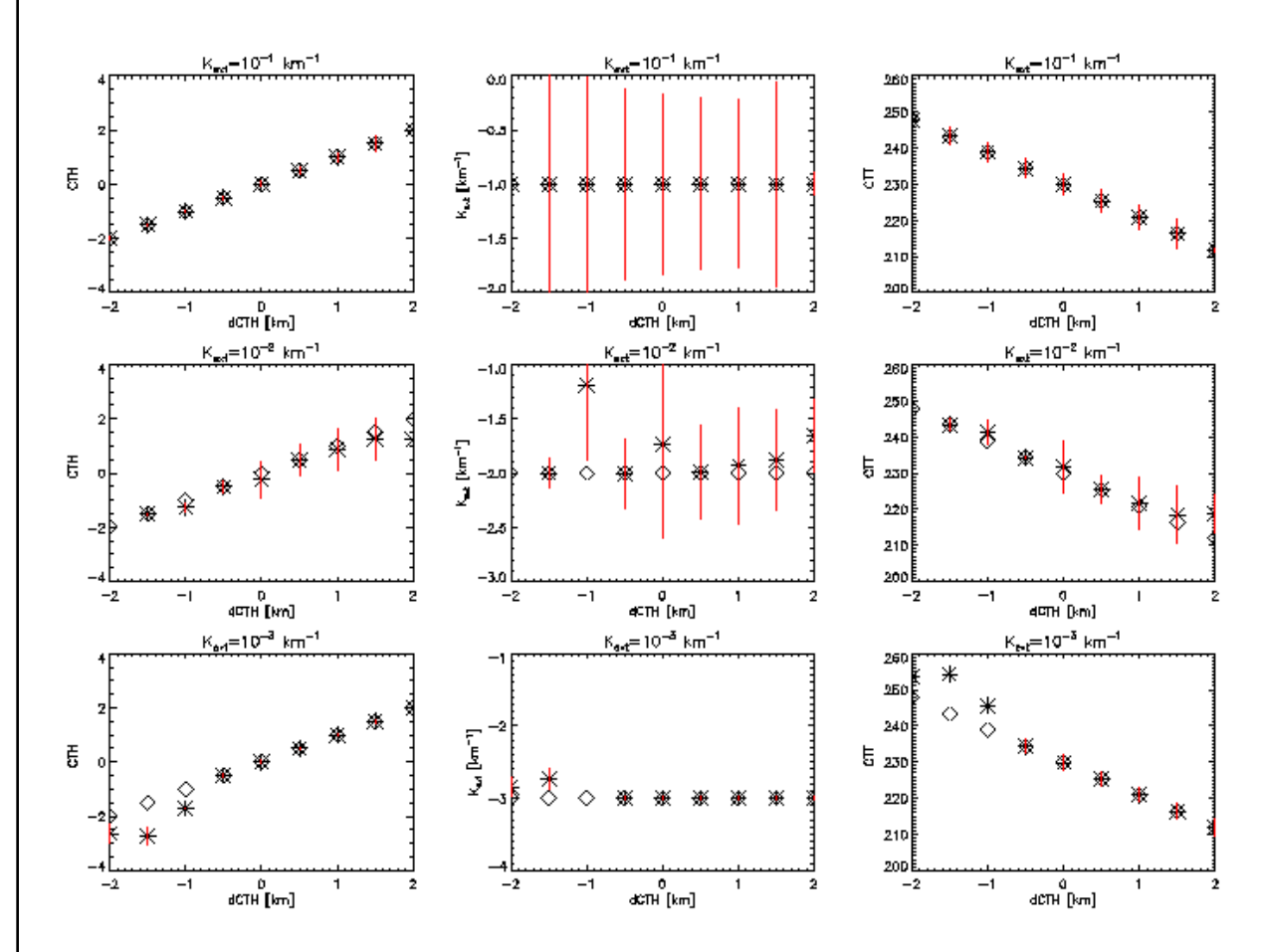
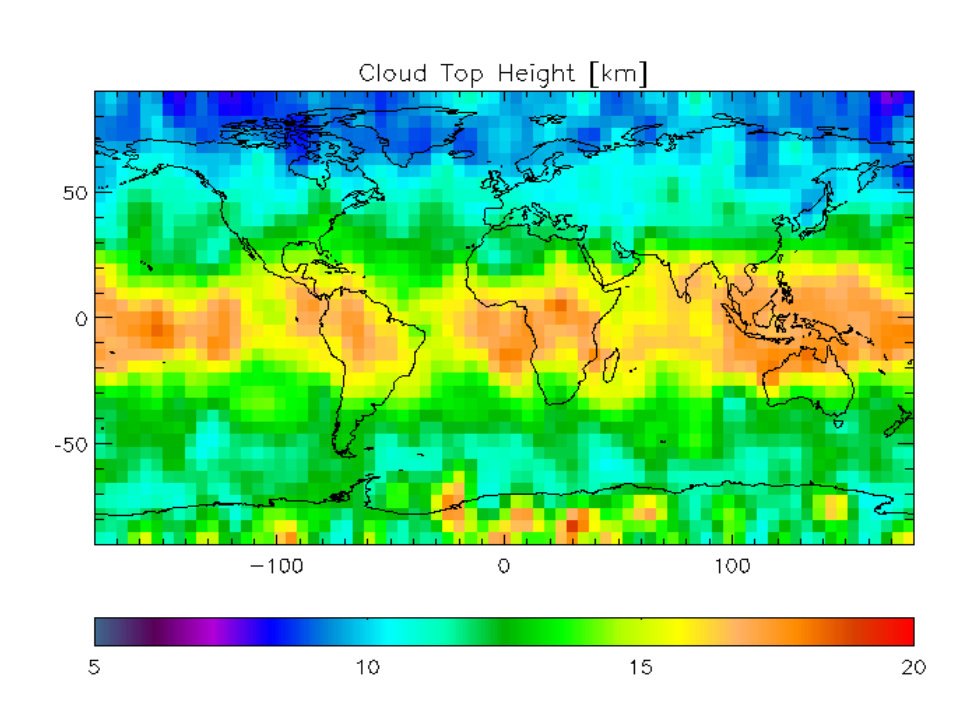


Figure 70: Results of sequential retrieval applied to RFM simulated data, showing 'true' (diamonds) and retrieved (asterisks plus red error bars) values for the three parameters (vertical axis) as a function of position of cloud top relative to center of the FOV (horizontal axis) and different $\log(k_{\rm ext})$, (different rows of plots - thick cloud in top row, thin cloud in bottom row)

5.1.8 Results with real data

The above algorithm has been used to process 1 day in 10 of MIPAS L1B spectra acquired throughout 2003. Annual averages of the retrieved quantities are shown in Figures 71-73. In all cases these are the averages of just the cases where a cloud-top has been identified within the 9 km or higher sweep.



Technical Note:

Figure 71: Annual average of Cloud Top Height during 2003

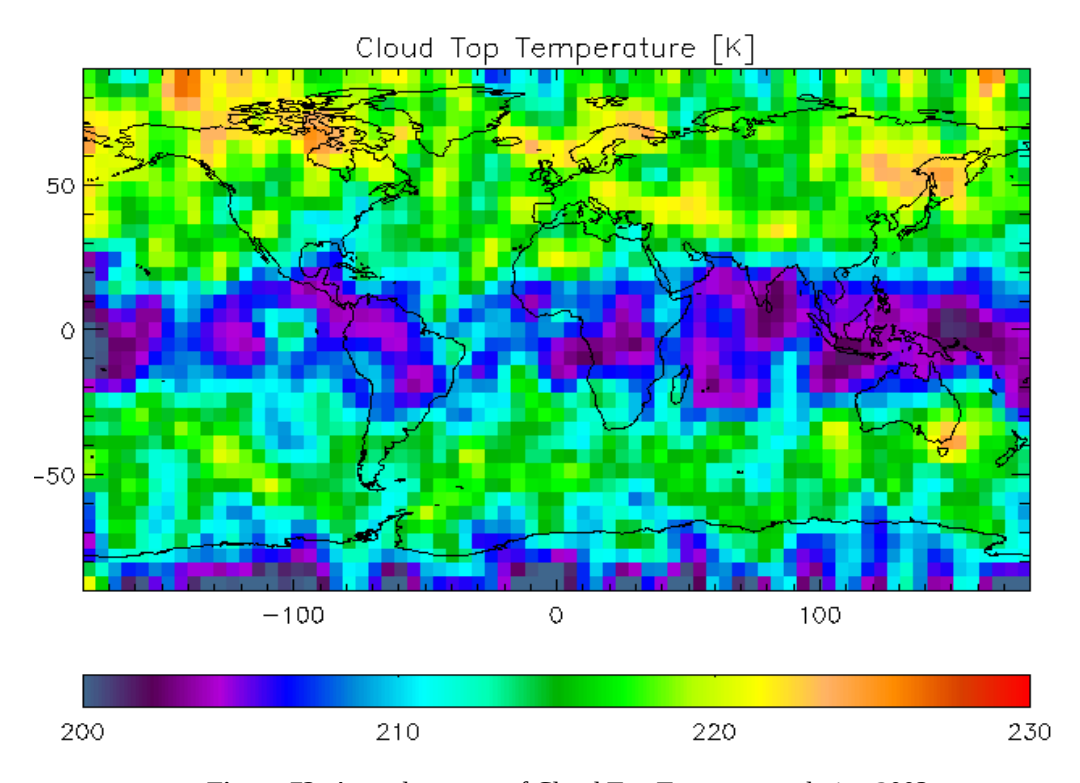


Figure 72: Annual average of Cloud Top Temperature during 2003

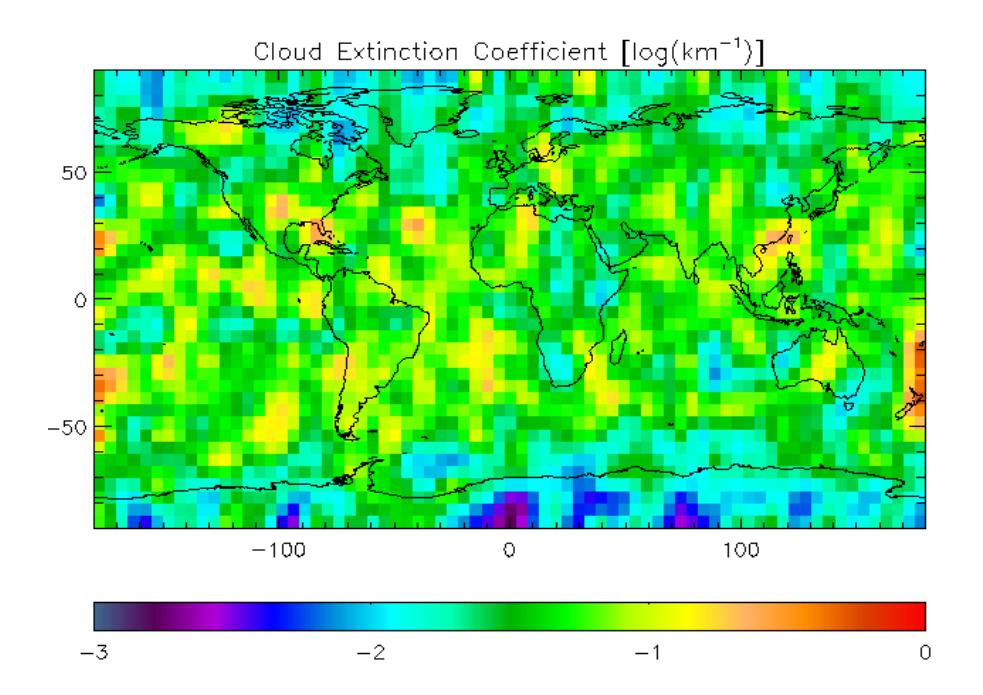


Figure 73: Annual average of Cloud Extinction during 2003

5.2 Microphysical Parameter

5.2.1 Theoretical retrieval limit for microphysical cloud parameters

In this section, on basis of the CSDB, it is investigated which information on microphysical cloud size distribution parameters could be obtained for PSCs and cirrus in the optimum case that the only error source would be the spectral noise of MIPAS. Other atmospheric parameters, like temperature and trace-gas profiles, are assumed to be known exactly. The simultaneous retrieval of different distribution parameters is tested. Further, the effect of using a limited set of spectral ranges compared to the whole spectral range of the CSDB is addressed.

Approach:

To determine the retrieval error from each single simulated tangent altitude measurement, linear error estimation has been applied:

$$S_{x} = (K^{T} S_{v}^{-1} K)^{-1}$$

where S_x is the covariance matrix of the microphysical parameters, K the Jacobian matrix from the CSDB and S_y the spectral noise error covariance for which the nominal MIPAS values have been used.

As target parameters for PSCs the volume density V, the mean radius R and the width W have been chosen. In case of cirrus the ice water content IWC and the effective radius Reff have been investigated.

The theoretical errors have been calculated for the whole CSDB wavenumber range (see description of the database) and for the following selected microwindows:

- 824-831 cm⁻¹
- 940-950 cm⁻¹
- 1224-1227 cm⁻¹.

For analysis, the resulting errors have been plotted against the integrated volume densities along the line-of-sight (denoted as 'volume column density' [μm^3 cm⁻²]) for PSCs and against the ice water path (IWP) divided by the effective radius (Reff) [g m⁻² μm^{-1}] in case of cirrus clouds. This has shown the provide much more compact relationships for different particle sizes than the a plots against volume density, ice water content or surface density, especially for estimation of the optically thick limit of the limb view as a limit for retrieveability of microphysical parameters.

The following conversion factors may be helpful in the following:

Volume densities: $1 \mu m^3 cm^{-3} = 9.2 \times 10^{-7} g m^{-3}$ (ice)

10 ppmv H2O @ 100 hPa $\approx 10^{-3}$ g m⁻³ (ice)

Ice water path: 100 g m^{-2} corresponds to $5 \times 10^{-4} \text{ g m}^{-3}$ over a limb path of 200 km

5.2.2 PSC Results

Figures 74-76 show the estimates of the relative error for volume density (Fig. 74), mean radius (Fig. 75) and distribution width (Fig. 76) versus the integrated volume density along the line-of-sight. Colors indicate the different particle sizes. The left columns contain the error estimates in case the whole wavenumber range chosen for the CSDB is used. The right columns are the results when instead of the whole range, only the three microwindows as defined above are used. The three rows in each Figure show STS (top), NAT (middle) and ice (bottom), where for STS the composition 25wt-% H2SO4/25wt-% HNO3 has been chosen since the two other STS compositions included in the CSDB exhibit very similar results to the ones shown here.

The following major points can be deduced:

- The most prominent feature in all plots is the continuous decrease of the relative errors with increasing slant column densities until a minimum is reached at volume column densities of $10^8 10^9 \, \mu m^3 \, cm^{-2}$ (equivalent to slant ice water paths of $0.92 9.2 \, g \, m^{-2}$). For higher densities, the errors begin to increase and to scatter more strongly. While the decreasing errors are due to the better signal-to-noise ratio for larger column densities, the turning point is a consequence of the limb-path becoming optically thick. For the largest ice particles (10 μm , red dots) the error increase starts at larger values of slant column density since the limb optical depth becomes more dominated by the surface density for the larger particle sizes, while for smaller ones it is dominated by the volume density.
- In most cases there is a large increase of errors between the 1-parameter and the 3- parameter fit (factor of 10 up to >100). This is more pronounced for the small particle modes since in these cases for absorbing particles, only the total volume density determines the extinction and there is no sensitivity on particle size (e.g. errors >>1000% for smallest STS particles.
- The increase of errors between the 'whole spectral range' and the '3 mw' retrieval is with a factor of around 5 relatively moderate. This is important since it indicates that for the processing scheme the wavenumber range can be restricted to those regions where there is least interference with spectral signatures of gaseous species.

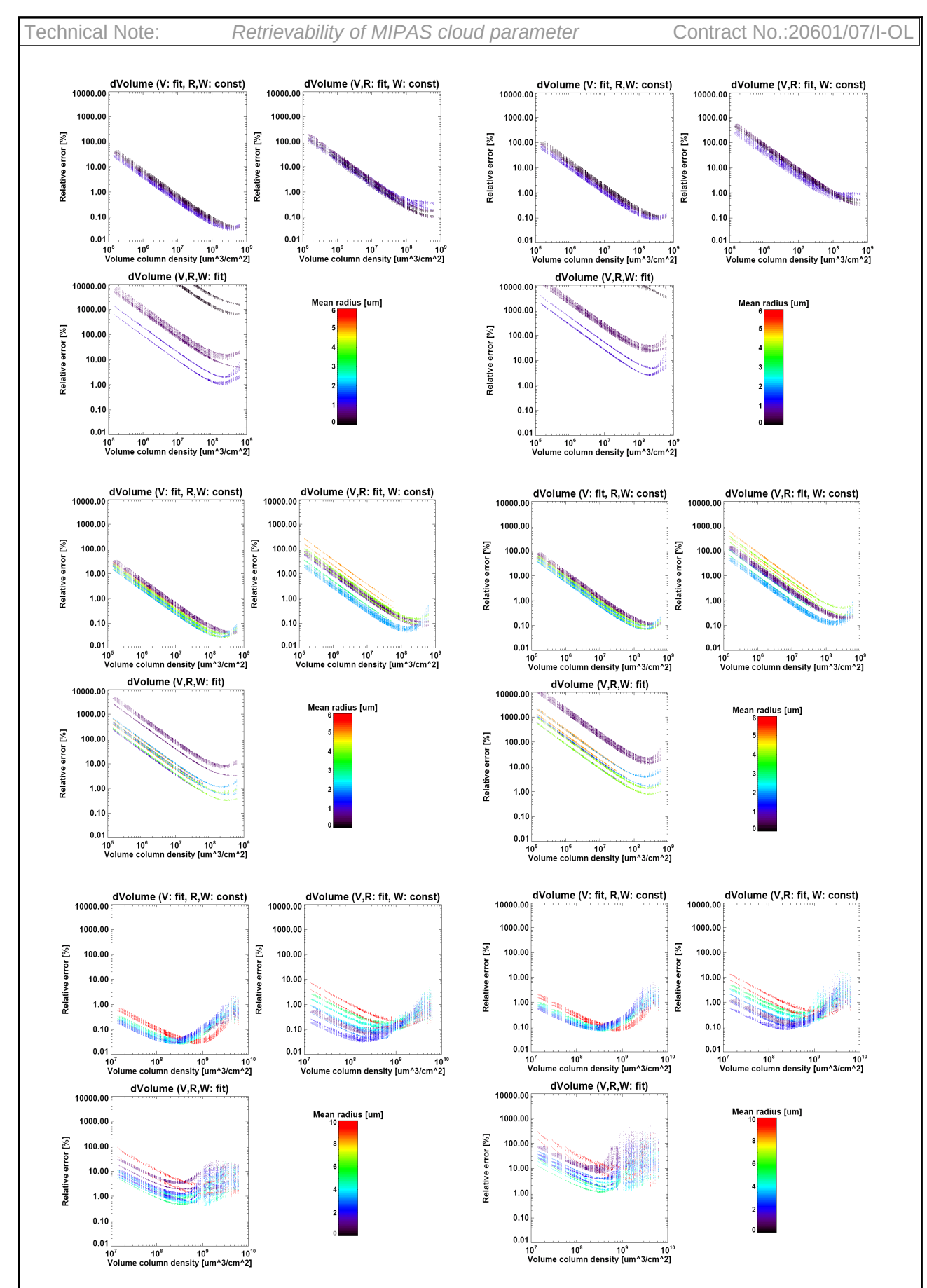


Figure 74: Error estimation for volume density retrieval versus slant path volume column desity. Top: STS (25wt-% H2SO4, 25wt-% HNO3), middle: NAT, bottom: ice. Left column: whole simulated spectral range, right column: 3 selected windows.

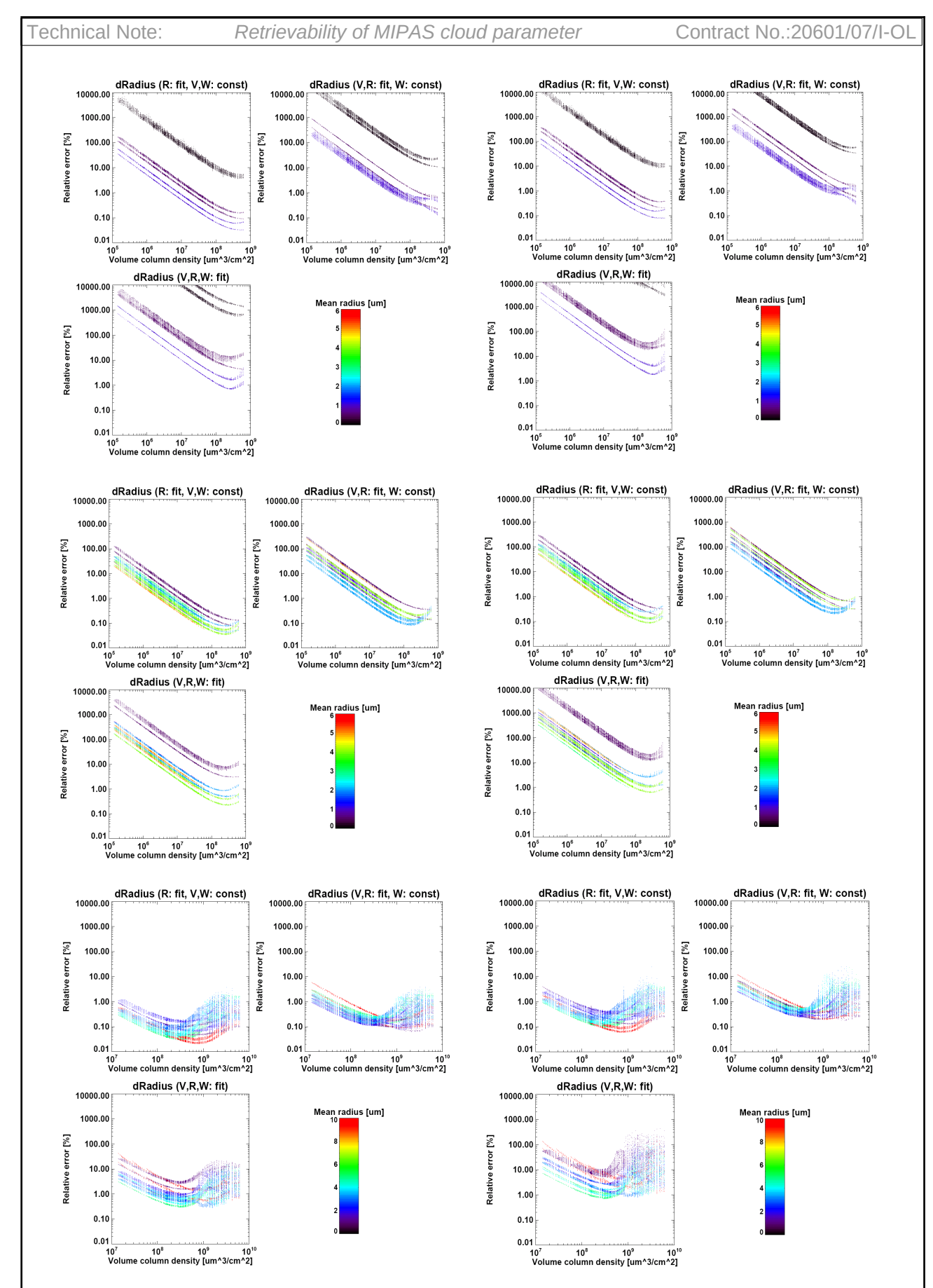


Figure 75: Error estimation for mean radius retrieval versus slant path volume column desity. Top: STS (25wt-% H2SO4, 25wt-% HNO3), middle: NAT, bottom: ice. Left column: whole simulated spectral range, right column: 3 selected windows.

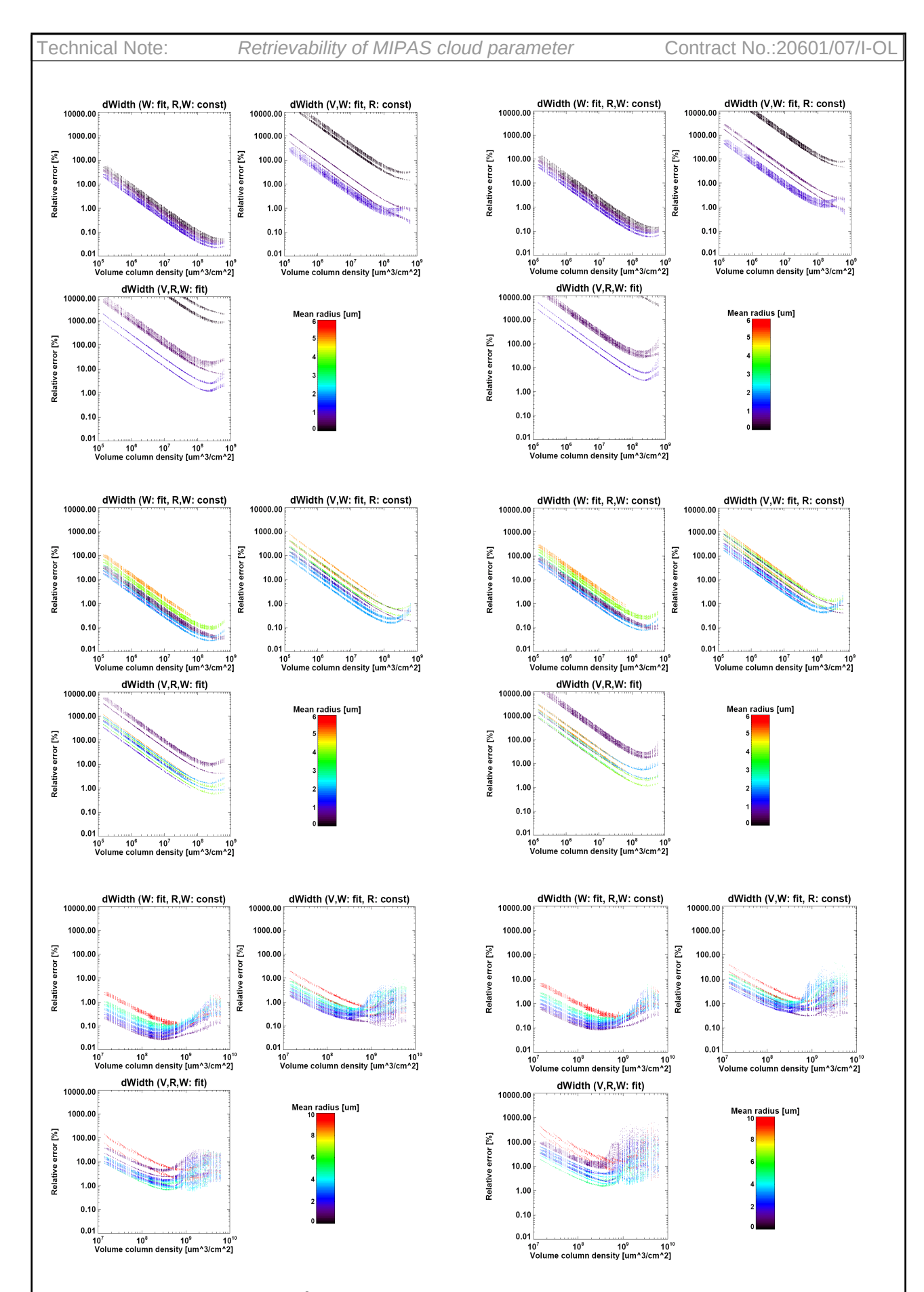


Figure 76: Error estimation for distribution width retrieval versus slant path volume column desity. Top: STS (25wt-% H2SO4, 25wt-% HNO3), middle: NAT, bottom: ice. Left column: whole simulated spectral range, right column: 3 selected windows.

5.2.3 Cirrus Results

Figures 77-80 show results of the linear error estimation from the polar summer, the mid-latitude and the tropical cirrus CSDBs. The relative errors of ice water content (top) and effective radius (bottom) are given as a function of the slant ice water column amount (IWP) (Fig. 77) or ice water surface column amount IWP/Reff (Figs. 78-80) along the limb line-of-sight and of the effective radius (color-coded).

As in case of the PSC database, the left columns correspond to the whole-spectral range (of the CSDB) and the right column to the three spectral windows as defined above. Within each panel the errors are plotted for a one-parameter fit (IWC or Reff), for a two-parameter fit (IWC and Reff, H2O=const) and a three-parameter fit (IWC, Reff and H2O), where H2O is the mean volume mixing ratio at the altitude range where the cirrus cloud is located.

Major findings:

- The comparison between Fig. 77 and Fig. 78 shows that for the particle sizes of cirrus clouds the error distributions are much more compact when plotted against IWP/Reff than against IWP. This is due to the larger particle sizes compared to the small-particle PSC cases. This is already visible for the 10 µm particles in the ice-PSC simulations.
- Like in the case of PSCs, the relative errors first decrease with increasing slant IWP/Reff (or IWP) but start to rise at values around 1 g m⁻² μ m⁻¹ (10 g m⁻²) when the cloud becomes opaque in limb geometry.
- In general, the errors increase by a factor of ~ 10 when a simultaneous fit of IWC and Reff is performed compared to a single parameter fit.
- There is nearly no increase estimated errors in the cloud parameters when water vapor is added as a third retrieval quantity indicating that the H2O spectral features are independent from the effects of clouds on the spectrum.

5.2.4 Conclusions

The linear error analysis of PSC/cirrus microphysical parameter retrieval shows that theoretically there is sufficient information in MIPAS spectra to derive cloud volume density and size information provided that the cloud is not too optically thick in limb. Upper limits are slant volume column densities of $10^8 - 10^9 \, \mu m^3 \, cm^{-2}$ for PSCs and an ice water surface path of 1 g m⁻² μm^{-1} for cirrus clouds. The possibility to retrieve different quantities is tied to the size of the particles: for very small PSC particles (of STS) there is only information on the total volume density. For larger PSC particles information on volume and radius is present, but to derive the distribution width seems not possible (large errors in 3-parameter retrieval) in most of the cases. In case of cirrus, sufficient information to derive IWC and effective radius seems feasible even in case of varying H2O abundances.

However, these calculations have been performed on basis of idealized conditions, namely (a) the clouds are horizontally homogeneous, (b) all other atmospheric constituents and temperature including the scene below the tangent point (i.e. the surface temperature and lower atmospheric conditions) are known, (c) the shape of the particle size distribution and particle habits/phase/composition are known and the microphysical properties of the cloud are homogeneous in the vertical.

Regarding the intended retrieval of cloud properties from MIPAS:

- (a) is mostly not the case for real clouds, however, in case of the optically thin and, thus, interesting cloud cases (tropical subvisual high cirrus clouds, PSC-cover of the Antarctic) it might be a good approximation. Thus, in general, a concentration-type of cloud property (like volume density, ice water content or surface density) cannot be derived, but rather the slant path column densities of these quantities which could then, using the assumption of horizontal homogeneity be translated into concentrations.
- (b) to minimize the errors due to interfering trace gases, selected microwindows are to be used. That the loss of information by application of small windows instead of the whole range is limited has been shown quantitatively by these calculations (increase of errors by about a factor of 5). Note that although the spectral coverage by the 3 selected windows is much smaller than the whole range of MIPAS, a retrieval of multiple parameters is still feasible.
- (c) The calculations in case of PSCs show that a simultaneous retrieval of three parameters (V, R, and W) is, even under the idealized conditions applied, problematic. Thus, some assumption has to be made on the particle size distribution, like a fixed width of the size distribution or the use of averaged typical single scattering properties as those applied for the construction of the cirrus CSDB.

In cond	clusion,	for the	inten	ded	proces	ssing s	scheme,	the	derivation	n of two	parai	mete	rs sho	ould	be
further	investig	gated: c	ne on	the	slant	colum	ın surfa	ce o	r volume	densities	and	the	other	on	the
particle	sizes.														

Figure 77: Tropical cirrus database: error estimation for ice water content as function of slant ice water path (IWP): top and for effective radius (Reff): bottom. Left column: whole spectral range of CSDB, right column: 3 selected windows.

10⁰ 10² 10⁴ IWP [g/m^2]

10⁰ 10² 10⁴ IWP [g/m^2]

Figure 78: Tropical cirrus database: like Fig. 78 but with changed x-axis, IWP/Reff, resulting in more compact relationships. Left column: whole spectral range of CSDB, right column: 3 selected windows.

Figure 79: Like Fig. 78 but for the mid-latitude cirrus database.

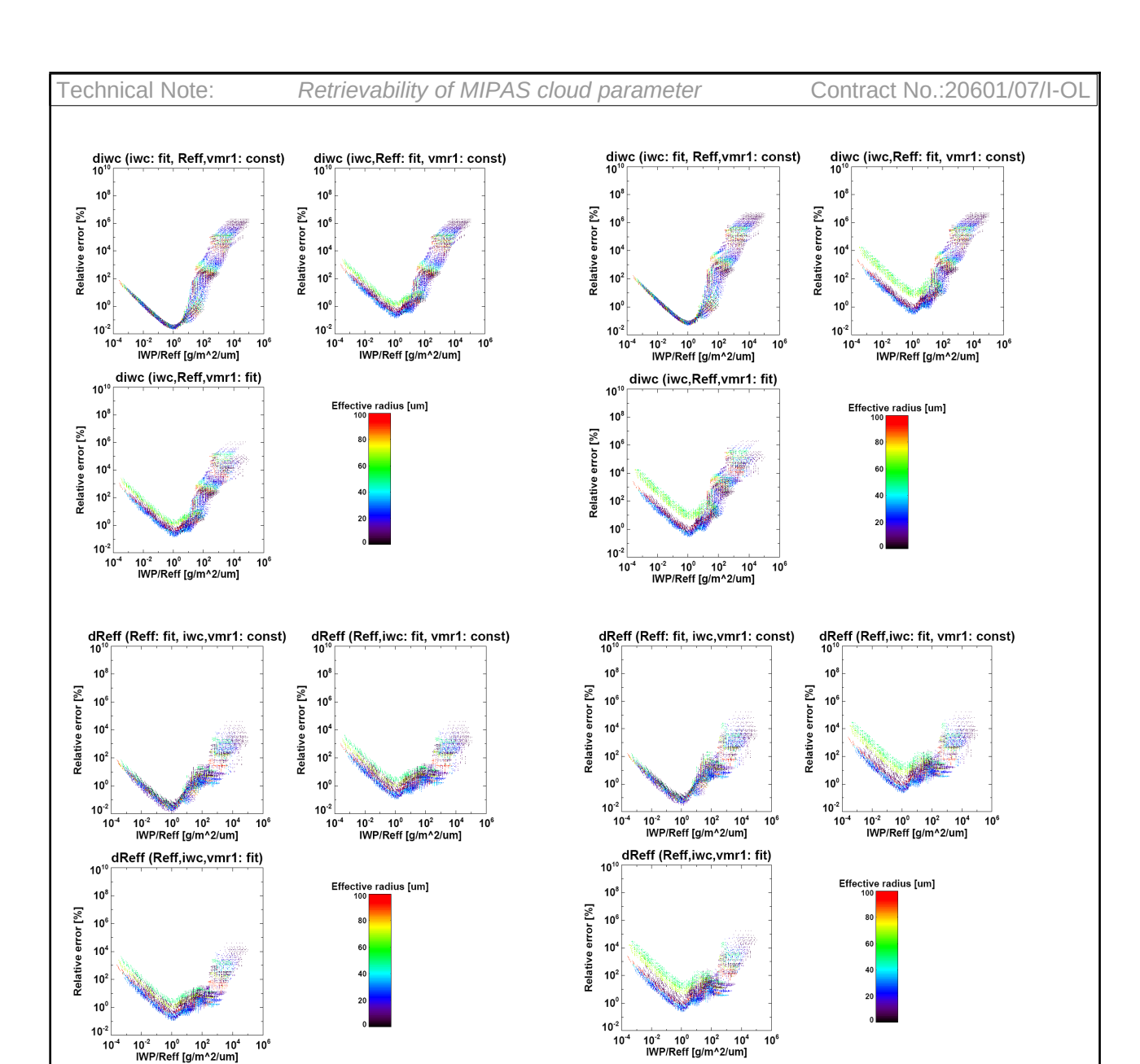


Figure 80: Like Fig. 78 but for the polar summer cirrus database.

5.2.5 An Estimate for slant IWP, IWC, Area Density and Volume Density Path

Various parameters from the CSDB spectra have been tested to extract simple and robust microphysical information form the measured spectra without radiative transfer calculations. For example the well established cloud index shows a quite fair correlation with the integrated Limb ice water path (IWP), like illustrated in Fig. 81(a). But IWP is based on the volume density of the particles, where the area density (e.g. for PSD for spherical particle A = 3V/Reff) integrated along the limb path should represent better the radiative properties of the cloud column. Here and already above this quantity is called area density path (ADP). The closer link between ADP and the CI-CR is already indicated in Fig. 81 by the color-coded radius dependence, and is even better to see in the compact correlation between CI versus IWP divided by the effective radius (Re) of Fig. 81(b). It looks reasonable that IWP/Re or ADP can be estimated from the simple color ratio for optically thin conditions (1.2<CI<~5). For optical thick conditions a lower limit for ADP seems assessable.

If you assume a homogeneous cloud layer along the limb path restricted to the TH layer – a simplified cloud geometry – then it is possible to compute the IWC by simple geometry parameters. Parameterisations like Donovan (2003) would then allow to estimate Reff based on the

CTT and IWC. Further tests and analyses are necessary to investigate how good the simple approach can work.

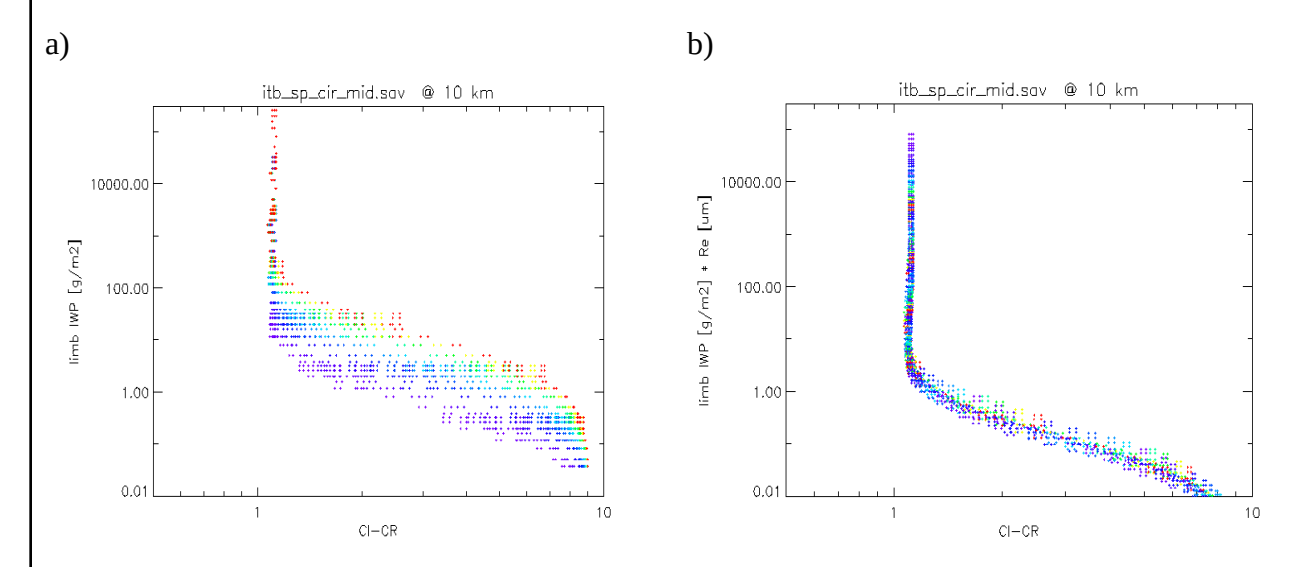


Figure 81: Standard cloud index color ratio for MIPAS band A versus limb Ice Water Path (IWP), the integrated IWC along the line of sight for the mid-latitude cirrus spectra of the CSDB at 10 km altitude. All different cloud scenarios and geometries are included. Color coded is the effective radius dependence, with largest radii in red and smallest in blue. **(b)** like (a) but CI-CR versus IWP divided by the effective radius of the particle size distribution.

The question if ADP and CI-CR follow a compact correlation is unfortunately not the case for all possible scenarios. Putting all scenarios for the tropical cirrus together (Figure 82) the scatter is mainly caused by the variability by the different tangent heights (a). Whereby, the different climatology profiles (latitudes) have no big impact on the variability, like shown in Figure 82 (b) for a fixed TH of 9 km.

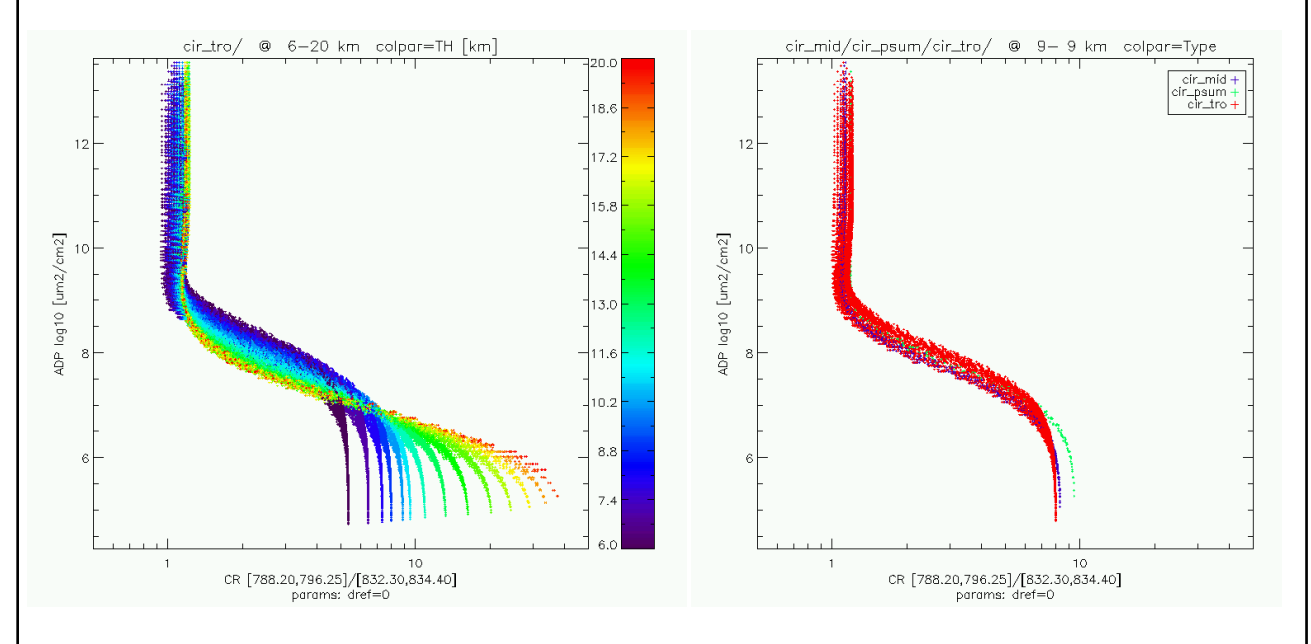


Figure 82: CI-CR versus ADP for (a) tropical cirrus scenarios between 6 and 20 km altitude and (b) three latitude regions at 9 km tangent height.

It looks reasonable, that a CI-CR threshold value for optically thick conditions (CI \sim 1.2) can refer to a fixed lower limit of ADP. In the example above ADP > 10^9 um2/cm2 is related at all altitudes

to optically thick conditions (but keep in mind the H2O continuum problem at altitudes below 8 km).

5.2.6 Particle size by use of brightness temperature difference correlations

<u>Approach:</u>

On basis of the CSDB here we test the possibility to derive information on cirrus particle size by use of correlations between different spectral windows. Especially brightness temperature differences are investigated since a variety of cloud detection/specification algorithms for nadir sounding instruments rely on such differences.

The following windows with minor trace gas interferences but covering a wide spectral range are used:

'827': 827.075±0.5 cm⁻¹
 '941': 941.525±0.5 cm⁻¹
 '1227': 1227.40±0.5 cm⁻¹
 '1972': 1972.57±0.5 cm⁻¹

Results:

Figures 83-91 show correlations between various brightness temperature (BT) differences versus the BT827-BT941 for three atmospheric cirrus cloud situations. The plots further differ by neglect or application of convolution of the pencil beam radiances with the field-of-view (FOV) of MIPAS, by the number of tangent altitudes used (all vs. only the highest ones near the cloud-top) and by the selected cloud index (CI) range. In all plots the particle effective radius is colour-coded varying from black (4.0 μ m) to red (90 μ m).

Figure 83(tropical cirrus, CI=1.4-5.0, no FOV convolution, all cloud-affected tangent altitudes): a separation of different particle sizes appears through the 'rainbow' like split of a majority of the scattered points, mainly with increasing particle sizes from right to left, i.e. from larger to smaller BT827-BT941 differences. However, this separation is not complete since there are some cases where small and large particles occupy the same region of the scatterplots.

This separation appears to be nearly complete when only the top cloud-affected spectra of a limb-scan are used as shown in Figure 84 (tropical cirrus, CI=1.4-5.0, no FOV convolution, only highest two cloud-affected tangent altitudes).

However, the preceding two examples show only an idealized case for an instrument with infinitesimal small vertical field-of-view extent. Fig. 85, in contrast shows the same correlations as in Fig. 84, but with the realistic FOV of MIPAS applied. In that case, the separation of particle sizes appears again blurred, especially for BT827-BT941 differences between 10 and 20 K. However, at larger BT827-BT941 differences, a smaller particle regime exists.

In Figs. 86 and 87 we've tested the effect of different lower cloud index boundarys. For Fig. 86 a CI-range of 1.2-5.0 has been used (i.e. optically thicker clouds included) while for Fig. 87 a CI-range of 1.8-5.0 only the BT differences of optically thinner clouds are plotted. While there is not much difference between the correlations for a lower CI limit of 1.4 and 1.2, in case of a CI limit of 1.8 (Fig. 87) the separations looks much better. However, still at values of BT827-BT941 around 10 K there is some mixing between large and small particles.

Figures 88 and 89 compare the two CI-limit ranges (Fig. 88: 1.4-5.0, Fig. 89: 1.8-5.0) in case of mid-latitude and Figs. 90 and 91 (90: 1.4-5.0, 91: 1.8-5.0) those for the polar summer atmospheres. Like for the tropical cirrus simulations, the separation between different particle sizes becomes in both cases clearer when a lower CI limit of 1.8 is applied. (With the exception of some intermixing in the polar summer case at BT827-BT941 \approx 10 - 20 K and BT827-BT1227 \approx 32 K).

Technical Note:	Retrievability of MIPAS cloud parameter	Contract No.:20601/07/I-OL
Conclusions:		
cm ⁻¹ and 941 cm ⁻¹ smaller particles the	ce absorption peak within channel A of MIPAS appear to be an adequate measure to separate e BT difference becomes smaller since the ice d be reached by application of the following sel	different cirrus size ranges. For absorption is stronger. Various
	cloud-affected limb views of each limb scan ar criterium on optically thin clouds is applied by s	
	iteria restrict the range of cloud observations fee made. However, they seem to be necessary	

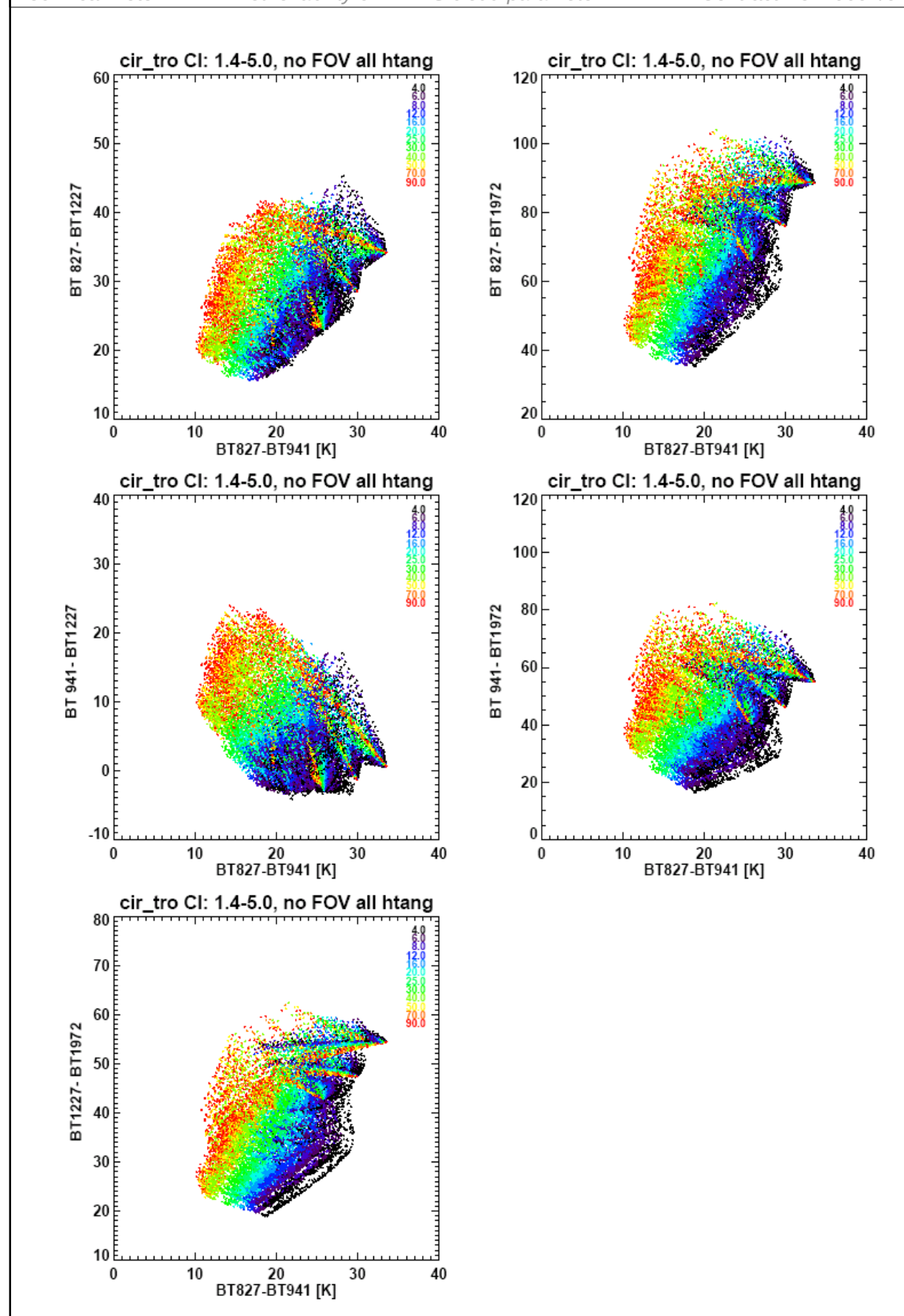


Figure 83: Tropical cirrus: correlation of brightness temperature differences between different spectral windows. Selection: CI-range: 1.4-5.0, no FOV convolution, all cloud-affected tangent altitudes. The color scale indicates the particle effective radius from 4.0 μm (black) to 90 μm (red).

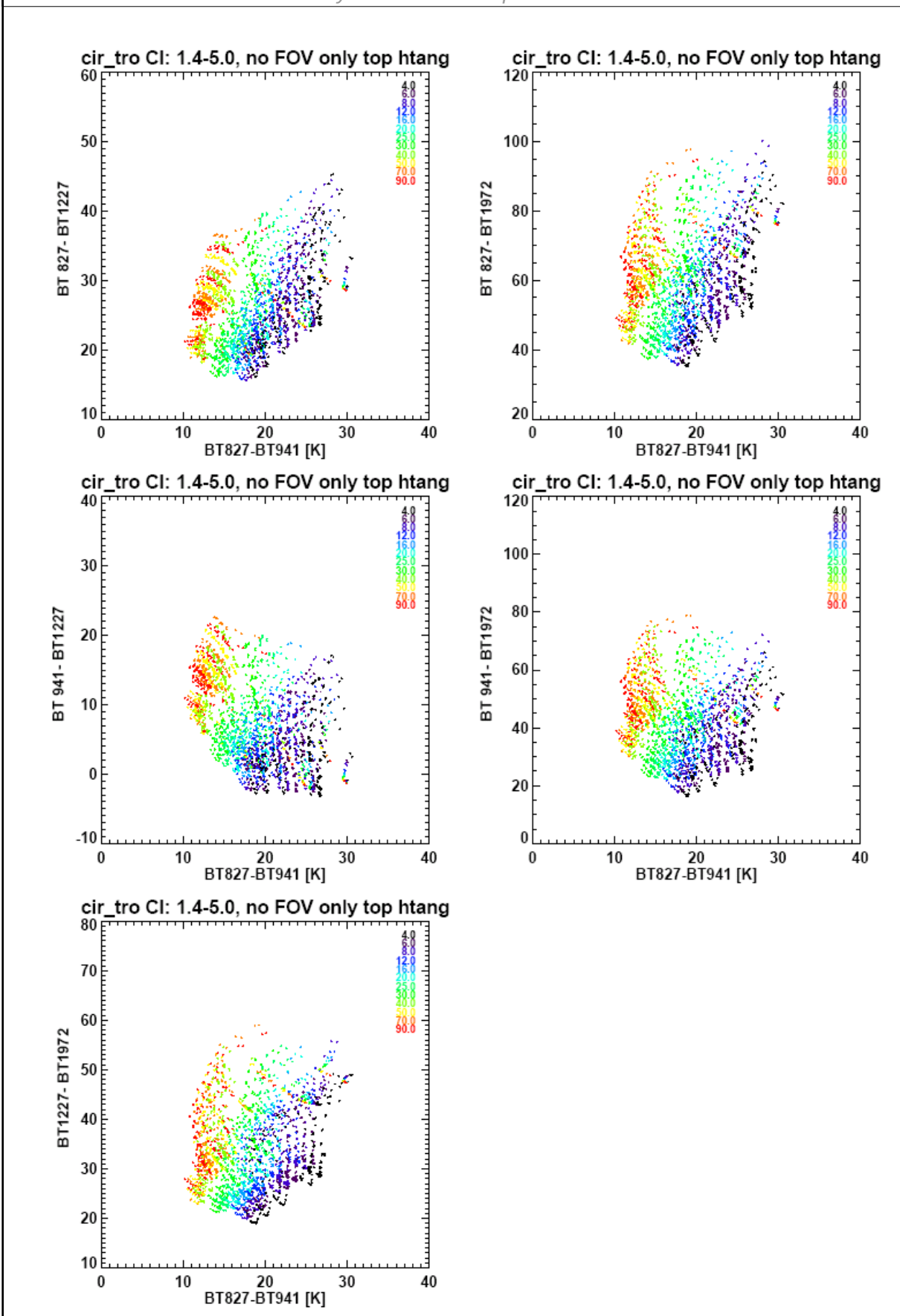


Figure 84: Like Fig. 83, but only with highest cloud-affected tangent altitudes. (Tropical cirrus: correlation of brightness temperature differences between different spectral windows. Selection: CIrange: 1.4-5.0, no FOV convolution, only highest-two cloud-affected tangent altitudes.)

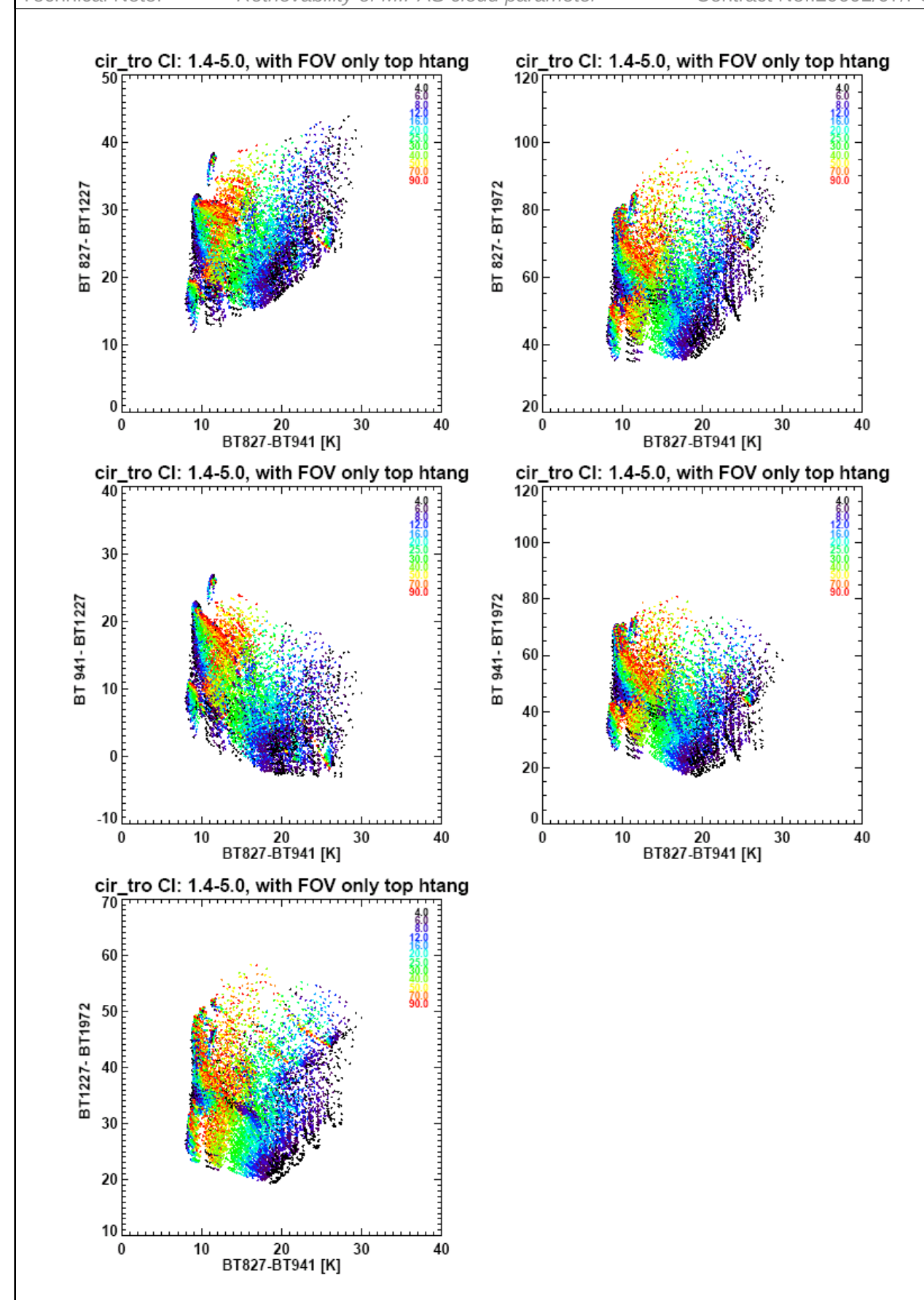


Figure 85: Like Fig. 84 but with FOV convolution. (Tropical cirrus: correlation of brightness temperature differences between different spectral windows. Selection: CI-range: 1.4-5.0, with FOV convolution, only highest-two cloud-affected tangent altitudes.)

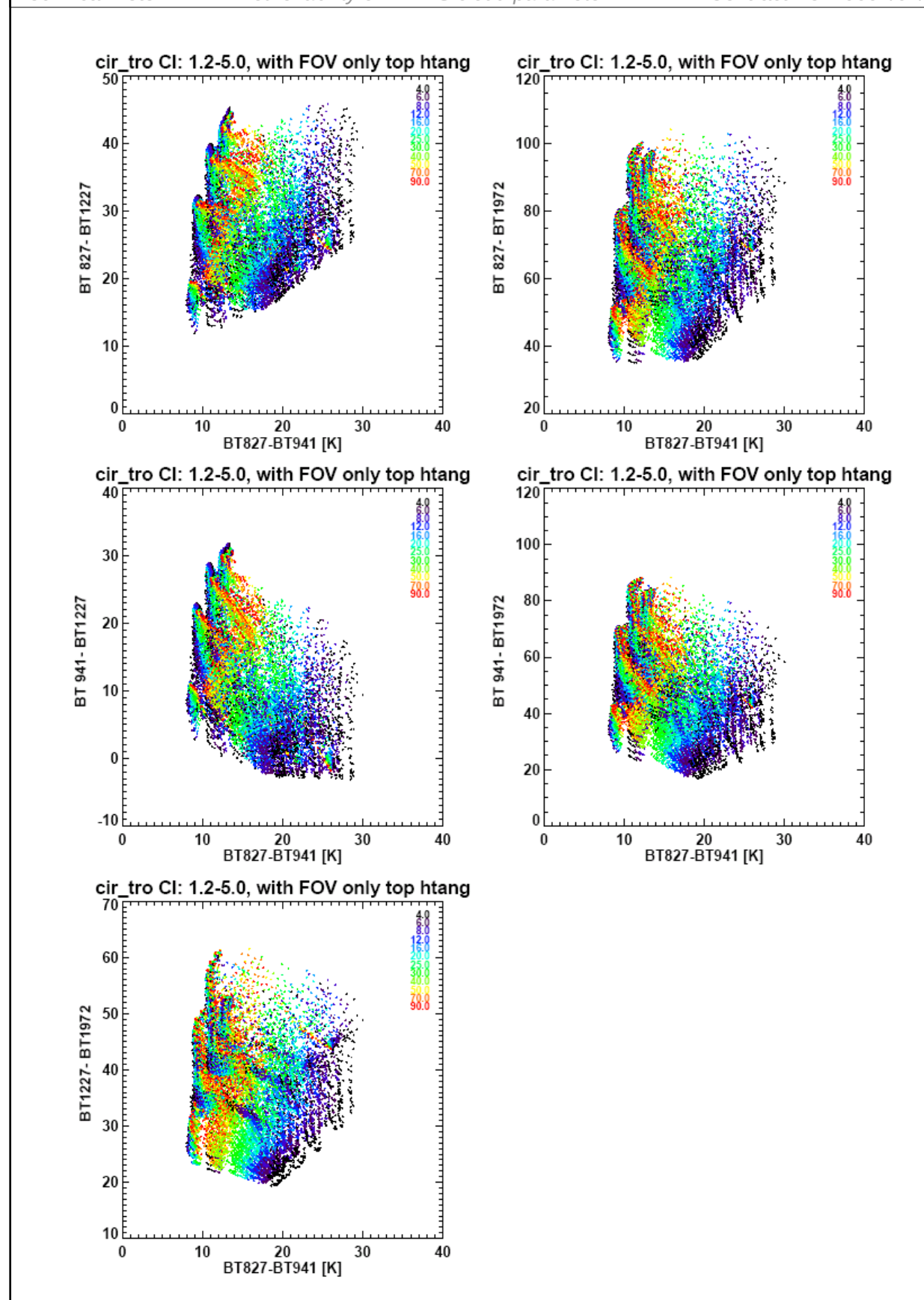


Figure 86: Like Fig. 86 and Fig. 85 but for CI-range 1.2-5.0 (Tropical cirrus: correlation of brightness temperature differences between different spectral windows. Selection: CI-range: 1.2-5.0, with FOV convolution, only highest-two cloud-affected tangent altitudes.)

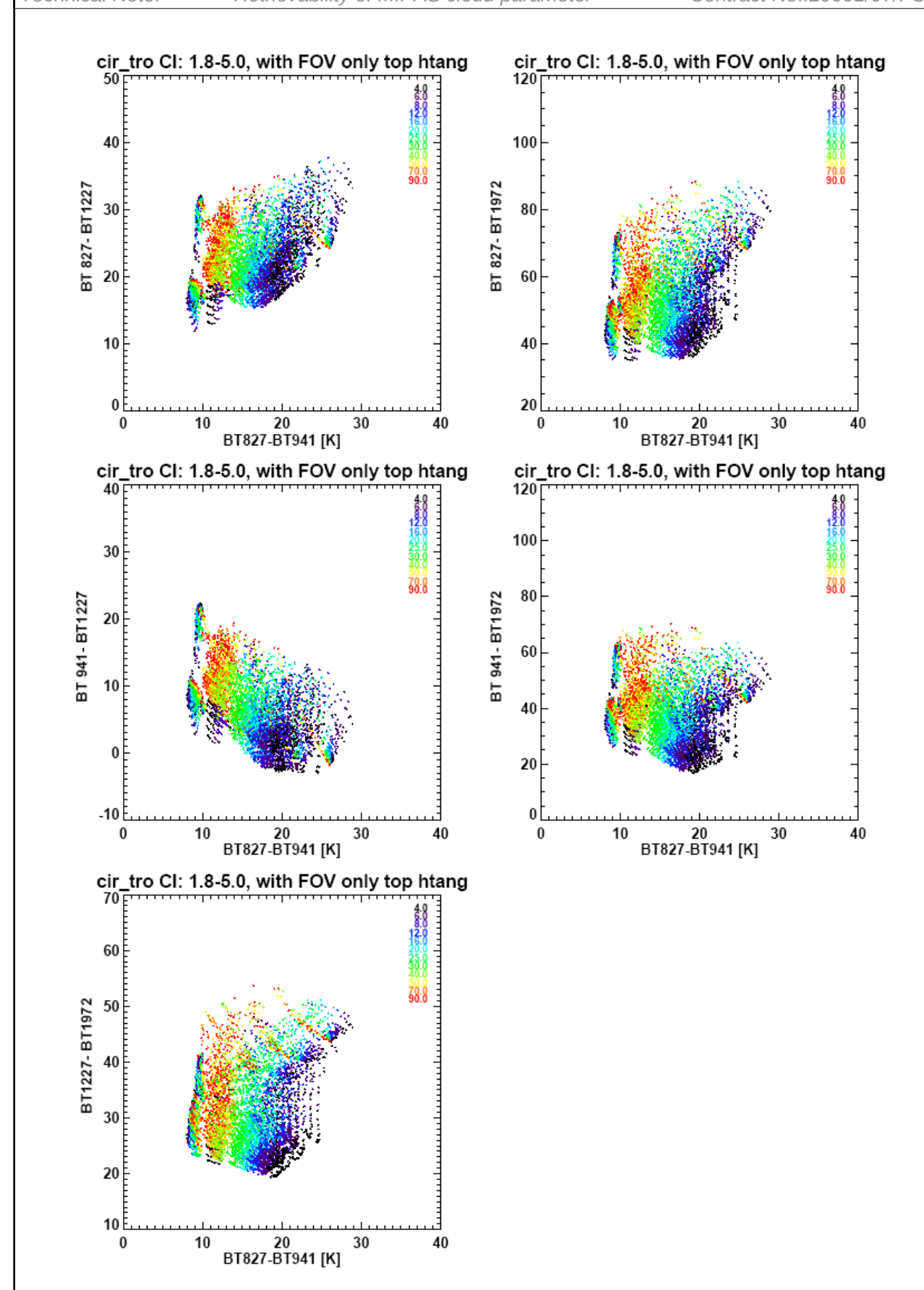


Figure 87: Like Fig. 85 but for CI-range 1.8-5.0 (Tropical cirrus: correlation of brightness temperature differences between different spectral windows. Selection: CI-range: 1.8-5.0, with FOV convolution, only highest-two cloud-affected tangent altitudes.)

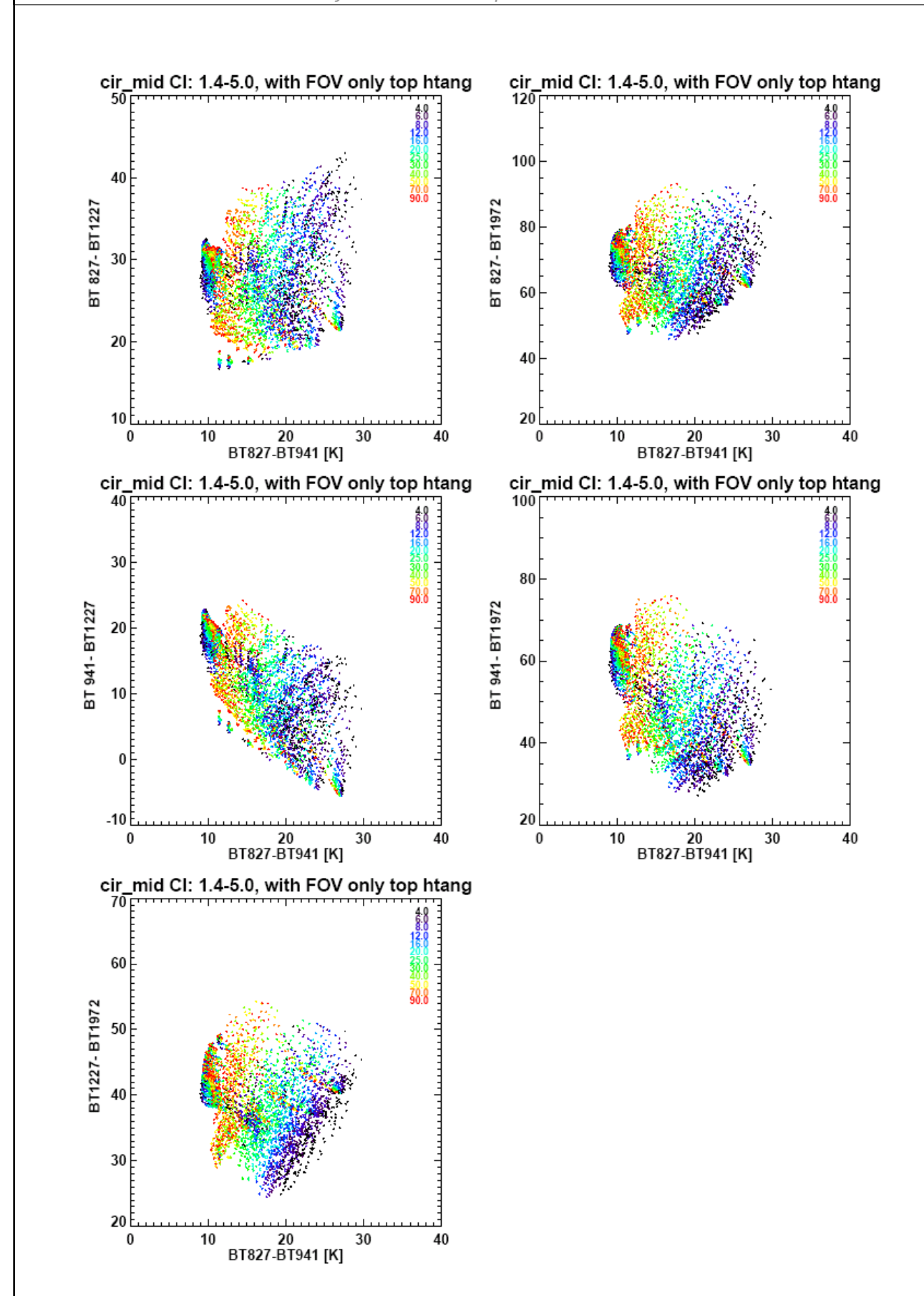


Figure 88: Like Fig. 85 but for mid-latitude cirrus (Mid-latitude cirrus: correlation of brightness temperature differences between different spectral windows. Selection: CI-range: 1.4-5.0, with FOV convolution, only highest-two cloud-affected tangent altitudes.)

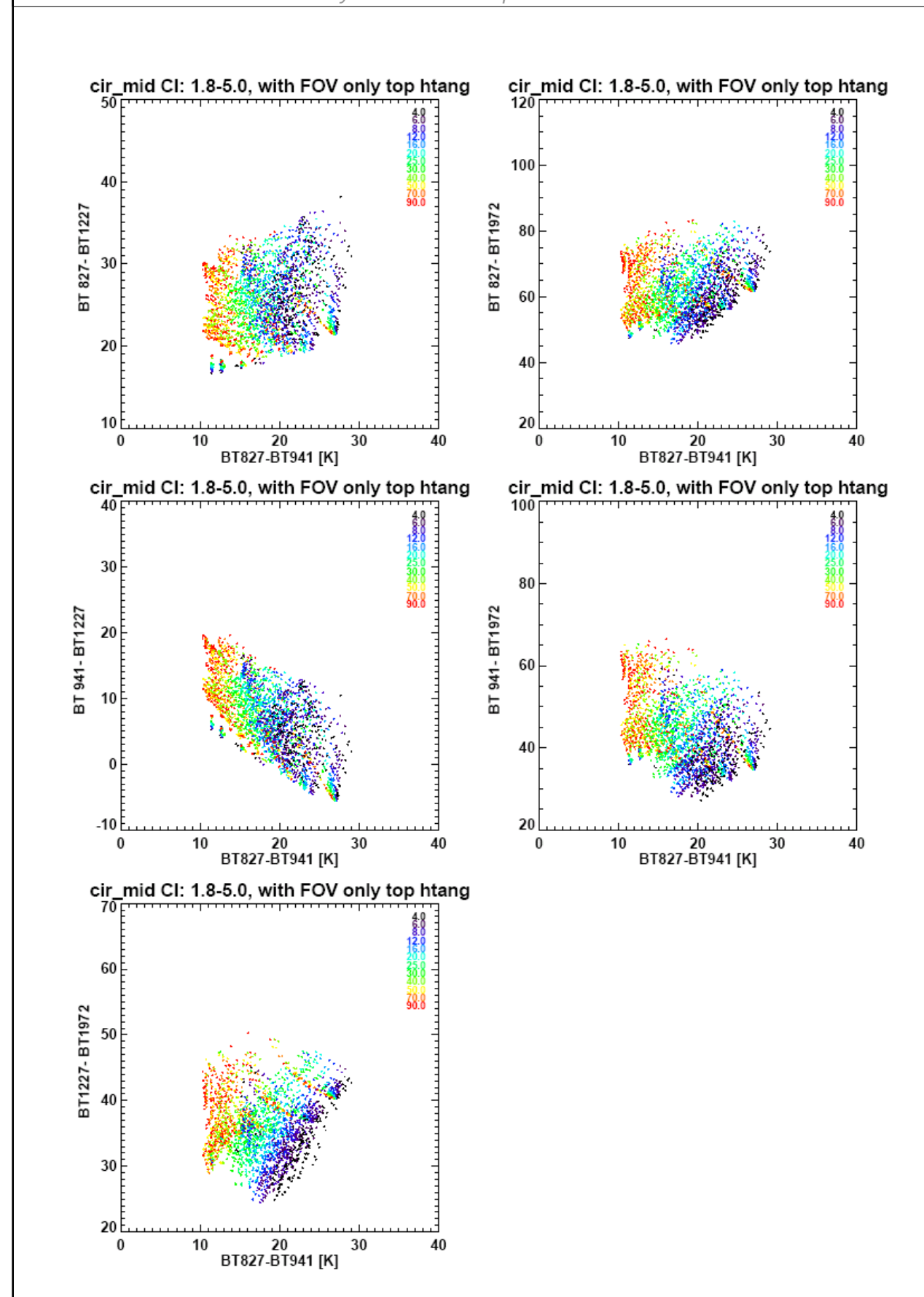


Figure 89: Like Fig. 87 but for mid-latitude cirrus (Mid-latitude cirrus: correlation of brightness temperature differences between different spectral windows. Selection: CI-range: 1.8-5.0, with FOV convolution, only highest-two cloud-affected tangent altitudes.)

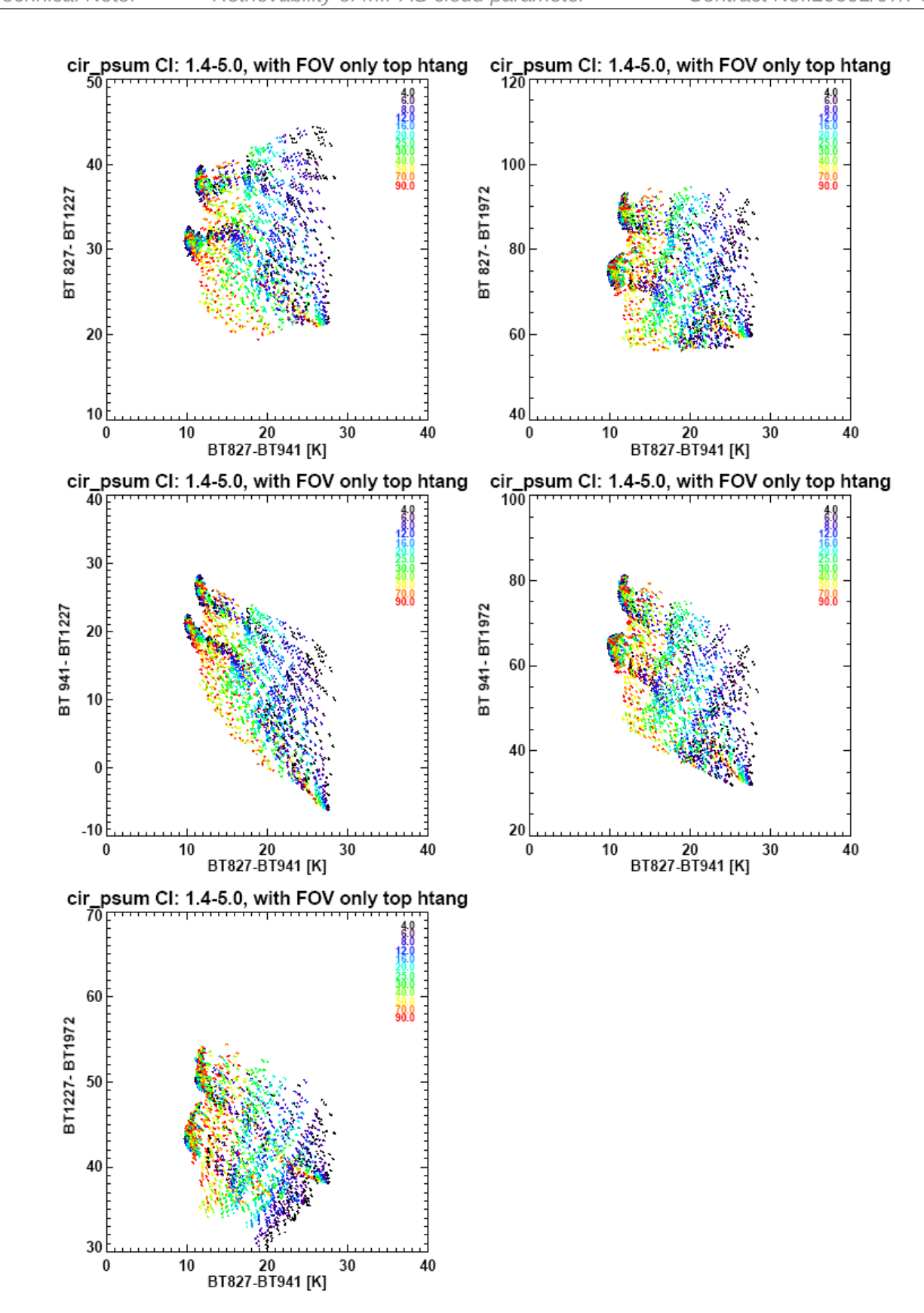


Figure 90: Like Fig. 85 but for polar-summer cirrus (Polar-summer cirrus: correlation of brightness temperature differences between different spectral windows. Selection: CI-range: 1.4-5.0, with FOV convolution, only highest-two cloud-affected tangent altitudes.)

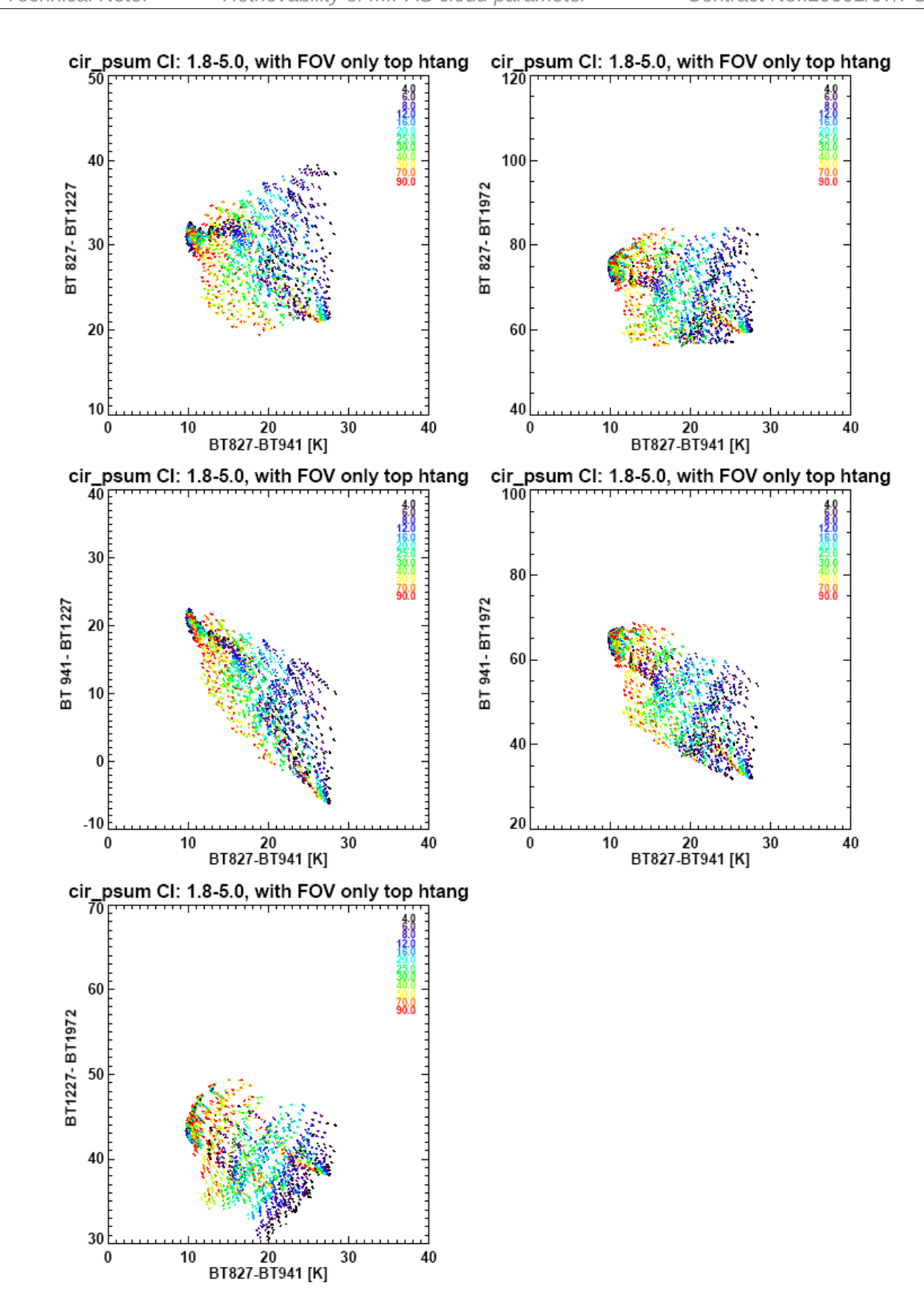


Figure 91: Like Fig. 87 but for polar-summer cirrus (Polar-summer cirrus: correlation of brightness temperature differences between different spectral windows. Selection: CI-range: 1.8-5.0, with FOV convolution, only highest-two cloud-affected tangent altitudes.)

6. Co-located Validation data

6.1 Introduction

The validation of the retrievable products is a prime task for a successful study. Various spaceborne, airborne and ground based have been investigated with respect to potential coincides with the MIPAS instrument for the time period September 2002 to March 2004. This will be a baseline for the more detailed Product Validation Procedure. In the validation process of the study it might be necessary to homogenise/optimise the coincidence criteria.

6.2 In situ and ground based instruments

FISH/FLASH on Geophysica

Ice water content from FISH measurements can be retrieved for various campaign datasets, including Envisat validation campaigns. Coincidence criteria already used for the water vapour validation of ESA operational products have been applied to the flight track. Optically thin cloudiness and cloud free condition are included in the FISH coincidences, but cloud-flagged ESA L1-profiles are so far not accounted for in the analysis of coincidences. This will extended in the near future. Around 35 coincidences with miss-distance 3 hours and 300 km where found in the altitude range 9 to 21 km.

FSSP on Geophysica

Similar analysis has been performed for the flight where the FSSP particle counter operated on the Geophysica. FSSP can deliver particle size distribution information. The minimum information is particle density in certain size bins. For coincidence calculations no restriction on MIPAS data have been applied (cloudy and non-cloudy). A total amount of 140 coincidences were found between 9 and 19 km for a rough 6h/600 km criterion. A restriction to 3h/300km end up with less than 20 coincidence points.

CloudNet Data

Ground-based radar and lidar data from three stations has been analysed at the University of Reading through the EU project CloudNet (www.met.rdg.ac.uk/radar/cloudnet/index.htm). CloudNet provides cloud properties from routine zenith-pointing, multi-wavelength radar and lidar measurements at 5 European stations. 3 of these stations (Cabauw, Chilbolton, Palaiseau) are analysed comprehensively thougout the period in which MIPAS operated in full resolution mode. Products include cloud ice and liquid water content profiles. The radar retrievals are provided together with co-located model cloud (and other meteorological variables) from a number of sources (Met. Office, ECMWF, Meteo France, KNMI). Data is generally provided with a 30s time-step throughout the day, continuously throughout the day for several years, depending on the station. Example CloudNet products are shown in .

Since these 3 stations operate continuously (with some but not many gaps due to operational problems), the maximum number of matches with MIPAS observations can be estimated by determining the number of MIPAS L2 retrievals within a given distance of each group station location (assuming that a CloudNet retrieval will always exist). Figure 93 shows the number of reprocessed MIPAS L2 observations from July 2002 to March 2004, as a function of a given maximum distance from each radar station (taking the latitude/longitude of lowest tangent view from each scan).

Note that the statistics vary from station to station primarily because MIPAS tends to sample similar longitudes along each orbit (the sampled lines of longitude being separated by \sim 500km).

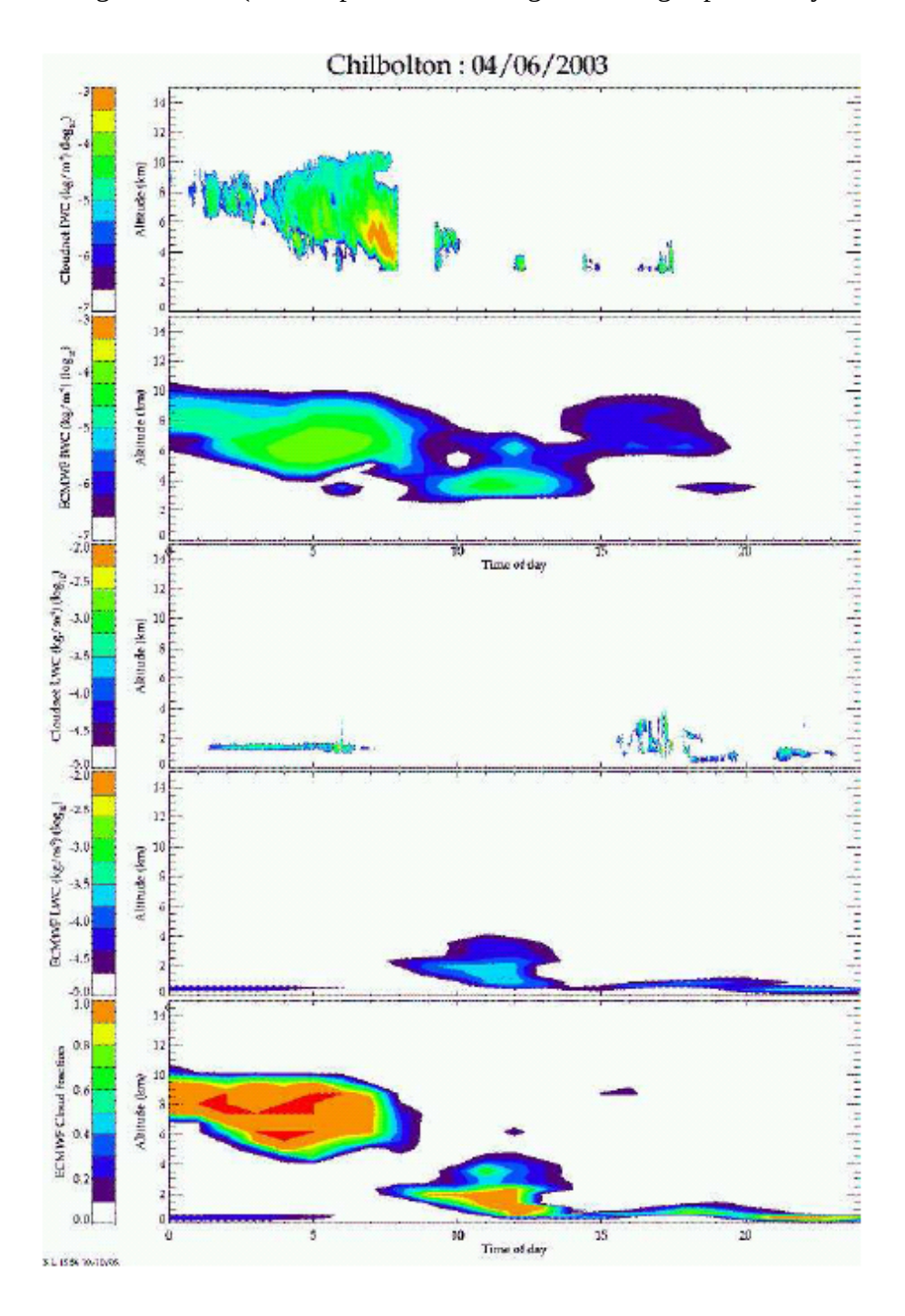


Figure 92: Example IWC and LWC from cloudnet compared to coincident ECMWF model profiles.

It should be noted that all the data processed by cloud-net is from vertically pointing radar/lidar data and so is representative of a much smaller horizontal extent than a MIPAS observation. Even where the co-location between MIPAS and the station is closer the line-of-sight distance in the 3km tangent layer (~400km), the variation of cloud within this distance will almost certainly make the direct comparison of CloudNet data with MIPAS meaningless. It is considered that CloudNet data can only be reliably used to perform statistical comparisons with MIPAS cloud retrievals. I.e. comparisons of monthly or seasonal averages and standard deviations derived from both CloudNet and MIPAS independently (without requiring individual observations to be precisely co-located). *McMurdo*, *NyAlesund and ALOMAR Lidars*

The lidars have been so far investigated for the winter NH 2002/3 (NyAlesund, Alomar) and SH 2003 (McMurdo). They deliver very sensitive CTH information and particle type for PSCs. For the NH lidars 40 respectively 25 coincidences where found for a 4h/400km criterion. For 122 McMurdo lidar profiles we found 1452 MIPAS coincident profiles with a rough criterion for the miss-time of 0.8 days.

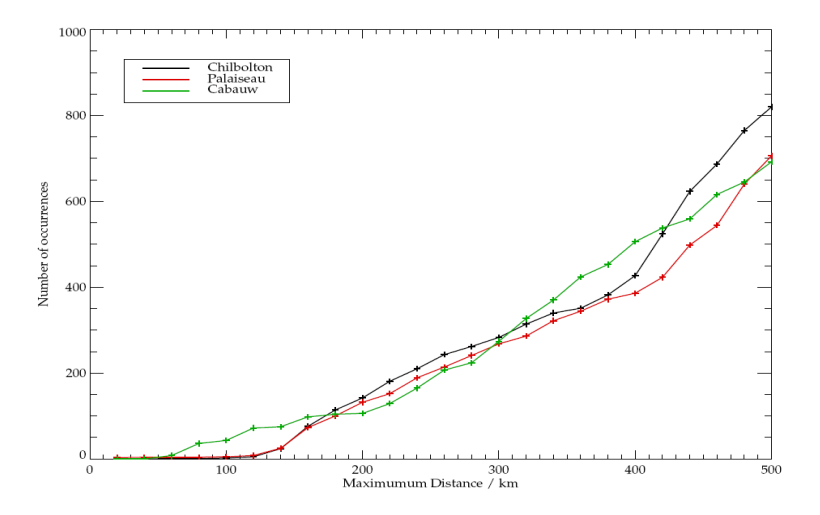


Figure 93: Number of MIPAS reprocessed L2 profiles within a given distance from each CloudNet radar station.

6.3 Satellite Instruments

SEVIRI and AATSR

Retrieval of MSG_1 SEVIRI data and AATSR-Envisat will be an additional very extensive dataset for validation. The overlap between SEVIRI and MIPAS is only for two month February/March 2004 but this is sufficient to find selected cloudy scenes in the geographically restricted area of observations by SEVIRI. MIAPS and AATSR should be co-located with little miss-time, but due to the MIPAS azimuth scanning, AATSR turns out not to be so well co-located with MIPAS, except near the equator. Oxford-RAL ORAC retrieval can be applied to correlative images from MSG-SEVIRI and AATSR to produce the following parameters (along with error estimates for each value: Cloud fraction, Cloud phase (water or ice), Cloud top temperature, Cloud top pressure, Cloud top height, Cloud optical depth (at 0.55 um), Cloud effective radius, Cloud liquid water path.

Occultation Instruments (SAGE/HALOE/POAM III)

All instruments deliver information for PSCs (CTH and potentially PSC type) but also cirrus cloud top heights can be retrieved from the data. For example SAGE and HALOE allow a quasi global statistic. The number of coincidences is quite high 1450 and 950 respectively, whereby HALOE measurements can covers only October 2002 to October 2003. Figure 63 shows the latitude dependence of the coincidences (4h/400km criterion), where for both instruments show in the tropics a significant minimum. For POAM III only NH winter 2002/3 have been investigate. The total number of coincidences with MIPAS were 73 from Dec 2002 to Jan 2003 using a coincidence criteria of 400 km and 4 hours.

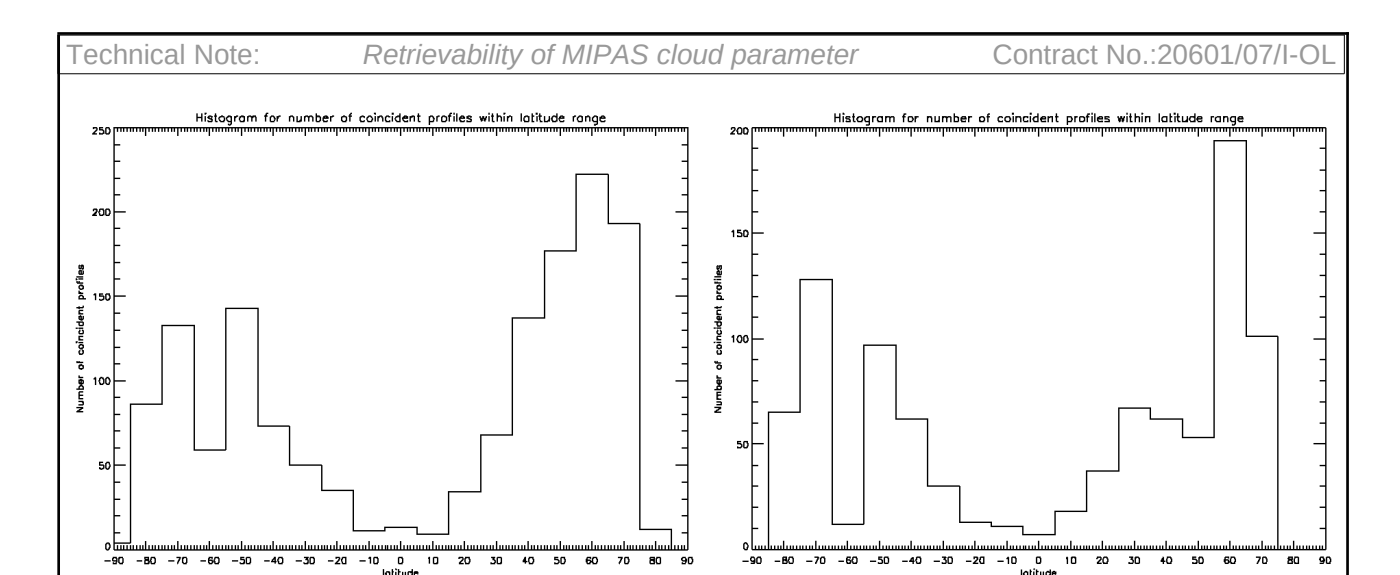


Figure 94: Number of MIPAS-SAGEII (left) and MIPAS-HALOE (right) coincidences for 4h/400km criterion.

GLAS - space borne Lidar

The only technique to obtain a continuous daily global coverage of subvisual/ultra-thin cirrus clouds and PSCs are space-borne lidars. During the first phase of MIPAS observations (June 2002 until March 2004) the Geoscience Laser Altimeter System (GLAS) instrument on ICESat recorded continuous data between 25 September and 18 November 2003. Figure 66 shows an example for closest matches between the two instruments within a time interval of 3h. For a 3h/500km we found around 40000 Lidar profiles coincident with 10700 MIPAS profiles. The large difference in the number is caused by high long-track resolution of the GLAS instrument, whereby frequently a number of GLAS profiles fulfill the coincidence criterion for one MIPAS profile. Reducing the criterion to 1h/100km results in still a large statistic of 3230 GLAS and 553 MIPAS profiles.

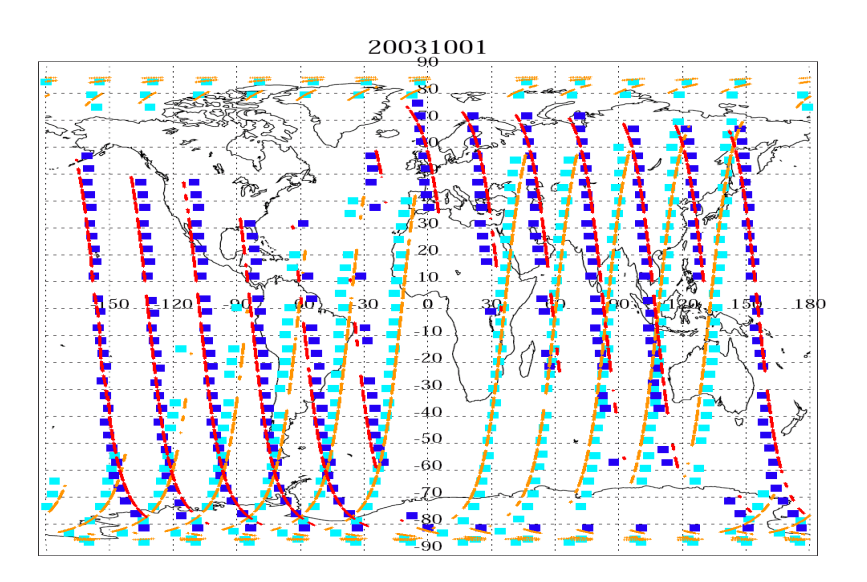


Figure 95: Coincidences between MIPAS limb scans (large squares, dark blue: night, light blue: day) and GLAS-Lidar observations (red: night, orange: day) on 1 Oct 2003.

The validation of the retrievable products is a prime task for a successful study. Various spaceborne, airborne and ground based have been investigated with respect to potential coincides with the MIPAS instrument for the time period September 2002 to March 2004. A summary table (Table 16) is compiled to give an overview of potential cloud parameter and number of coincidences related to miss-time/miss-distance. This will a baseline for the more detailed Product Validation Procedure.

Instrument	Miss-time/distance	Number of Coincidenes	Parameters
FISH	3h/300km	(35) _{hb}	IWC
FSSP	6h/600km	140	volume/radius
CloudNet (3 sites)	minuntes/400km	~ 1200	IWC, CTH, LWC
NH Lidar (PSC)	4h/400km	65	CTH, PSC type
SH Lidar (PSC)	0.8 days	122	
SAGE II (III)	4h/400km	1450	CTH, vol, SVC,
HALOE	4h/400km	950	EXT, PSC-type
POAM	4h/400km	73 _{PW2002/3}	
GLAS	3h/300km	40000L/10700M	СТН
	1h/100km	3237L/543M	
SEVIRI (nadir)	0/0	Feb/Mar 2003	СТН, СТР,СТТ,
AATSR (nadir)	0/0 (tropics)	Equ Region	LWP

Table 16: Summary of potential vallidation datasets for MIPAS cloud products.

6.4 Intercomparison with Aura Instruments

6.4.1 Introduction

The NASA Aura satellite was launched on July 15 2004 and therefore overlapped only with the MIPAS RR measurements. AURA is in a near polar, sun-synchronous orbit at 705 km (cf 800 for Envisat) approximately 100 minutes and crosses the equator at 13:45 local solar time for the ascending node (cf 10.00 descending node for Envisat). It has a ground track repeat-time of 16 days (cf 3 days for Envisat). Some preliminary work has been performed on comparisons of cloud macroscopic parameters with the two infrared instruments on Aura: HIRDLS and TES.

6.4.2 HIRDLS

The High Resolution Dynamics Limb Sounder (HIRDLS) HIRDLS is a 21-channel limb-scanning infrared radiometer, which includes window channels for aerosol/cloud detection, and Cloud Top Height is an operational product. However, due to pointing error, operational HIRDLS altitudes are accepted to be higher by 1.7 km than intended, so effectively a first order correction can be applied to the CTHs by simply subtracting off 1.7 km from the reported values. The HIRDLS science team is currently working on retrieving extinction information from cloudy spectra, however this algorithm has yet to be fully developed and HIRDLS extinction values are not yet available.

6.4.3 TES

The Tropospheric Emission Sounder (TES) is an infrared-imaging, limb and nadir sounding Fourier Transform Spectrometer which measures spectra between $650 - 3050 \text{ cm}^{-1}$ at a resolution of 0.02 cm^{-1} for altitudes between 0 - 33 km. However, TES is currently operated almost exclusively in nadir-viewing mode. The TES team models the radiance contributions of clouds using a frequency dependent set of cloud optical depth and cloud top height, which are retrieved

simultaneously with the regular products of temperature, emissivity and trace gases. TES operationally reports cloud top heights and average effective cloud optical thickness as determined from its nadir measurements.

6.4.4 Comparison with MIPAS

A comparison has been carried out of cloud properties retrieved from MIPAS spectra against HIRDLS and TES operational cloud products. The month of May 2006 has been (arbitrarily) chosen as the study timeframe as all instruments have a high degree of coverage and of processed data during that period. Although spatially, the orbits of the two spacecraft enable many overlapping measurements, temporally the orbits are far enough apart that there are few measurements which overlap in both time and space - it is thus not plausible to compare the cloud products on a case-by-case level, but rather on a statistical basis only. In this comparison, the retrieved MIPAS CTH is compared with both the HIRDLS and TES CTHs and the retrieved MIPAS K_{ext} is compared with the TES optical depth. As well, comparisons about how often each of the instruments detect cloud (ie. cloud frequency) are carried out to get a feel for each instrument's inherent sensitivity to certain types of cloud.

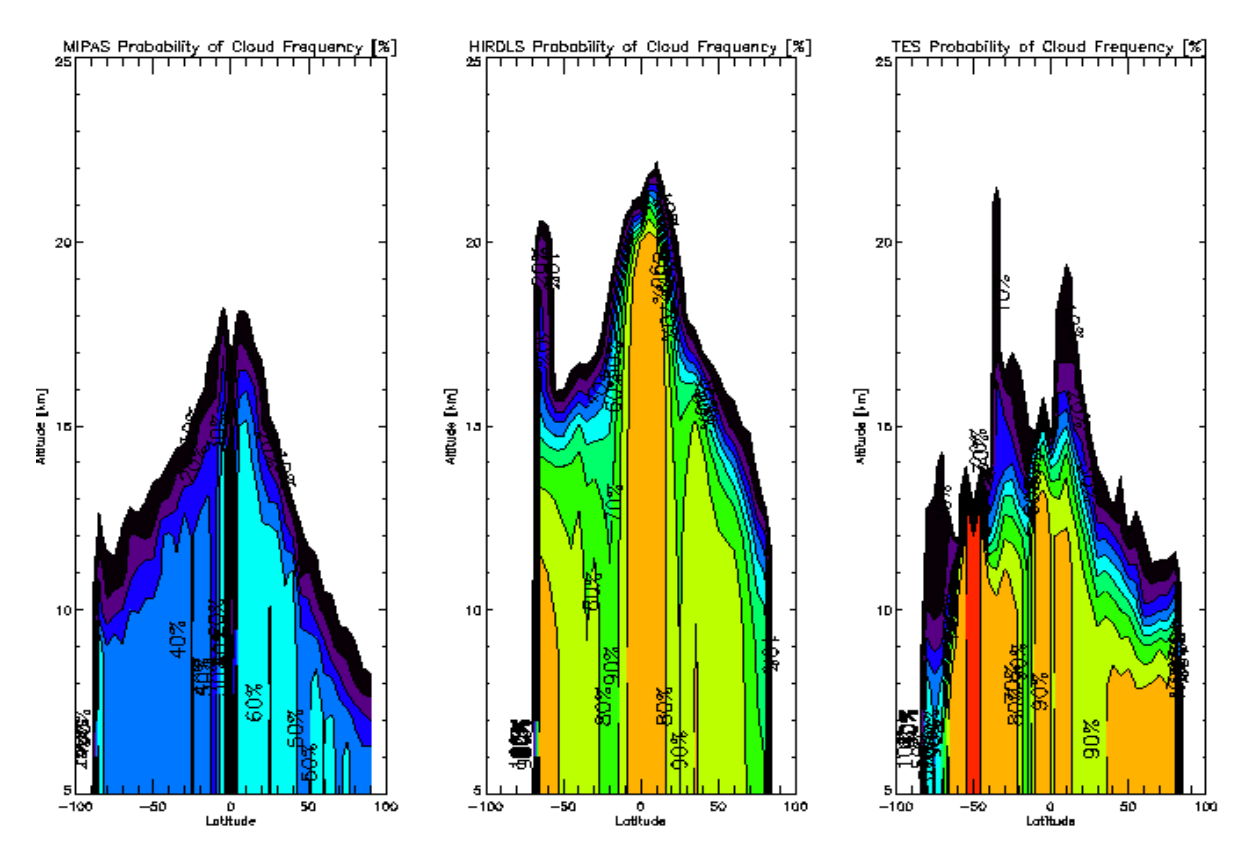


Figure 96: Probability that there exists cloud cloud at a given latitude and at or below a given altitude for MIPAS (left), HIRDLS (middle) and TES (right).

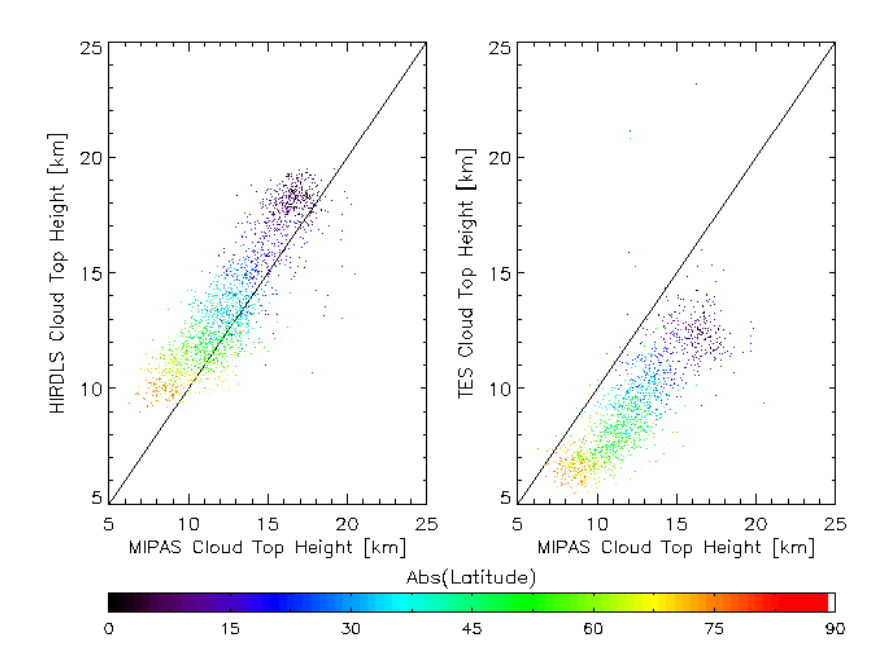


Figure 97: Scatter plots showing the mean cloud top height [km] in each 5° latitude/longitude grid for MIPAS and HIRDLS (left), and MIPAS and TES (right). The CTHs are colour-coded by latitude, whereby red points are polar points and black correspond to equatorial points, as described by the colourbar. Black line is the one-to-one line.

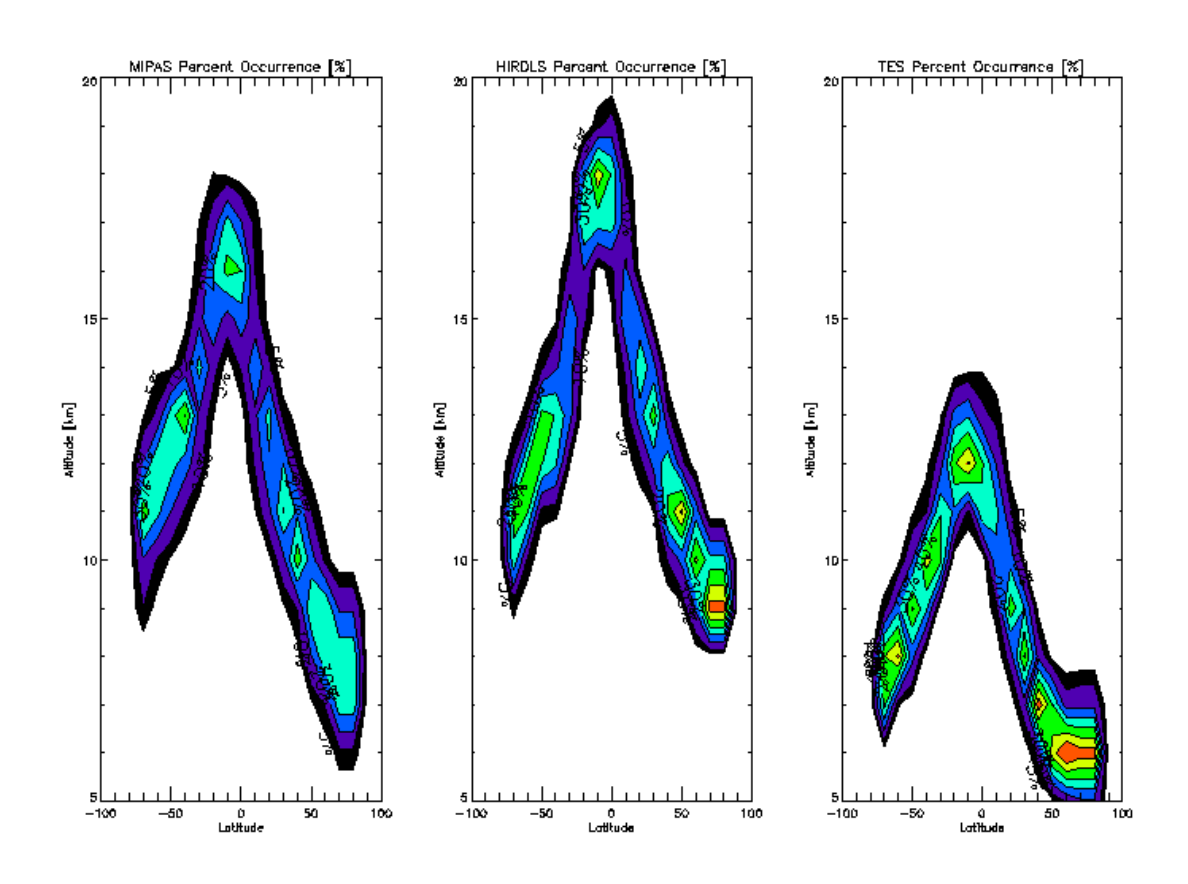


Figure 98: Probability distribution function of CTH from MIPAS (left), HIRDLS (centre) and TES (right).

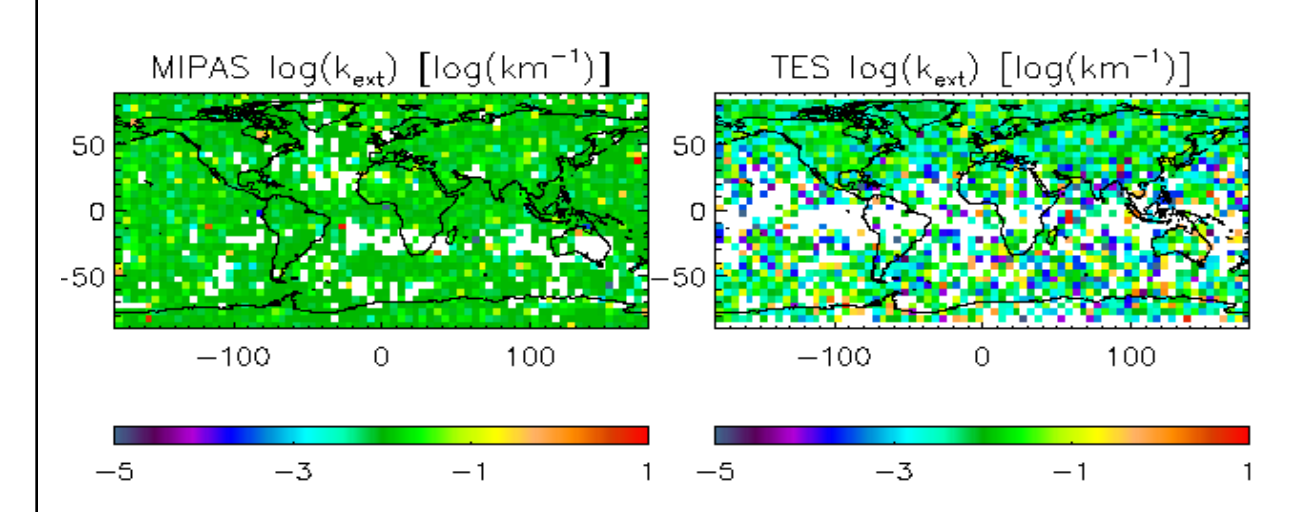


Figure 99: Mean of logarithm of extinction coefficient in 5° latitude/longitude grid from MIPAS (left) and TES (right).

6.4.5 Conclusions

Overall, from a qualitative perspective, the MIPAS retrieved cloud products of cloud top height and cloud extinction coefficient compare well with HIRDLS cloud top height and TES cloud top height and cloud optical depth.

In terms of cloud detection, all instruments show the same global distribution, with increased probability of finding cloud in the tropics and less at the poles. However, MIPAS notes far less cloud detected than do the other two instruments, which is undoubtedly due to a too strict threshold being used in the detection method.

All cloud top heights exhibit the same global patterns --- for instance, in terms of increasing height with increased proximity to the equator and heightened cloud over regions of known convection. HIRDLS shows the highest cloud tops and TES the lowest, but taking into account the known 1.7 km pointing error associated with HIRDLS and the fact that TES cloud products are from it's nadirviewing measurements, the cloud top heights reported by all three instruments agree quite well.

Both MIPAS and TES report a near-global coverage of extinction coefficient of 10⁻² km⁻¹, however TES exhibits more structure globally than does MIPAS, however this may just be a result of different cloud layers being detected.

7. Summary and Conclusions for Processor Realisation

This section summarizes the outcome of the feasibility study of the current knowledge in retrieving cloud parameter from MIPAS spectra in order to give recommendations what kind of products a potential cloud processor is able to provide under the restriction of a near real time processing (NRT).

(a) Cloud Scenario Database

A major part of this study was the compilation of a unique database of modeled cloud spectra under various atmospheric condition, geometries, with the derivatives of the spectra (Jacobians) of the most prominent parameters, and all of this for a number of cloud and aerosol types. This dataset facilitate various applications:

- to quantify the retrievability of various cloud parameter
- to quantify the errors of retrieval parameters
- to specify classification schemes for a number of cloud types
- to test various retrieval algorithms with blind data sets

In addition, the dataset is an extremely valuable tool for studies on the retrievability of cloud parameters for instruments planed for the future and the definition of corresponding instrument specifications.

(b) Cloud Detection

Various methods for cloud detection have been investigated in this study. Each of theses methods has advantages and disadvantages depending on the intention of the follow-on analyses. For example extremely sensitive methods in the UTLS might fail in the free troposphere. Very robust techniques are necessary for trace gas retrieval, where slightly contaminated spectra by clouds are not that problematic, but the underestimation of the real cloud occurrence in a specific altitude level by a cloud index threshold not stringent enough to detect all potential cloud events, would result in a bad validation result. In consequence we like to suggest, that for a cloud processor a number of cloud detection methods should be implemented in parallel. All detection methods can detect clouds quite effectively but with restrictions under certain conditions. At a later stage of the project (processor product validation) a combination of the various techniques will achieve the best possible compromise in respect to sensitivity and robustness.

In addition it is desirable, that a user of the processor has the possibility to decide which algorithm gives the most valuable results for his application and a certain flexibility of the scheme will also help to adopt the processor under changing atmospheric and instrumental background conditions, like for example the reduced resolution data or enhanced aerosol load due to a volcanic eruption.

(c) Cloud Classification

The differentiation of cloud types turn out to be a very difficult task. Simple two colour ratio or brightness temperature difference scatter plots are not sufficient for some of the required classification and improvements are still necessary. However, the differentiation of most PSC types in the CSDB works excellent, which is a kind of proof of concept for a number of recent publications on MIPAS PSC data. The most difficult task here is the differentiation between NAT and STS. But a combination of two different multi-spectral analyses will allow a reliable differentiation in certain areas of the correlation diagram.

Liquid and ice water clouds are not distinguishable with the well established MWs and multi BTD methods used for nadir measurement in the IR. The different observation geometry results in a much larger variability of the parameter and the loss of a significant separation in the correlation diagrams. Various attempts have been tested with only limited success, like a clustering for optical thick conditions and areas in the correlation diagram restricted only to liquid clouds, but merging with cirrus in other areas. Further analyses are planned by applying a naive Bayes classifier to the database. These method optimises the selection of a number of CR or BTD to a maximum in the probability density. In addition, temperature criteria can help to constrain the plausibility for liquid (T>-40°C) and cirrus clouds.

Finally, aerosols have not been taken into account so far in the analyses, due to the fact that (1) the compilation of aerosol database was delayed, (2) under the atmospheric conditions in 2002-2004 the aerosol load was extremely low in the stratosphere and in consequence the continuum contributions very low, and (3) enhanced tropospheric aerosol comes only into focus, when concentrating on the lowest altitude level of MIPAS (4-6 km), where the large amount of water vapour continuum causes a lot of difficulties to define a reliable classification scheme. This is even the case for liquid and cirrus clouds at these levels.

(d) Macrophysical Cloud Parameter

The macrophysical retrieval of parameters like cloud fraction, cloud top height/pressure/temperature and extinction with a very simple cloud forward model shows quite consolidated results on the test datasets for 2003, for the reduced resolution mode and in comparison to cloud parameter of the EOS Aura instruments. A more recent analysis with the CSDB spectra (not part of section 5.1) show that the retrieval does a fairly consistent job even in the case of optically very thin and for non-cloudy spectra.

(e) Microphysical Cloud Parameter

The linear error analysis show that the MIPAS IR spectra should include enough information content to retrieve microphysical cloud parameter (like volume densities, respectively IWC and size information). However, this appears only possible with a cpu-expensive and detailed forward model and/or under the assumption of horizontal inhomogeneity.

The area density integrated along the limb path (area density path, APD) shows a robust correlation with the standard CI-CR, which gives confidence that the retrieval of an upper threshold for ADP under optical thick conditions and moderate error bars for optically thin conditions is realistic. In addition, ADP looks like a valuable quantity for comparisons with other limb sounding instruments and includes itself microphysical information. With the assumption that the cloud is homogeneous along the limb path the particle surface area density (AD) can be estimated. Together with an external or internal information on a realistic effective radius (e.g. parameterisations for $R_{\rm eff}$ as function of T or from the particle size retrieval of the same spectrum, see below) it is possible to estimate the IWC. Despite these quantity would be only an estimate, it is a quite valuable product for scientific applications (e.g. comparisons with global models).

The uncertainties of the quantities ADP, AD, IWP and IWC are difficult to quantify, but this should be possible when applying modeled spectra for realistic clouds geometries (with FM2D) in a kind of blind test to the processor prototype. This is a planned activity in the ongoing study. Further investigations are to consolidate the very promising possibility to determine size bins for the effective radius based on the IR spectra without any time expensive forward model.

(f) Validation and error assessment

Various satellite, airborne and ground based instrument data have been collected for validation

purposes of this studies. However, comparison with most instruments suffers under the problem, that viewing geometries or the sensitivity for cloud detection are very different to the MIPAS limb sounding instrument. In consequence comparisons on a well-founded statistical basis (like large number of coincidences, zonal means, monthly means, etc.) are the preferable way of validation. This is necessary, because each instrument observes the potentially very heterogeneous cloud field from a different position and therefore with a different LOS. This makes the interpretation of comparisons of single events quite unspecific and problematic.

Best suited datasets for the 7/2002 to 3/2004 period are for example the GLAS lidar, the HALOE and SAGE occultation instruments or the well established international satellite cloud climatology project dataset (ISCCP, so far not investigated in detail). The latter is exclusively based on nadir looking instruments and might have a lack of sensitivity for very thin cirrus clouds, where MIPAS is especially well suited for detection.

An alternative way of validation of the planned cloud processor is a blind test of the processor with modeled clouds spectra and profiles compiled of cloud-free and cloud spectra. This can include spectra of the CSDB (KOPRA and especially FM2D spectra on broken cloud fields) or already well characterised single events of the MIPAS dataset. An appropriate validation procedure should be implemented for better characterisation of the processor and the quantification of the processor product errors.

8. References

Ackerman, S., Smith, W.L., Spinhire, J.D., and Revercomb , H.E, 1990, "The 27-28 October 1986 FIRE IFO Cirrus case study: Spectral properties of cirrus clouds in the 8-12 micron window", Monthly Weather Review, 118, 2377 - 2388 .

Baran, A. J., P. N. Francis, L.-C. Labonnote, and M. Doutriaux-Boucher, A scattering phase function for ice cloud: Tests of applicability using aircraft and satellite multi-angle multi-wavelength radiance measurements of cirrus. Q. J. R. Meteorol. Soc., 127, 2395-2416, 2001

Desmond, H., Optimisation of Microwindow Positioning for the Detection of Cloud in MIPAS Spectra, http://www.atm.ox.ac.uk/group/mipas/reports/Desmond Cloptimisation.pdf, 2007.

Donovan, D. P., Ice-cloud effective particle size parameterization based on combined lidar, radar reflectivity, and mean Doppler velocity measurements, J. Geophys. Res., 108(D18), 4573, doi:10.1029/2003JD003469, 2003.

Evans, K.F., The spherical harmonics discrete ordinate method for three-dimensional atmospheric radiative transfer, American Met. Soc., 55:429–446, 1998.

Ewen, G.B.L., R.G. Grainger, A. Lambert and A.J. Baran, Infrared radiative transfer modelling in a 3D scattering cloudy atmosphere: Application to limb sounding measurements of cirrus, Journal of Quantitative Spectroscopy and Radiative Transfer, Vol. 96, 45-74, 2005.

Greenhough, J., J. J. Remedios, H. Sembhi, and L. J. Kramer, Towards cloud detection and cloud frequency distributions from MIPAS infra-red observations, Advances in Space Research, 36, 800-806, 2005.

Höpfner, M., N. Larsen, R. Spang, B. P. Luo, J. Ma, S. H. Svendsen, S. D. Eckermann, B. Knudsen, P. Massoli, F. Cairo, G. Stiller, T. v. Clarmann, and H. Fischer, MIPAS detects Antarctic stratospheric belt of NAT PSCs caused by mountain waves, Atmos. Chem. Phys., 6, 1221-1230, 2006a.

Höpfner, M., B. P. Luo, P. Massoli, F. Cairo, R. Spang, M. Snels, G. Di Donfrancesco, G. Stiller, T. von Clarmann, H. Fischer, and U. Biermann, Spectroscopic evidence for NAT, STS, and ice in MIPAS infrared limb emission measurements of polar stratospheric clouds, Atmos. Chem. Phys., 6, 1201-1219, 2006b.

Höpfner, M. and C. Emde, Comparison of single and multiple scattering approaches for the simulation of limb-emission observations in the mid-IR, J. Quant. Spectrosc. Radiat. Transfer, 91, 3, 275-285, 2004.

Höpfner, M., Study on the impact of polar stratospheric clouds on high resolution mid-IR limb emission spectra, J. Ouant. Spectrosc. Radiat. Transfer. 83, 1, 93-107, 2004.

Höpfner, M., H. Oelhaf, G. Wetzel, F. Friedl-Vallon, A. Kleinert, A. Lengel, G. Maucher, H. Nordmeyer, N. Glatthor, G. Stiller, T. von Clarmann, H. Fischer, C. Kröger, and T. Deshler, Evidence of scattering of tropospheric radiation by PSCs in mid-IR limb emission spectra: MIPAS-B observations and KOPRA simulations, Geophys. Res. Lett., 29(8), 1278, doi:10.1029/2001GL014443, 2002.

Höpfner, M., T. Blumenstock, F. Hase, A. Zimmermann, H. Flentje, and S. Fueglistaler, 'Mountain polar stratospheric cloud measurements by ground based FTIR solar absorption spectroscopy', Geophys. Res. Lett. 28, 11, 2189-2192, 2001.

Höpfner, M., C.E. Blom, H. Fischer, N. Glatthor, T. Gulde, C. Piesch, 'HNO3 and PSC measurements from the TRANSALL: sequestering of HNO3 in the winter of 1994/95', J. Atmos. Chem., 30, 61-79, 1998.

B. Kerridge, et al., Consideration of mission studying chemistry of the utls. Final Report ESA Contract No 15457/01/NL/MM, 2004

Kahn, B. H., and Eldering, A., Irion, F. W., Mills, F. P., Sen, B., and Gunson, M. R., 2003, "Cloud identification in Atmospheric Trace Molecule Spectroscopy infrared occultation measurements", Applied Optics, 41, 15, 2768 - 2780

Kramer, L.J., Sensitivity of the MIPAS instrument on ENVISAT to the detection of Polar Stratospheric Clouds, M. Phil. thesis, *University of Leicester*, 2004.

Remedios, J. J., Profiles for MIPAS EOS, Space Research Centre, Leicester, UK, January 2001.

Remedios J.J., Spang, R. Detection of cloud effects in MIPAS spectral data and implications for the MIPAS operational processor, Proceedings of the ENVISAT Calibration Review, 9-13 September 2002, ESA-ESTEC, Noordwijk, The Netherlands, 2002.

Remedios, J. J., R. J. Leigh, A. M. Waterfall, D. P. Moore, H. Sembhi, I. Parkes, J. Greenhough, M.P. Chipperfield, and D. Hauglustaine, MIPAS reference atmospheres and comparisons to V4.61/V4.62 MIPAS level 2 geophysical data sets, Atmos. Chem. Phys. Discuss., 7, 9973-10017, 2007

Raspollini P. et al., Spie Proceedings, Level 2 near-real-time analysis of MIPAS measurements on ENVISAT, Remot Sensing of Clouds and the Atmosphere VII, Volume 4882, Agia Pelagia, Crete, Greece, 2002.

Shettle, E. P., Fenn, R. W.: Models for the aerosols of the lower atmosphere and effects of humidity variations on their optical properties. AFGL-TR-79-0214, 20 September 1979.

Spang, R., M. Riese, G. Eidmann, D. Offermann, and P.H. Wang, A detection method for cirrus clouds using CRISTA 1 and 2 measurements, Adv. Space Res., 27/10, 1629- 1634, 2001.

Spang, R., Remedios, J. J. Observations of a distinctive infra-red spectral feature in the atmospheric spectra of polar stratospheric clouds measured by the CRISTA instrument, Geophys. Res. Lett., 30(16), 1875, doi:10.1029/2003GL017231, 2003.

Spang R., J.J. Remedios, and M.P. Barkley, Colour indices for the detection and differentiation of cloud types in infrared limb emission spectra, Adv. Space Res., 33 1041-1047, 2004.

Spang R., J. J. Remedios, L. J. Kramer, L. R. Poole, M. D. Fromm, M. Müller, G. Baumgarten, P. Konopka, Polar stratospheric cloud observations by MIPAS on ENVISAT: detection method, validation and analysis of the northern hemisphere winter 2002/2003, Atmos. Chem. Phys. 5, 679-692, 2005a.

Spang, R., J. J. Remedios, S. Tilmes, and M. Riesef, MIPAS observations of Polar Stratospheric Clouds in the Arctic 2002/3 and Antarctic 2003 winters, Advances in Space Research, 36, 868-878, 2005b

Spang, R. et al., High resolution limb observations of clouds by the CRISTA-NF instrument during the SCOUT-O3 tropical aircraft campaign, J. Adv. Space Res. (2007), doi:10.1016/j.asr.2007.09.03

Tisdale, R. T., D. L. Glandorf, M. A. Tolbert, und O. B. Toon. Infrared optical constants of low–temperature H2SO4 solutions representative of stratospheric sulfate aerosols. J. Geophys. Res., 103(D19):25,353–25,370, 1998.

Voigt C., H. Schlager, H. Ziereis, B. Kärcher, B. P. Luo, C. Schiller, M. Krämer, P. J. Popp, H. Irie, Y. Kondo, Nitric acid in cirrus clouds, *Geophys. Res. Lett.*, 33, L05803, doi:10.1029/2005GL025159, 2006.

Yang, P., Wei, H-L., Baum, B.A., Huang, H-L., Heymsfield, A.J., Hu, Y.X., Gao, B-C., and Turner, D.D., 2003, "Spectral signature of mixed phase clouds composed of non-spherical ice crystals and spherical liquid droplets in the terrestrial window region", Journal of Quantitative Spectroscopy and Radiative Transfer, 79-80, 1171-1188.

Yang, P., Liou, K.N., and Arnott, W.P., 1997, "Extinction efficiency and single-scattering albedo for laboratory and natural cirrus clouds", Journal of Geophysical Research, 102.D18. 21,825-21,835

Zasetsky, A. Y., A. F. Khalizov, M. E. Earle, and J. J. Sloan: Frequency Dependent Complex Refractive Indices of Supercooled Liquid Water and Ice Determined from Aerosol Extinction Spectra, J. Phys. Chem. A, 109, 2760-2764, 2005.